Hydrogel Nanostructures for Plasmonic and Biosensor Applications

Dissertation for obtaining a doctoral degree at the
University of Natural Resources and Life Sciences, Vienna

Submitted by

Nityanand Sharma

Supervisor : Prof. Dr. Wolfgang Knoll

University of Natural Resources and Life Sciences, Vienna

Department of NanoBioTechnology

University of Natural Resources and Life Sciences

Vienna, November 2015

तमसो मा ज्योतिर्गमय..

Lead us from darkness (ignorance) to brightness (knowledge)..

— Brhadaranyaka Upanishad

To my parents...

Acknowledgements

Experimental research is often a collaborative endeavor, and the work presented in this thesis is certainly no exception. During the last three years, I have had the pleasure of working with a number of bright and enthusiastic people. I take this opportunity to earnestly thank everyone who has helped me directly or indirectly to complete this project.
I would, first, like to thank Prof. Dr. Wolfgang Knoll for giving me the opportunity to do PhD at BOKU and AIT. I also thank Prof. Dr. Bo Liedberg for his support during our stay at NTU, Singapore. I would like to express my gratitude to Prof. Dietmar Pum, Prof. Erik Reimhult and Prof. Eva Sinner for their support to finish my course work at BOKU.
My deepest appreciation goes to Dr. Jakub Dostalek for his active guidance, fruitful discussions and supports which provided me new ideas in my research. Jakub has always been ready to lend a hand in the lab. His positive attitude and enthusiasm has been inspirational.
Vienna has been a wonderful place to work, and I have been blessed with a large number of friends and coworkers. It has been my good fortune to work with the Matin, Hulan and Imran in the lab. I have truly enjoyed working with them. Discussions with Simone, Stefan and Nestor has always been enjoyable. Many other people outside the group have significantly enriched my life in Vienna, and, their contribution and support can't be overlooked. Support provided by Manuela at various stages are unforgettable. Discussions with Drago over various issues has helped me understand things better. Company of Ciril has always helped me in finding vegetarian food at different places. Presence of Dr. Yi Wang at NTU, Singapore was very helpful.

Words cannot express my gratitude to my parents and relatives. Their love and unconditional support has always been the bedrock upon which every important achievement in my life has been built.
Lastly and most importantly, I would like to thank the *supreme power* for his grace on me without which I could not have achieved anything.

Vienna, 12 November 2015 Nityanand.

Abstract

Plasmonics is recently emerged nanophotonics research area that focuses at sub-wavelength confinement of light energy by its coupling to surface plasmons - collective oscillations in charge density and associated electromagnetic field at surfaces of metals. Hybrid responsive polymer-metallic nanostructures represent an attractive class of materials with actively tunable plasmonic properties. Such characteristics may enable new applications of plasmonics in analytics that utilize direct or optical spectroscopy-based detection of molecular analytes as well as in development of novel miniaturized plasmonic components. This thesis describes novel implementations of thermo-responsive *N*-isopropylacrylamide (pNIPAAm) - based hydrogel to metallic nanostructures that support surface plasmons. It reports means of structuring a photo-crosslinkable pNIPAAm layer with features exhibiting size as small as 100 nm by nano-imprint lithography and laser interference lithography. A new technique for in situ observation of swelling characteristics of such nanoscopic soft matter objects that are arranged in a period array was developed based on optical waveguide mode-enhanced diffraction measurements. pNIPAAm periodic structures highly swell in water (swelling ratio up to 10) and they can be prepared on around 1 cm^2 area on a gold surface. A structure that acts as a tunable plasmonic crystal was prepared and by its reversible swelling and collapsing a plasmonic bandgap can be open and closed. In addition, responsive pNIPAAm material was employed as a "glue" in plasmonic structures. Firstly, it was employed to serve as a responsive cushion that tethers a thin metallic film with arrays of nanoholes to a solid glass surface. The swelling and collapsing of the cushion is demonstrated to mediate the extraordinary transmission and potentially offer a new means of the implementation of nanohole arrays surface plasmon resonance biosensor with flow-through architecture. Lastly, pNIPAAm was used as a glue in order to form a composite film with high density of nanoparticles that were imprinted with a low molecular weight organic molecule. The composite film exhibited highly open architecture through which the target analyte L-Boc-phenylalanine-anilide (L-BFA) can freely diffuse and become affinity capture. Direct detection of affinity binding at concentrations around μM was carried by optical waveguide spectroscopy as the composite film can serve at the same time as large capacity affinity binding matrix and an optical waveguide.

Abbreviations

2D/3D...	Two Dimensional/ Three Dimensional
AFM.....	Atomic Force Microscopy
ATR.....	Attenuated Total Reflection
BP-Thiol.	(3-thiopropyl)oxybenzophenone
BRE.....	Bio-Recognition Element
EBL.....	Electron Beam Lithography
EG.....	Ethylene Glycol
FDTD....	Finite Difference Time Domain
FIB	Focused Ion Beam
FOM.....	Figure of Merit
ITO	Indium Tin Oxide
IUPAC...	International Union of Pure and Applied Chemistry
L-BFA....	L-Boc-phenylalanine-anilide
L-BPA....	L-Boc -phenylalanine
L-BTP ...	L-Boc-Tryptophan
L-BTS....	L-Boc-tyrosine
LCST	Lower Critical Solution Temperature
LIL.....	Laser Interference Lithography
LOD	Limit of Detection
MAA.....	Methacrylic Acid
MIP.....	Molecularly Imprinted Polymer
NHA.....	Nanohole array
NIL.....	Nano-imprint Lithography
NIP.....	Non-Imprinted Polymer
OSTEmer	Off-Stoichiometry Thiol-Enes Polymer
OWS.....	Optical waveguide Spectroscopy
PDMS ...	Polydimethylsiloxane
pNIPAAm	Poly(N-isoproprylacrylamide)
RIfS.....	Reflection Interference Spectroscopy
RIU.....	Refractive Index Unit

SAM	Self-Assembled Monolayer
SEM	Scanning Electron Microscopy
SERS.....	Surface Enhanced Raman Spectroscopy
SPPs	Surface Plasmon Polaritons
SPR	Surface Plasmon Resonance
SPs	Surface Plasmons
SR	Swelling Ratio
TE	Transverse Electric
TIR	Total Internal Reflection
TM	Transverse Magnetic
UV	Ultraviolet

Publications

This thesis is based on the following papers, which are referred to in the text by their numbers (4-7).

4 **N. Sharma**[*], F. Pirani[*], A. M. Cencerrado, S. Fossati1, C. Petri, U. Jonas, E. Descrovi, J. L. Toca-Herrera, J. Dostalek., **Waveguide-Enhanced Diffraction for Observation of Responsive Hydrogel Nanostructures**, (Manuscript in preparation) ([*]First authorship shared)
Author's contribution: NS was responsible for planning, and evaluating the waveguide-enhanced-diffraction measurements. NS wrote the main part of the manuscript. FP obtained the measurement data. CP synthesized the polymers. AMC obtained the *in situ* AFM images.

5 **N. Sharma**, C. Petri, U. Jonas, J. Dostalek., **Reversibly Tunable Plasmonic Bandgap by Responsive Hydrogel Grating**, (Manuscript in preparation)
Author's contribution: NS was responsible for planning, performing and evaluating the width of bandgap calculation in angular-wavelength measurements. NS wrote the main part of the manuscript. CP synthesized the polymers.

6 **N. Sharma**, H.Keshmiri, C. Petri, T. I. Wong, X. Zhou, U. Jonas, J. Dostalek., **Tunable Plasmonic Nanohole Arrays Actuated by a Thermo-responsive Hydrogel Cushion**, (Manuscript submitted) Journal of Physical Chemistry C
Author's contribution: NS was responsible for planning, performing and evaluating the thermo-responsive and refractometric measurements. NS wrote the main part of the manuscript. CP synthesized the polymers, HK did the simulation, TIW prepared the nanohole arrays.

7 **N. Sharma**, C. Petri, U. Jonas, M. Bach, G. Tovar, K. Mrkvova, M. Vala, J. Homola, W. Knoll, J.Dostalek., **Molecularly Imprinted Polymer Waveguides for Direct Optical Detection of Low– Molecular–Weight Analytes**, Macromolecular Chemistry and Physics (**2014**), 215 (23), 22952304.
Author's contribution: NS was responsible for planning, performing and evaluating the refractometric, affinity and specificity measurements. NS wrote the main part of the paper. CP synthesized the polymers. GT provided the moleculary imprinted polymer nanoparticles.

Contents

List of Figures

List of Tables

1 Introduction

The craving for knowledge has driven the human race to explore the materials unexplored and know the unknowns. Since the day sun has set its light on earth, mankind has been mesmerized by its different effects and appearances. Blue color of sky and appearance of color bands in rainbow has always been fascinating and poetic experience. First encounter of sunlight and subsequent appearances of shadow must have intrigued him to find out the underlying cause. The desire to detect the events or changes in its environment, and observe its corresponding output has driven him to make various sensory devices. In modern world, optical sensors has becomes progressively exploited technology in important fields such as environmental monitoring, medical diagnostics, food safety and security.

Gobal research and development (R&D) in last 30 years has expanded exponentially in terms of financial investment, the published literature, and the number of active researchers on the field of sensors. Sensor devices capable of rapid, selective and sensitive detections of biomarkers, pathogens and toxic substances with simple operation are strongly desired in clinics, food industries and environmental monitoring facilities which can be a target of bio-terrorisms. Thus, a near revolution is apparent in sensor research, giving birth to a large number of sensor devices for medical and environmental technology. With this paced development taking place, there is an urgent need to explore new materials which can have the required properties to be used in sensors.

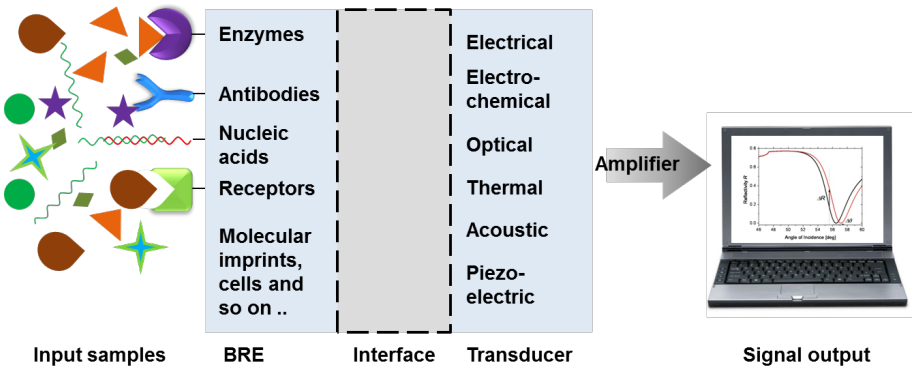

Figure 1.1: Schematics of a typical biosensor.

1.1 Biosensor

According to IUPAC, biosensor is a device that uses specific biochemical reactions mediated by isolated enzymes, immunosystems, tissues, organelles or whole cells to detect chemical compounds usually by electric, thermal, or optical signals [1]. Soon after the development of the first biosensor by Clark in 1962 [2] many efforts have been made to take advantage of the unique recognition and signal-amplification abilities of biological systems that have evolved over millions of years with detection and amplification system. The most common format of a biosensor relies on bio-recognition elements (BRE) immobilized on the sensor surface in order to specifically capture target analyte contained in a sample solution. Interfacing BRE on sensor surface requires ample dexterity and therefore, understanding the surface chemistry is an important issue. For instance, a non-fouling layer offers great feasibility to minimize nonspecific absorption of molecules from the sample onto the sensor surface, thus to distinguish the specific signal from the noise and improve the sensitivity and specificity of the biosensors. The potential of biosensor technologies to provide high sensitivity, high specificity and miniaturized devices for rapid and economical detection of range of important analytes has generated intense commercial interest. Among these biosensors, the most commonly used biosensor schemes are based on optical [3–6] and electrochemical transducers [7–12].

A typical biosensor consists of three parts, as seen in Figure (1.1):

1. BRE, that specifically interact with target analyte, which are typically biological materials, such as enzymes, antibodies, nucleic acids, cell receptors, organelles, tissue, and whole

cells, or biomimic materials.

2. Transducer, that transforms the interactions of BRE with analyte into a measurable electrochemical, optical, thermometric, piezoelectric or magnetic signal.

3. Signal output system, that is primarily responsible for the processing and display of sensor output.

1.1.1 Optical Biosensor

Over the last three decades the field of optical biosensors have made tremendous advancement in terms of development and application of technology that was gradually pushed forward to provide high sensitivity, real-time monitoring of molecules interactions, and rapid signal read-out. The methods that are prominently used include fluorescence spectroscopy [13], Raman spectroscopy [14], optical waveguide spectroscopy (OWS) [15], ellipsometry [16], reflectometry [17] and surface plasmon resonance (SPR) [3, 18, 19]. Among these optical methods, SPR has established itself as a widely employed analytical method which in conjunction with appropriate BRE can be tailored for label-free biomolecular interaction analysis (BIA) and detection of chemical and biological compounds. Since the first demonstration of SPR for the observation of processes at the surface of metal and sensing of gases [20] in the early 1980s, SPR biosensor have become a popular technique for monitoring and quantifying bimolecular interactions in real-time. Consequently, SPR sensing technology has been commercialized [21] by various companies including Biacore [22], Windsor [23] and Bionavis [24].

1.2 Surface Plasmon

Surface plasmons (SPs), also known as surface plasmon polaritons (SPPs), are surface electromagnetic waves that propagate in a direction parallel to the metal/dielectric interface. Surface plasmon resonance (SPR) was first observed by R.W. Wood in year 1902 by illuminating metallic grating with polychromatic light beam. The observed diffraction spectra exhibit dark bands which he describes as one of "the most interesting thing ever met" [25] and this were later attributed to the excitation of SPs. Andreas Otto in 1968 demonstrated it by bringing the quartz-glass substrate coated with silver in contact with quartz prism and attributed the dip

in the reflectivity spectra to the excitation of SP [26]. In the year 1968, E. Kretschmann and H. Raether reported the excitation of SP by covering the one side of glass prism with silver film [27]. In years that follows, SP as an useful tool and its fundamental theory of the excitation for different configuration and their investigation was established by researchers, thereby introducing SPs into modern optics. Initially SPR was used for thin film characterization tool [28], study at interfaces [29], afterwards it has flourished into a full fledged interdisciplinary fields involving non-linear optics [30], semiconductor laser [31–34], optical data storage [35], photonic bandgap structures [36–38], nanostructures [39], sensors [3, 18, 20, 40].

1.3 Electromagnetic Theory of Surface Plasmon

This section presents the electromagnetic theory of SP and provides theoretical model for light propagating along metal-dielectric interfaces. Important concepts for understanding the propagation of SPs and methods for their optical excitation are discussed.

Surface plasmon originates from the coupled oscillations of electromagnetic field and density of electron plasma on a metal surface. From Maxwell's equations with standard boundary conditions, it can be shown that planar metal-dielectric interface supports existence of guided SP mode [41]. It's dispersion relation can be expressed as :

$$\beta = k_0 \sqrt{\frac{\varepsilon_m \varepsilon_d}{\varepsilon_m + \varepsilon_d}}, \tag{1.1}$$

where β is the SP propagation constant, $k_0 = 2\pi/\lambda = \omega/c$ is the propagation constant of light in vacuum with an angular frequency ω, wavelength λ and velocity of light in vacuum c. ε_d and $\varepsilon_m = \varepsilon_m^{'} + i\,\varepsilon_m^{''}$ are the permittivity of dielectric and metal, respectively. From the boundary conditions of Maxwell's equation it follows that SP exist only in transverse magnetic (TM) polarization for which the magnetic intensity vector is parallel to the metal surface. Since ε_m is a complex quantity, β is also complex. Additionally, SP exist at frequencies for which $\mathrm{Re}\{\varepsilon_m\} < 0$ and $|\mathrm{Re}\{\varepsilon_m\}| > \varepsilon_d$. Metals such as gold, silver and aluminum have negative real part of their complex permittivity (i.e. $\varepsilon_m^{'} < 0$) which supports SPs. Expressing the metal permittivity using Drude's model, the existence of SP at interface between metal and dielectric is fulfilled below the plasma frequency ω_p. This implies that for $\omega < \omega_p$ no electromagnetic

field can propagate in a metal.

If the magnitude of the real part of the permittivity of metal is greater than the imaginary part; $\left|\varepsilon_m^{'}\right| > \varepsilon_m^{''}$, then equation (1.1) can be expressed as:

$$\beta = \mathrm{Re}\{\beta\} + i\,\mathrm{I}m\{\beta\} = \frac{\omega}{c}\sqrt{\frac{\varepsilon_d\varepsilon_m^{'}}{\varepsilon_d+\varepsilon_m^{'}}} + i\frac{\varepsilon_m^{''}}{2(\varepsilon_m^{'})^2}\frac{\omega}{c}\left(\frac{\varepsilon_d\varepsilon_m^{'}}{\varepsilon_d+\varepsilon_m^{'}}\right)^{3/2}, \tag{1.2}$$

where $Re\{\}$ and $\mathrm{Im}\{\}$ denote the real and imaginary part of the complex number, respectively. Imaginary part of the propagation constant is associated with the attenuation of the SP propagation. The attenuation is characterized by the propagation length L, which is defined as the distance in the direction of propagation at which the energy of the SP decreases by a factor of $1/e$:

$$L = 1/2\mathrm{Im}\beta, \tag{1.3}$$

Geometry depicted in Figure 1.2(a) with Cartesian coordinate z being perpendicular to the metal/dielectric interface is used. Metal is in the region $z<0$ and the SP is propagating along the $x-$ axis parallel to the interface. The electromagnetic field of the SP (TM mode) then can be expressed as:

$$\vec{E}_m = (E_{xm}, 0, E_{zm})exp[i(\beta x + k_{zm}z - \omega t)], \forall z < 0, \tag{1.4}$$

$$\vec{H}_m = (0, H_{ym}, 0)exp[i(\beta x + k_{zm}z - \omega t)], \forall z < 0, \tag{1.5}$$

$$\vec{E}_d = (E_{xd}, 0, E_{zd})exp[i(\beta x - k_{zd}z - \omega t)], \forall z > 0, \tag{1.6}$$

$$\vec{H}_d = (0, H_{yd}, 0)exp[i(\beta x - k_{zd}z - \omega t)], \forall z > 0, \tag{1.7}$$

where $\vec{E}$ and $\vec{H}$ are the electric and magnetic field vectors, respectively.

Surface plasmon propagates along the metal surface with its field exponentially decaying into both metal and dielectric medium with transverse propagation constant $\sqrt{k_0^2\varepsilon_m - \beta^2}$ and $\sqrt{k_0^2\varepsilon_d - \beta^2}$ in the metal and dielectric, respectively. The field decay in the direction perpendicular to the metal-dielectric interface is characterized by the penetration depth

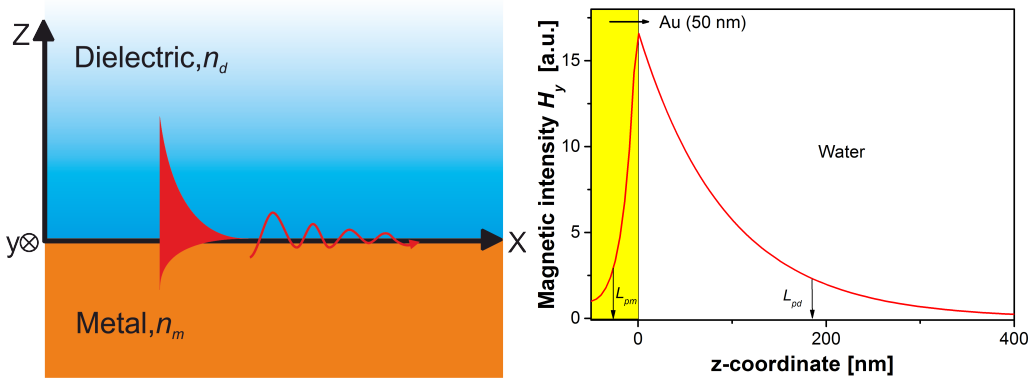

(a) (b)

Figure 1.2: (a) Schematic presentation of a surface plasmon at the interface between a metal and a dielectric. (b) Distribution of magnetic field of a surface plasmon at the interface of gold ($\varepsilon_m = -12 + i1.5$) and dielectric ($\varepsilon_d = 1.78$), wavelength $\lambda = 633$ nm, with the penetration depth $L_{pd} = 183$ nm, $L_{pm} = 27$ nm, and propagation length $L_x = 7200$ nm (Image reproduced from [42]).

L_p, which is defined as the distance from the interface at which the amplitude of the field decreases by a factor of $1/e$. Penetration depth for the metal can be expressed as,

$$L_{pm} = 1/|k_{zm}| = \frac{1}{k_0}\frac{\sqrt{\varepsilon_m + \varepsilon_d}}{\varepsilon_m}, \tag{1.8}$$

and for the dielectric,

$$L_{pd} = 1/|k_{zd}| = \frac{1}{k_0}\frac{\sqrt{\varepsilon_m + \varepsilon_d}}{\varepsilon_d}, \tag{1.9}$$

1.4 Excitation of Surface Plasmon

From the Equation (1.2), it follows that the real part of the propagation constant $\mathrm{Re}\{\beta\}$ is always higher than the one of the optical waves propagating to the far field, see Figure (1.3). The SP dispersion curve (C) in Figure (1.3) approaches the light line (A) at low frequencies, whereas at high frequency it approaches the cutoff angular frequency $\omega_{max} = \omega_p/\sqrt{1+\varepsilon_d}$. This implies that, these waves can not be phase matched along the metal surface and direct coupling between them is not possible. In order to optically excite SP, a coupler providing enlargement of the optical wave's momentum needs to be employed. To achieve this, two types of couplers are used. The first is by using a *prism coupling* employing the attenuated

total reflection (ATR) and the second is *grating coupling* using diffraction of light on periodic modulated metallic surfaces to achieve the momentum matching condition.

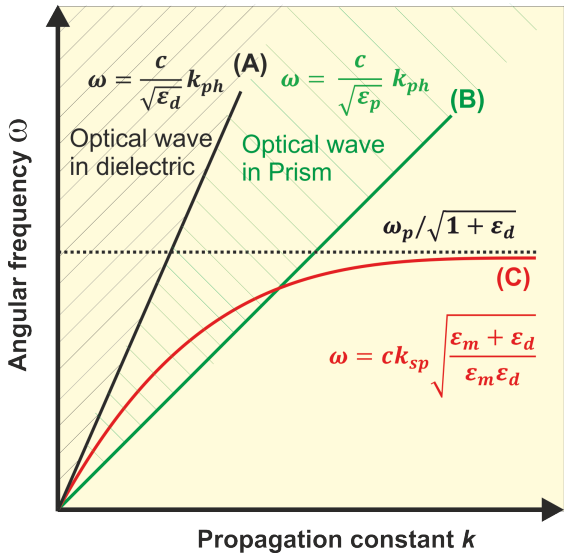

Figure 1.3: Curve (A) and (B) show typical dispersion relation of a free photon propagating inside a dielectric and in a coupling prism with $\varepsilon_p > \varepsilon_d$, respectively in order to compare with the SP dispersion. Curves (C) shows the dispersion relation of SP at the interface between metal and dielectric.

1.4.1 Prism Coupling

There are two configurations of the ATR method- Kretschmann configuration [27] and Otto configuration [26].

In the Kretschmann configuration of the ATR method, a high refractive index prism with refractive index[1] n_p (e.g. BK7 or LASF9 glass) is interfaced with a metal-dielectric waveguide consisting of a thin metal film with permittivity ε_m, and a semi-infinite dielectric with a refractive index n_d ($n_d < n_p$), see Figure (1.4). When a light wave propagating in the prism is made incident at an angle[2] $\theta > \theta_c$ on the metal film a part of the light is reflected back into the prism and a part tunnels through the metal in the form of an evanescent wave. If the metal film is sufficiently thin (noble metals such as Au, Ag, $\cdots$ with thickness less than 100 nm for light in visible and near infra-red part of spectrum), the evanescent wave penetrates through the metal film and couples with a surface plasmon at the outer boundary of the metal film.

[1] Permitivity ε and refractive index n satisfy $\varepsilon = n^2$
[2] The critical angle (θ_c) is the angle of incidence above which the total internal reflection occurs.

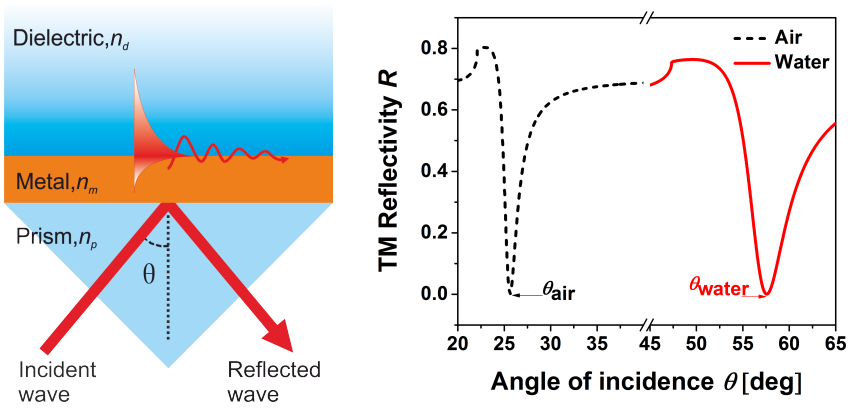

Figure 1.4: (a) Schematic of attenuated total reflection method with the Kretschmann configuration for the excitation of surface plasmon, and (b) the angular reflectivity spectra for 47 nm of Au ($n_{Au} = 0.18 + i\,3.43$) [43] on a prism base $n_p = 1.845$ in air $n_{\text{air}} = 1$ (dots), and water $n_{\text{water}} = 1.333$ (solid), at wavelength $\lambda = 632.8$ nm.

Excitation of SP occurs, when the propagation constant of SP at the interface between metal and dielectric with a lower refractive index is matched to the one of the incident optical wave:

$$\frac{\omega}{c} n_p \sin(\theta) = Re\{\beta\}, \tag{1.10}$$

This phase-matching between the incident photon and the SP is referred to as surface plasmon resonance (SPR). On the dispersion curve in Figure (1.3), this defines an operating point in which the frequency and the wave vector of both the exciting light and the plasmon are determined [44]. The strength of the coupling between an optical wave and surface plasmon wave can be controlled by varying the thickness of the metal layer. The excitation of the SP manifest itself as a narrow absorption dip in the angular (or wavelength) reflectivity spectrum. The minimum in the reflection as can be seen in Figure (1.4)(b) is highly sensitive to the optical properties of the adjacent dielectric. The spectral position of the SPR dip can be determined from the phase-matching condition (Equation (1.10)). As follows from this equation, SPR dip is a function of refractive index ε_d of the dielectric on the metal surface, as:

$$\theta = sin^{-1}\,\text{Re}\left\{\sqrt{\frac{\varepsilon_m \varepsilon_d}{(\varepsilon_m + \varepsilon_d)\varepsilon_p}}\right\}, \tag{1.11}$$

The angular spectrum of reflectivity Figure (1.4)(b)) and field distribution can be calculated based on Fresnel equations and transfer matrix formalism described in literature [45–49].

1.4.2 Grating Coupling

In grating coupling, diffraction on a periodically modulated metallic surface is employed to match propagation constants of an optical wave and SP. As shown in Figure (1.5)(a), light beam hit the metallic grating with a period Λ at an incident angle θ. This approach can be explained using the Floquet theorem by means of which dispersion relations of a SPW and an optical wave are described as folded in the first Brillouin zone, see Figure (1.5)(b).

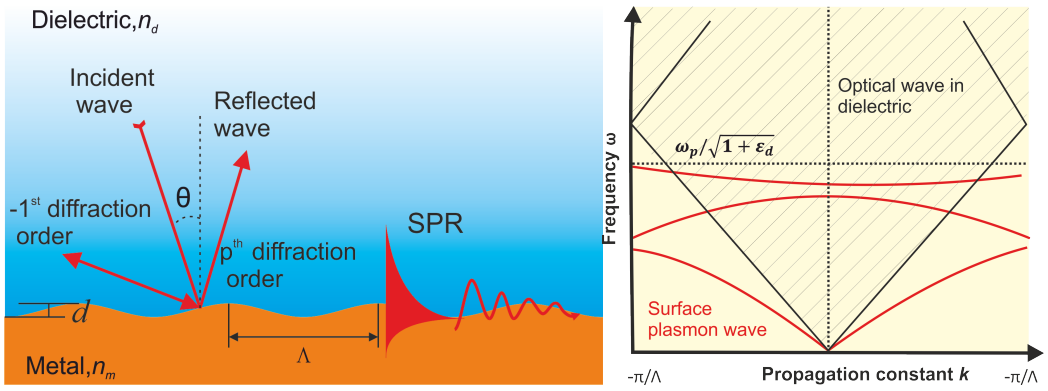

(a) (b)

Figure 1.5: (a) Schematic presentation of SP along periodically corrugated metal-dielectric interface diffraction coupled to an optical wave propagating in the dielectric. (b) Dispersion relation of SP propagating along a periodically modulated metal-dielectric interface with the dispersion relation of an optical wave in the dielectric (dashed region).

In this zone, the propagation constant of a SP and the one of an optical wave propagating in the dielectric lie between $-\pi/\Lambda$ and π/Λ. Due to the folding of dispersion relations, component of the propagation vectors of a SP and of an optical wave parallel to the grating surface can be matched at certain frequencies, see Figure (1.5). These frequencies fulfill following momentum matching conditions:

$$\frac{\omega}{c} n_d \sin(\theta) + p\frac{2\pi}{\Lambda} = \pm Re\{\beta\}, \tag{1.12}$$

where the first term ($\frac{\omega}{c} n_d \sin(\theta)$) on the left hand side represents the component of the propagation constant of the incident light beam that is parallel to the grating surface, and the second term on left side is due to the contribution of diffraction and p is an integer. The integer $p \neq 0$ is indexing the order of diffracted wave. The strength of coupling between an optical wave and a SP is mainly affected by the profile and depth of the modulation of grating surface.

Note that the grating constant Λ should be within the same order of magnitude as the wavelength of the incoming light, given the fact that SPR coupling via the first diffraction order ($p = \pm 1$) is significantly more efficient than via higher orders. A shallow grating with amplitude of several tens of nanometers is typically sufficient for efficient coupling to SPs. As follows from condition (1.12), the position of SPR dip or peak is a function of permittivity ε_d of the dielectric adjacent to the metal surface.

1.4.3 Field Enhancement

Upon the coupling of SP and dielectric waveguide modes, energy of incident wave is accumulated on a surface and the intensity of electromagnetic field is enhanced. The value of this enhancement factor K can be given by the ratio of the magnetic field intensity on the metal surface at the dielectric side divided by the incoming magnetic field intensity, i.e. the light intensity at the interface $|H_s|^2$ to the incoming light intensity $|H_0|^2$ ($K = |H_s|^2 / |H_0|^2$). For a mere total internal reflection (TIR) geometry, e.g., a glass water interface, the reflectivity R and enhancement factor K, as function of angle of incidence θ, can be calculated as shown in Figure (1.6)(a). The enhancement factor of this geometry is maximum of K =4 at the critical angle θ_c. Moreover, if prism base is coated with a 50 nm of Au to support SPs, then the enhancement factor K is increased to 16 due to the contribution of SPs as seen in Figure (1.6)(b) at wavelength $\lambda = 633\,\text{nm}$.

1.5 SPR Biosensors

Surface plasmon resonance as a tool for sensing was first reported in 1982 as a gas sensor [20, 51]. Thereafter, SPR has been extensively used for measurement in the field of food quality and safety analysis [52–56], medical diagnostics [57–60], environmental monitoring [61–63]. Ability

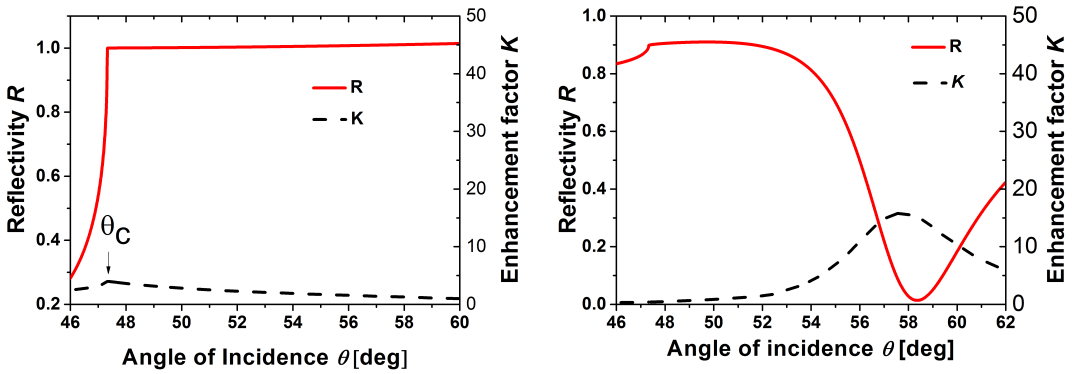

(a) (b)

Figure 1.6: Reflectivity (R) and the intensity enhancement factor K as the function of the angle of incidence θ for (a) total internal reflection (TIR) at a glass-water interface, and (b) a surface plasmon polariton excitation at a gold-water interface (with d_{Au} = 50 nm, $n_{Au} = 0.21 + i3.32$) (Reproduced from [50]).

of SPR sensors for direct, label free and real time detection has found interest in detection of chemical and biomolecular compounds [19] and in biomolecular analysis are recently the major and most rapidly evolving areas [3, 18].

1.5.1 Principle of SPR Biosensor

In SPR biosensor, SP is excited at the interface between a metal film and a sensitive layer, changes in the refractive index of which are to be measured. Any change in the refractive index of the sensitive layer produces a change in the propagation constant of the surface plasmon. This change alters the coupling condition between a light wave and the surface plasmon, which can be observed as a change in one of the characteristics of the optical wave interacting with the surface plasmon [18]. Classification of SPR sensor depends upon the type of properties it uses of light wave to interact with SP, accordingly it can be classified as SPR sensors with angular, wavelength, intensity, phase, or polarization modulation [64].

In SPR sensors with angular modulation a monochromatic light wave excites a surface plasmon. The strength of coupling between the incident wave and the surface plasmon is observed at multiple angles of incidence of the light wave and the angle of incidence yielding the strongest coupling is measured and used as a sensor output. The binding of the analyte molecules to bio-recognition element (BRE) which is immobilized in the sensitive layer (e.g.

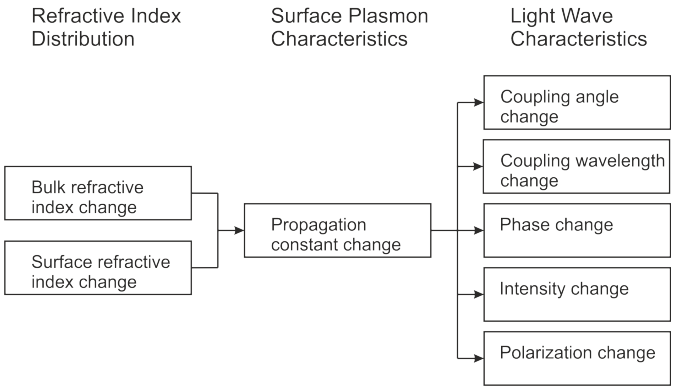

Figure 1.7: Concept of surface plasmon resonance sensors (Reproduced from [64])

hydrogel thin layer) induces a change in the refractive index in the vicinity to the metallic surface δn which produces a change of propagation constant $\delta\beta$ and consequently changes the coupling condition to SPs, as indicated in Equations (1.1), (1.12) and (1.10). Thus the molecular binding events are monitored as a shift in the angular SPR reflectivity dip $\Delta\theta$, or the reflectivity changes ΔR at an angle set in the vicinity of the resonance see Figure (1.7).

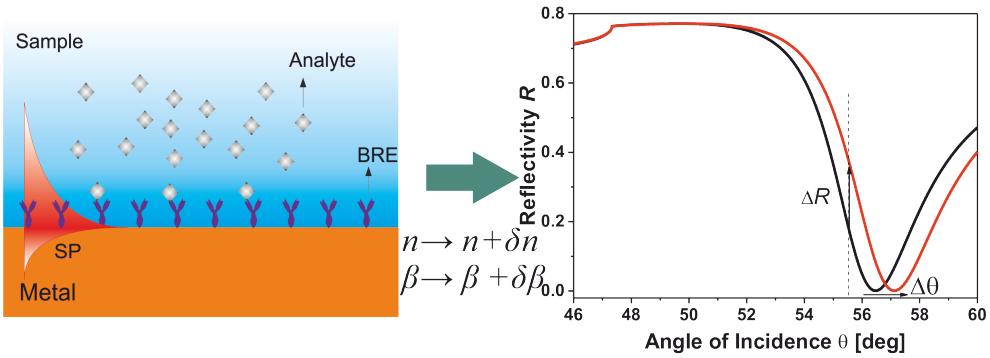

Figure 1.8: Schematic of the operation of SPR biosensors measuring the binding induced refractive index changes as a shift in the SPR resonant angle $\Delta\theta$, or the changes of reflectivity ΔR

The strength of the refractive index change δn induced by the analyte molecules binding to the bio-recognition elements depends on the volume refractive index increment $\left(\frac{dn}{dc}\right)_{vol}$ and can be expressed as:

$$\delta n = \left(\frac{dn}{dc}\right)_{vol} \Delta c_b \tag{1.13}$$

where Δc_b is the concentration of bound analyte expressed in mass per unit volume. For a

thin layer of thickness h, the refractive index change can be rewritten as:

$$\delta n = \left(\frac{dn}{dc}\right)_{vol} \frac{\Delta\Gamma}{h} \tag{1.14}$$

where Γ denotes the surface concentration in mass per unit area [16] and $\frac{dn}{dc}$ is a constant, that has value $0.2\,\mathrm{mm^3\,mg^{-1}}$ for measuring of biomaterials.

1.5.2 Characteristics of SPR Biosensors

The main characteristics describing the performance of SPR biosensors include sensitivity, resolution, limit of detection and figure of merit.

Sensitivity

Sensitivity is the ratio of the change in sensor output to the change in the measurand. In a SPR sensor with angular modulation the sensitivity $S_{\theta b}$ to the bulk refractive index changes δn_b can be expressed as:

$$S_{\theta b} = \frac{\delta\theta_r}{\delta n_b} \tag{1.15}$$

where θ_r is the resonance angle at which the reflectivity is minimum. For SPR affinity biosensors, the molecular binding events induced change in the refractive index typical occurs only within a very short distance d from the sensor surface. Assuming $d << L_{pd}$, thus an effective bulk refractive index change which is seen by a SP mode can be expressed as:

$$\delta n_b = \delta n_s \frac{2d}{L_{pd}} \tag{1.16}$$

where δn_s is the refractive index change in the film with thickness d.

In the intensity modulation, one typically monitors the reflectivity changes at an angle $\theta < \theta_r$ where the slope $S_{R\theta} = \frac{\Delta R}{\Delta\theta}$ is linear (see Figure (1.7)). Thus the reflectivity sensitivity of SPR

biosensor to the bulk refractive index changes can be written as:

$$S_{Rb} = \frac{\delta R}{\delta n_b} = \frac{\delta \theta_r}{\delta n_b} S_{R\theta} = S_{\theta b} S_{R\theta} \tag{1.17}$$

Resolution

Resolution of a SPR sensor is the smallest change in bulk refractive index which produces a detectable change in the sensor output. The magnitude of sensor output change that can be detected depends on the level of uncertainty of the sensor outputs, the output noise. In this study, intensity modulation is used for monitoring the refractive index changes. The resolution of a SPR sensor, r_R, is typically expressed in terms of the standard deviation of the noise of sensor output, σ_R, translated to the refractive index of bulk medium,

$$r_R = \frac{\sigma_R}{S_{Rb}} \tag{1.18}$$

where S_{Rb} is the bulk refractive index sensitivity.

Limit of Detection

The limit of detection (LOD), as defined by the International Union of Pure and Applied Chemistry (IUPAC), is the concentration of analyte c_L derived from the smallest measure Y_L that can be detected with reasonable certainty. The value of Y_{LOD} is given by the equation:

$$Y_{LOD} = Y_{blank} + m\sigma_{blank} \tag{1.19}$$

where Y_{blank} is the mean of the blank (sample with no analyte) measures, σ_{blank} is the standard deviation of the blank measures, and m is a numerical factor chosen according to the confidence level desired (typically 2 or 3) [65]. As $c_{blank} = 0$, the LOD concentration c_{LOD} can be expressed as:

$$c_{LOD} = \frac{1}{S_c(c=0)} m\sigma_{blank} \tag{1.20}$$

where S_c denotes the sensor sensitivity to analyte concentration.

Figure of Merit

As the sensitivity is defined by detecting either the wavelength or the intensity shift of the plasmon dip that occurs upon a change in the refractive index close to the sensitive surface layer. However, a determination of the plasmon dip minima requires a mathematical calculation that depends on the spectral width of the plasmon dip and the intensity of the signal, or more accurately the noise level in the signal. It is therefore necessary to introduce a term that includes resolution in order to make a fair comparison between different surface layer since the peak width can vary significantly. This has led to the introduction of a new parameter known as figure of merit (FOM) that includes both sensitivity and resolution. FOM is defined as the ratio between the bulk refractive index sensitivity and the spectral width, expressed as:

$$\chi = \frac{S}{\Delta\theta_{FWHM}} = \left(\frac{\delta\theta_r}{\Delta\theta_{FWHM}} \frac{1}{\delta n_b}\right) \tag{1.21}$$

where θ_{FWHM} is the change in the spectral width at full width at half minima (FWHM).

1.6 Thin Hydrogel Film

Hydrogels are cross-linked polymer networks absorbing large quantities of water without dissolving. Softness, smartness, and the capacity to store water make hydrogels unique materials [66, 67]. The ability of hydrogels to absorb water arises from hydrophilic functional groups attached to the polymer backbone while their resistance to dissolution arises from cross-links between network chains. Hydrogels has been proposed as a support matrix that can accommodate large amounts of molecules with specific functions. The polymer networks provide support to one partner of an affinity binding pair, e.g. an antigen and easy mobility to the analyte upon addition of the analyte solution, i.e. an antibody. This approach takes advantage of the three-dimensional open architecture of the swollen hydrogel to increasing the binding capacity of the surface architecture for the capture of target analyte. Responsive hydrogels exhibit drastic volume changes in response to specific external stimuli, such as changes in temperature, pH values, ionic strengths, light intensity, electric fields [68–71].

Such stimuli-sensitive hydrogels have been intensively studied with respect to drug delivery systems [68, 72–80] and other biomedical application and medicine technique, like cell encapsulation and tissue engineering applications [81], therapeutics [82], production of soft contact lenses [83], medical dressings [84], artificial kidney [85] and artificial muscles [86] because of their low toxicity and high biocompatibility. Furthermore, mechanical strength of the hydrogel has been shown to perform work on the micro and macroscale [87].

Hydrogels application in biosensor technologies has allowed great improvements in the performance for detection of chemical or biological analytes [88–91] where it has been implemented at the interface between an analyzed sample and a transducer. Typically, hydrogels are modified with BREs such as antibodies, enzymes, or biomimetic moieties based on molecular imprinting in order to specifically recognize target analytes present in a liquid sample (Figure (1.9)). Compared with other types of biointerfaces (e.g., based on self-assembled monolayers [SAMs]), hydrogels can accommodate orders-of-magnitude larger amounts of recognition elements and provide a more natural microenvironment for biomolecules, which increases their stability and offer routes for implementing additional functionalities (e.g., separation of target analyte from other molecules in a sample, simplified methods for readout). In addition, the class of "smart" gels that can respond to external stimuli (e.g. temperature or pH changes) holds potential for development of biosensors with enhanced sensitivity and implementing of new biosensor schemes for sensitive analysis of molecular analytes [92–94]. For instance, miniature hydrogel sensor elements were integrated in a contact lens for the analysis of glucose in tear fluid. The hydrogel element served both as a host for recognition elements and as an optical transducer for detection of glucose [95].

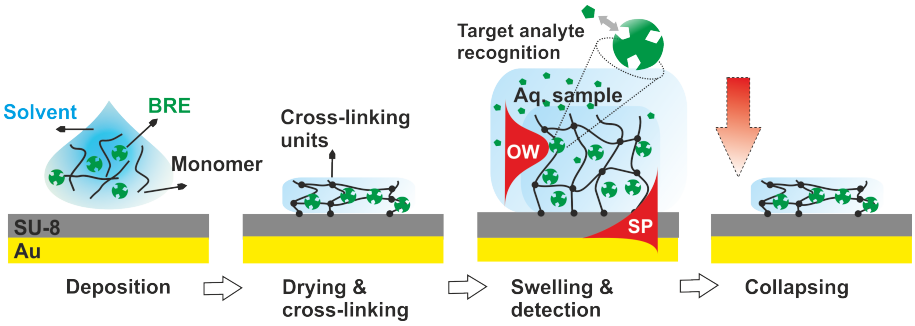

Figure 1.9: Concept of biosensor surface modification with hydrogel.

Work in this thesis has been performed on poly(N-isopropylacrylamide) (pNIPAAm)-based hydrogel, which is the most commonly used polymer based hydrogels [96] having the ability to respond to temperature change undergoing reversible phase transition, [80,97,98] and exhibits a well defined lower critical solution temperature (LCST) in water around 31–34 °C [71,72] which is close to the body temperature. It can be conveniently synthesized in multi-gram amounts by free radical polymerization [99,100]. Since pNIPAAm has both hydrophilic (amide) groups and hydro- phobic (isopropyl) groups, hydrogen bonds between pNIPAAm and water are strong to show hydrophilicity and a mixture of pNIPAAm and water is a homogeneous solution as the temperature is below the LCST. On the contrary, as the temperature is above LCST, the interaction within pNIPAAm is stronger than the hydrogen bonds between pNIPAAm and water to show hydrophobicity and the mixture appears to be a heterogeneous solution. Therefore, pNIPAAm is widely used as a thermo-sensitive carrier to control drug activity.

1.6.1 Diffusion of Target Analyte

In biosensor applications, hydrogel materials are employed at an interface between an analyzed aqueous sample and a transducer. Typically, the hydrogel interface is modified with biomolecular recognition elements (BREs) such as antibodies, enzymes or with bio-mimetic molecular imprinted moieties in order to specifically recognize target analytes. Highly sensitive biosensors that detect analytes at extremely low concentration levels or recognize environmental changes arising from biological processes are crucial for the early detection of diseases and prognosis. In order to reach fast detection times, target analytes have to rapidly diffuse through the hydrogel binding matrix and react with incorporated recognition elements. The mesh size ξ and the molecule hydrodynamic radius r_h are the key parameters affecting the diffusion-driven mass transport in gels in which the diffusion coefficient scales as $D_g \sim exp(-r_h/\xi)$. In highly swollen gels with $r_h \ll \xi$, D_g of mobile target molecules is close to that in water and the recognition elements in hydrogels are easily accessible for the binding. However, diffusion is dramatically hindered by steric and hydrodynamic interactions when the size of the mobile molecules is comparable to the mesh size $r_h \sim \xi$. The distance between polymer crosslinks provides a measure for the mesh size ξ and it is related to the hydrogel swelling ratio (SR) defined as the ratio of the thickness in swollen (hydrated) and

collapsed (dry) state. The swelling ratio SR is inversely proportional to the polymer volume fraction *f*. These parameters can be controlled through the gel composition and cross-linking density. [101] The characteristic time of the hydrogel response to the stimuli scales with its size Δx and diffusion coefficient D of the network as $\sim \Delta x^2/D$, where D is in the order of $10^{-4} - 10^{-6}\,\mathrm{mm^2 s^{-1}}$ for most common gels [91].

1.6.2 Structured Hydrogels

The use of three-dimensional (3D) hydrogel Structures are becoming increasingly important in applications such as cell culturing, development of scaffolds for tissue engineering, and high-throughput assay platforms with microarray detection format (e.g. 2D cell cultures do not properly imitate the micro-ambiance of three-dimensionally organized native tissue) [102]. The ability to structure 3D hydrogels with controlled geometry and feature sizes is important since pore size and shape strongly impact cell behavior in many biomedical applications such as tissue engineering and biosensors [103, 104]. Until now, numerous methods for structuring of hydrogels on a surface were developed including those based on microfluidics [105], photolithography [106–108] or soft-lithography-based techniques [109–111]. Among these techniques, laser interference lithography (LIL) and nanoimprint lithography (NIL) are easy to use and suitable for fabricating large scale area. Optical diffraction has been introduced as a technique to investigate the periodically patterned hydrogel films. It was later shown that the diffraction efficiency could be greatly enhanced by using SP as the diffracted electromagnetic wave [112]. The reversible swelling and collapsing of the structured hydrogel triggered by an external stimulus leads to an increase in the refractive index contrast on a grating, which manifested in enhancing the diffraction efficiency of the grating. [112]

As seen in Figure (1.10), light beam from a laser source is coupled to a high-refractive-index prism and SPs are excited at its base by using the ATR method with Kretschmann configuration. The angle of incidence of the excitation light beam, θ, is set to an edge of an SPR dip with a high slope $\delta\theta/\delta\theta$ (see Figure (1.8)). Because of the changes in the local environment of structured hydrogel, refractive index changes occurs, which in turn causes the variation of coupling strength of SPs at a given angle of incidence across the sample. Thus, the intensity of a reflected light beam is modulated by the hydrogel structure and can be observed by a

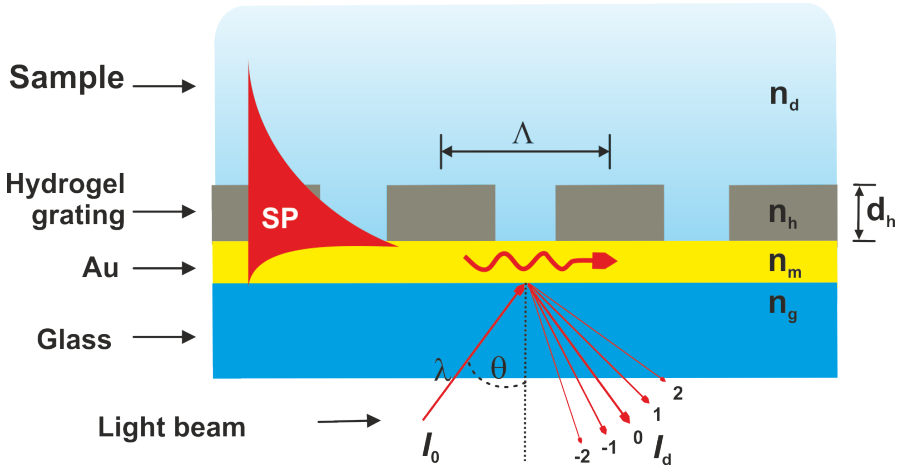

Figure 1.10: Schematics of a SP-enhanced diffraction for the investigation of periodically patterned hydrogel films.

detector. For detail description see the section (4.2.5).

1.6.3 Hydrogel Optical Waveguide Modes

In an asymmetric planar slab waveguide structure with a thin dielectric film attached to the metal surface such that its permittivity ε_f is greater than that of adjacent top dielectric medium (ε_d), additional guided optical waves can be observed as shown in Figure (1.11).

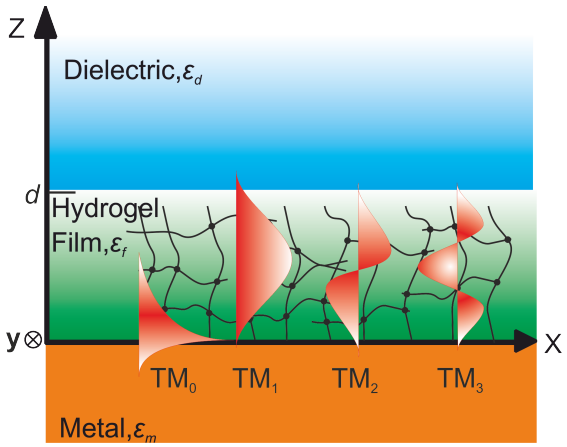

Figure 1.11: Schematics of optical waveguide modes on a structure with metal (ε_m), film (thickness d, ε_f), and dielectric (ε_d).

The considered planar structure comprises of a dielectric film (permittivity of ε_f and thickness of d) sandwiched between a substrate (metal, ε_m) and a superstrate (dielectric, ε_d). The

boundary conditions of Maxwell's equations require that the components of the electric and magnetic field intensity vectors parallel and perpendicular to the boundaries [3] of the wave-guiding layer are continuous at the boundaries ($z = 0$ and $z = d$). According to these conditions, one can derive the dispersion relation of guided waves propagating with distinct propagation constant β which fulfills the following relations:

$$\tan(kd) = \frac{\gamma_d/k + \gamma_m/k}{1 - (\gamma_d/k)(\gamma_m/k)}; \text{for TE modes,} \tag{1.22}$$

$$\tag{1.23}$$

$$\tan(kd) = \frac{\gamma_d \varepsilon_f/k\varepsilon_d + \gamma_m \varepsilon_f/k\varepsilon_m}{1 - (\gamma_d \varepsilon_f/k\varepsilon_d)(\gamma_m \varepsilon_f/k\varepsilon_m)}; \text{for TM modes,} \tag{1.24}$$

where $k^2 = k_0^2\varepsilon_f - \beta^2$, $\gamma_m^2 = \beta^2 - k_0^2\varepsilon_m$, and $\gamma_d^2 = \beta^2 - k_0^2\varepsilon_d$ are the transverse propagation constants in the waveguide film, the metal and dielectric, respectively.

1.6.4 Optical Waveguide Spectroscopy

Optical waveguide spectroscopy (OWS) refers to a method of observation of guided waves supported by dielectric structures. The basic slab structure of a dielectric optical waveguide is a layer of transparent material with a refractive index (n), which is higher than its surroundings. The light is confined and propagates with low attenuation. The optical coupling depends on the dimension and refractive index of the different parts in the waveguide system. This makes optical waveguiding suitable for sensor applications. For example, adsorption of a small amount of analyte on the surface of the waveguiding layer can lead to a large change in the optical coupling conditions (see Figure (1.12)). Analysis of the coupling conditions (incident angle, and percent reflected light) gives quantitative information about the adsorbed analyte. Only light with specific momentum and energy may propagate in a waveguide. Depending on the thickness and refractive index of the waveguide system, more than one *mode* of such

[3] Normal components: $B_\perp$; $D_\perp$ are continuous,
Tangential components: $E_\parallel$; $H_\parallel$ are continous,
where $\vec{D} = \varepsilon_o \varepsilon_r \vec{E}$; $\vec{B} = \mu_o \mu_r \vec{H}$

guided light may be allowed. Analysis of multiple guided modes can give information on the structural properties of the adsorbed analyte layer.

OWS refers to the application of waveguide spectroscopy for sensing purposes using a 1-dimensional slab waveguide and using prism coupling through a semi- transparent metal film in the Kretschmann configuration [27]. Figure (1.11) shows the schematic of these layers with waveguide mode. The dielectric thin-film waveguide (typically > 500 nm) is prepared on top of a semi-transparent metal layer (e.g. 47 nm Au), which in turn is deposited on a BK7 (n = 1.515) or LASF9 (n = 1.845) glass substrate. Optical modes in the dielectric waveguide are confined in the thickness direction by the Au layer and the medium on top of the sample (e.g. air or aqueous). The glass substrate are attached to the back of prism (with refractive index n_p higher than the waveguide layer) with index-matched immersion oil. Laser light is directed through the prism/glass substrate assembly and impinges at an angle on the substrate side of the semi-transparent metal layer. The momentum of the incidence light is defined by the refractive index of the prism, and the component parallel to the surface can be adjusted by changing the incidence angle θ.

At most angles, light is reflected from the back of the metal film and detected by a photo-detector. Beyond the critical angle (θ_c) of total internal reflection (TIR), light is coupled into the waveguide at specific combinations of wavelengths and incidence angles if it satisfy the conditions (1.10) and (1.24). The different modes are referred to by the number of nodes in the propagating electric field and are excited in turn as the incidence angle (θ) is scanned in a $\theta - 2\theta$ configuration. If light is coupled into the waveguide and propagates through the dielectric thin-film layer, optical damping by the metal layer dissipates the energy as heat and little light can be back coupled by the symmetric prism. Thus, waveguide modes show up as sharp intensity minima in the reflected intensity (R) in a angular reflectivity spectra.

Spectroscopy of surface plasmon and hydrogel waveguide waves provides a powerful technique for in situ observation of hydrogel films. It allows real-time monitoring of changes in their characteristics such as thickness (d_h) and refractive index (n_h) that are associated with variations in optical properties. These parameters can be obtained by fitting a Fresnel reflectivity for a multilayer (e.g., based on transfer matrix formalism) to the measured reflectivity

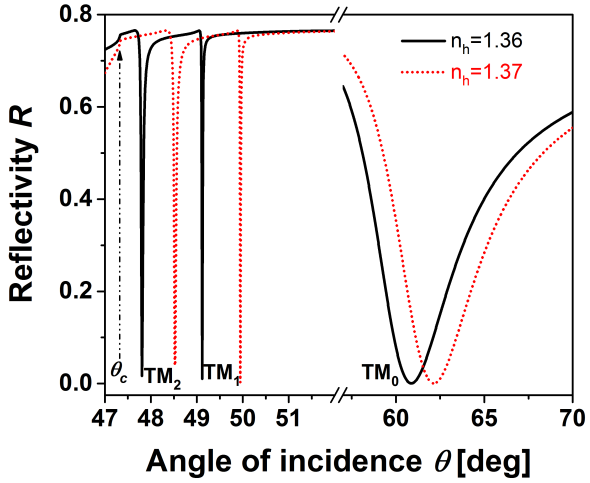

Figure 1.12: Simulated angular reflectivity spectra in water ($n_{water} = 1.333$) for the excitation of optical waveguide modes (TM_1 andTM_2) and surface plasmon (TM_0) on Au surface ($n_{Au} = 0.18 + i\,3.43, d_{Au} =$ 47nm) with a thin hydrogel layer ($n_h = 1.36, d_h = 2349$nm)

spectra $R(\theta)$ in which the hydrogel density is approximated by using a *box model*. In this model, the dependence of the refractive index perpendicular to the surface $n(x)$ is assumed to be the following function of the distance from the surface:

$$n(x) = n_d + (n_h - n_d)H(d_h - x)\,, \tag{1.25}$$

where x is the perpendicular to the sensor surface with $x = 0$ located at the interface between metal and hydrogel, H is the Heaviside step function. For small refractive index n_h of a hydrogel, its surface mass density from equation (1.14) can be expressed as:

$$\Gamma = (n_h - n_d) \times d_h \times \frac{\delta c}{\delta n_h}\,, \tag{1.26}$$

where the coefficient $\frac{\delta c}{\delta n_h} \sim 0.2 mm^3 mg^{-1}$ relates changes in the refractive index and concentration of organic materials in the gel (e.g., polymer or proteins). From the effective medium theory [46] follows that polymer volume fraction f of a swollen hydrogel is equal to:

$$f = \frac{(\{\mathrm{Re}(n_h)\}^2 - n_d^2)(\{\mathrm{Re}(n_{h-dry})\}^2 + 2n_d^2)}{(\{\mathrm{Re}(n_h)\}^2 + 2n_d^2)(\{\mathrm{Re}(n_{h-dry})\}^2 - n_d^2)}\,, \tag{1.27}$$

where n_{h-dry} is the refractive index of hydrogel in dry state.

In this study waveguide modes were excited at only one wavelength, using a He-Ne red laser operating at 632.8 nm.

2 Aim of this study

The goal of this thesis is advancing of plasmonics applications by combining of metallic structures with responsive hydrogel materials. In particular, the thesis aims at novel hybrid materials for direct detection of small molecules and at nanostructures that exhibit actively tunable plasmonic properties. It should be noted that up to now the majority of plasmonic nanostructures are static and their properties are fixed once they are prepared. Plasmonic nanostructures with actively adaptable properties holds potential to provide additional advantage and unleash the potential of plasmonics in various important areas ranging from bionanotechnologies (e.g. amplification of optical spectroscopy at tunable wavelengths) to highly integrated optical circuits (e.g. modulation of optical signal transmitted by confined field of surface plasmons). Among others, photo-crosslinkable *N*-isopropylacrylamide-based (pNIPAAm) polymer that can form thermo-responsive network is an attractive material for such research. This material can be reversibly switched between collapsed and swollen state by changing temperature around the lower critical solution temperature (LCST) which is accompanied by strong variations in refractive index as well as volume. Such materials provide an attractive platform for design of hybrid structures where spectrum of supported plasmon modes is controlled by tuning of near field coupling or directly by changes in the optical density. Methods for the grafting of responsive hydrogel networks to a gold surface, its structuring by using laser interference and nanoimprint lithography, and preparation of thin composite films are to be developed and characterized. Swelling behavior of structured hydrogel will be investigated and related to that of regular thin films. The developed structures will be applied in four projects.

1. Thermo-responsive pNIPAAm layer with arrays of nano-pillars on its top will be prepared and used to explore a difference between swelling that occur only in one direction (1D) and that occurring in three-dimensional (3D). Novel optical tool for investigation of such 3D and 1D swelling characteristics based on optical waveguide-enhanced diffraction spectroscopy will be carried out and the observed results will be compared to observation achieved by regular tools.

2. Dense pNIPAAm hydrogel grating will be prepared on a gold surface in order to actuate propagation of surface plasmons by their Bragg scattering. The reversible swelling and collapsing of the material is expected to switch "on" and "off" the grating which leads to opening and closing of a bandgap in surface plasmon dispersion relation. By this means, local density of states in vicinity to a metallic surface can be reversibly tuned which can find applications in optical spectroscopy (e.g. Purcell effect). In addition, such structure can act as a tunable mirror reflecting propagating surface plasmon beam in active plasmonics applications.

3. A thin metallic film with arrays of nanoholes exhibit unique optical properties associated with the coupling of light to surface plasmons that confine its energy in the nanoholes. These materials are pursued for application in e.g. optical filters relying on extraordinary transmission at narrow wavelengths or for optical sensing with "flow through" architecture when an analyzed liquid sample passes through the structure. In the present work we propose a novel structure where a thin perforated metallic film is attached to a solid support by using a responsive hydrogel cushion. This approach can provide means to reversibly change plasmonic properties (e.g. peak transmission wavelength) and actively flow aqueous sample through the pores triggered by the swelling and collapsing of the cushion.

4. Lastly, pNIPAAm is to be used as a glue to form a composite film with high density of polymer nanoparticles. In particular, molecular imprinted polymer nanoparticles (nanoMIP) are used in order to form a highly permeable layer with large surface area that can be used for efficient capture of target molecules by the imprinted moieties. Such approach is envisaged to dramatically improve the binding capacity of nanoMIPs that typically weakly interact with target small molecules. When the same film acts as a

waveguide, highly accurate optical waveguide spectroscopy (OWS) may provide means for sensitive direct detection of small molecules by nanoMIP which is not possible by regular surface plasmon resonance.

The thesis is structured into 7 chapters with the following outline. Chapters 4 to 7 describe the key results achieved in this thesis. Introduction chapter describes the concept of optical biosensor, theory of surface plasmon, excitation techniques, discussion about hydrogel and optical waveguide spectroscopy. The implementation of these guided waves to biosensor is discussed. In addition, estimation of the LOD, selectivity, resolution of SPR biosensor and an overview of hydrogel binding matrices applied in biosensors are presented. Chapter 3 titled as "Methods and Sample Preparation" covers experimental methods used in this thesis. All information about general sample preparations, used optics and instruments, and applied methods are introduced in this chapter. Protocols used for sample preparation including nanoimprint lithography, laser interference lithography, deposition of thin films, surface modification with self-assembled monolayer (SAM), template stripping and readout methods are presented.

3 Methods and Sample preparation

In the course of this work, several method were followed and equipment were used. Here a general idea about them is presented which will find recurrence in later chapters.

3.1 Optical Instruments

In this section, discussion about optical setups and equipments necessary to complete the projects has been done.

3.2 Preparation of Nanostructures

Preparation of nanostructures has become easier with advancement in technology including electron beam lithography, colloidal lithography, laser interference lithography (LIL) and nanoimprint lithography (NIL). Electron beam lithography is generally used for preparing prototypes with sub-10 nm resolution [113].

However, many of these techniques requires extensive amount of time and money and produces writing area in micro to millimeter range see Table (3.1). Thus they are not suitable for large scale production of nanostructures. Where as, nanoimprint lithography [114] and laser interference lithography are methods that allow for structuring of large areas in a short time. Nanoimprint lithography has been shown to produce feature sizes below 10 nm [115], while laser interference lithography is mainly intended to patterns a few micrometers to a few 100 microns.

Table 3.1: Characteristics of most popular lithographic techniques [116]

Techniques	Minimum feature size	Area	Cost	Time
Deep UV lithography [117]	≅ 50-100 nm	Large	High	Short
Extreme deep UV lithography [118]	≅ 30 nm	Large	High	Short
X-ray lithography	≅ 20 nm	Large	High	Short
Electron beam lithography [113]	<10 nm	Small	High	Long
Soft lithography	≅ 10 nm	Large	Low	Short

3.2.1 Laser Interference Lithography

Laser interference lithography utilizes the wave nature of light to produce an interference pattern on the screen (photoresist here), when two coherent beams interferes. Figure (3.1) shows the Llyod'd mirror configuration utilized to achieve such an interference pattern. Narrow beam from UV-laser (He-Cd laser, output power 4 mW, model IK 3031 R-C, Kimmon, Japan) operating at λ = 325 nm is focused by a 40x microscope objective lens (LMU-40X-NUV, Thorlabs) to a pin hole with diameter d = 10 μm. Combination of microscope objective lens and the pinhole works as a spatial filter to improve the homogeneity of the beam. A lens with focal length f = 100 cm is placed at a distance of 1 m from the pinhole to collimate the divergent beam. This combination of microscope objective lens, pinhole and lens works as a beam expander for the setup. Beam expander allows increasing the beam diameter thereby making it possible to radiate large areas with homogeneous intensity. The expanded beam is incident on a sample holder consisting of a rectangular dielectric mirror (RM-50.0-30.00-12.7-UV, CVI Melles Griot) and a space to fix the sample. The dielectric mirror and the sample are orthogonal to each other. The sample holder can be rotated by an angle θ to suite the need of period of nanostructures. Intensity of the interference pattern on the sample comprises of the expanded incident beam directly hitting the sample and a fraction of the beam which is reflected by the dielectric mirror.

Intensity distribution is a critical factor for fabricating uniform periodic patterns especially on large area, where it is a function of the wave amplitude of the interfering beams, the wavelength of the light source, and the LIL angle. For a two-beam interference pattern, intensity is given

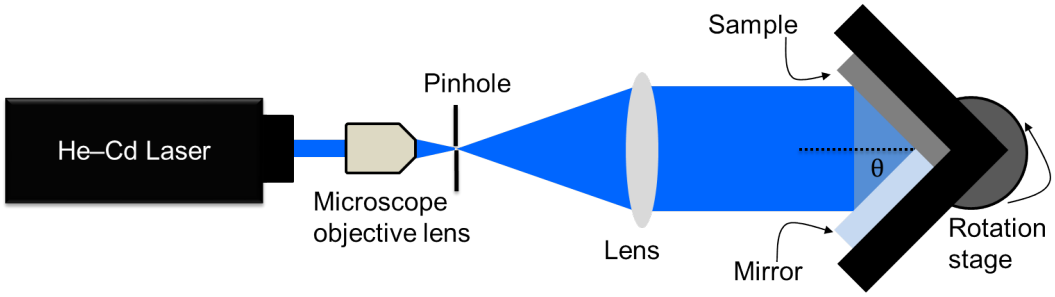

Figure 3.1: Schematics of the Llyod's mirror configuration employed for laser interference lithography.

by:

$$I(x) = 2A\left\{cos\left(\frac{4\pi}{\lambda} \times \sin(\theta)\right) + 1\right\} \tag{3.1}$$

where A is the wave amplitude of the partial beams, λ is the wavelength, and θ is the LIL angle. The intensity is oscillating with the cosine in x-direction. The period (also known as pitch) of this oscillation can be derived as:

$$\Lambda = \frac{\lambda}{2\sin(\theta)} \tag{3.2}$$

LIL has the following advantages compared with other nanolithography technologies: (1) low cost; (2) very high throughput; (3) no contamination on the surface; (4) capability to fabricate patterns large areas (up to hundreds of mm in diameter); (5) re-configurable patterns (with different periods, feature sizes and pattern shapes) [119]. In general, an N-dimensional periodic structures ($N \leq 3$) can be obtained by interfering $(N+1)$ non-coplanar beams within the photoresist. The fringe contrast (or intensity modulation) of the pattern is defined as:

$$V = \frac{I_{max} - I_{min}}{I_{max} + I_{min}} \tag{3.3}$$

where I_{max} and I_{min} are the maximum and minimum intensities in the interference pattern, respectively. An ideal fringe modulation corresponds to the case where $I_{min} = 0$. This will occur when the intensity and polarization of each beam are identical, and the two beams interfere at the photoresist symmetrically at an angle [120].

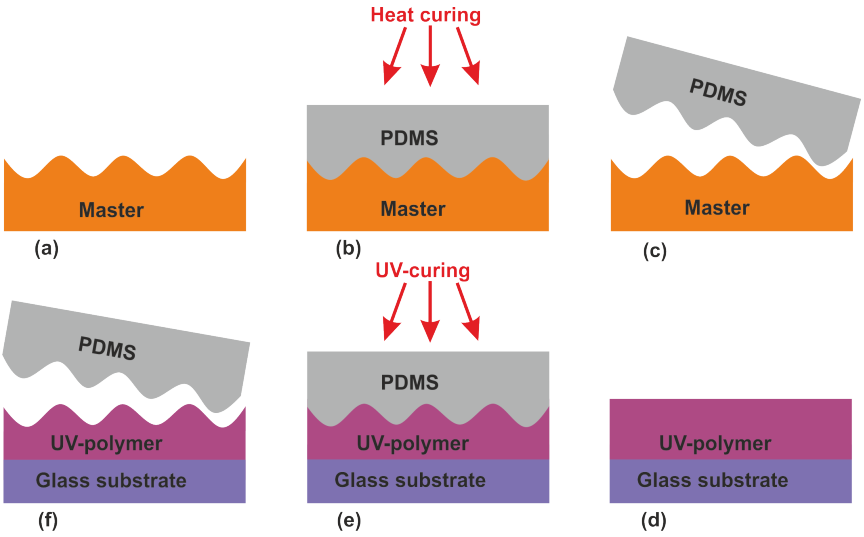

Figure 3.2: Schematics of the nano-imprinting process. a) master is used to prepare the b) PDMS stamp by heat curing it at $T = 50°C$ which has the opposite features than that of master. c) Stamp is released from the master carefully. d) Photoresist is spread over substrate and e) PDMS stamp is brought in contact with resist which is UV-cured and then e) detached to give a structured surface with features similar to the master.

3.2.2 Nano-Imprint Lithography

Nano-imprint lithography is fundamentally different from other conventional lithographies in principle. NIL creates a relief pattern on resist by deforming the resist shape physically using embossing of an existing nanostructure (master), rather than modifying the resist's chemical structure with radiation or self-assembly as is done in LIL and colloidal lithography, respectively. This difference in principles makes NIL capable of producing sub-10 nm features over a large area with a high throughput and low cost [115]. One can distinguish between two kinds of NIL which differ in the way to cure the resist. The first is thermal NIL; where the resist is heat cured, and the second is UV-NIL; where the resist is a UV-crosslinkable photoresist, that is cured by UV-light. Feature sizes are limited by the size of the master from which the structure is replicated.

Methods used in NIL can broadly be categorized into two steps: imprint and pattern transfer. In the imprint, a mould of Polydimethylsiloxane (PDMS) is created by casting liquid PDMS over a master containing the structure to be reproduced. The PDMS is then heat cured at $T = 50°C$ overnight or at room temperature for 2 days. After releasing the PDMS from the master it can be used for imprinting a substrate. For the pattern transfer, PDMS stamp is

brought into contact with the substrate with spin coated UV-photoresist on top. Weight of the stamp itself is enough to make a conformal contact. The substrate with photoresist and stamp on top is then put inside a UV-lamp for crosslinking. Afterwards the PDMS working stamp can be easily detached from the substrate. Step-by-step process for imprinting can be seen in Figure (3.2).

Since imprint lithography is not based on modification of resist chemical structure by radiation, its resolution is immune to many factors that limits the resolution of conventional lithography, such as wave diffraction, scattering and interference in a resist, back-scattering from a substrate, and the chemistry of resist and developer.

3.2.3 Prism-Coupled SPR Spectroscopy

A custom-built surface plasmon resonance (SPR) setup in the Kretschmann configuration was developed in-house and was used for optical SPR studies. As shown in Figure (3.3), an attenuated total reflection (ATR) method was used for the excitation of prism-coupled SPs on the sensor surface. Laser beam (He-Ne, Uniphase, 5 mW, λ = 632.8 nm) passes through a chopper (frequency = 1432 Hz) that is connected to a lockin amplifier (EG & G, Model 7260). The modulated beam then passes through a polarizer, through which intensity and plane of polarization of the laser beam can be changed. A sample chip was optically matched to the prism base by index matching immersion oil (refractive index n = 1.700, Cargille Laboratories Inc, USA). The beam is then reflected off the base of the coupling prism (Schott, LASFN9, n_{p} = 1.85 @ λ = 632.8nm) for an angle of incidence θ, and is collected by a photo-detector connected to lock-in amplifier with integration time of 300 millisecond. The whole assembly of prism/sample and the photo-detector are mounted on two co-axial goniometers with an angular resolution of 0.001° (Huber GmbH, Germany) enabling an independent tuning of respective angular positions.

3.2.4 Angular Wavelength Spectroscopy

An optical setup utilizing ATR method with the Kretschmann configuration has been used to measure angular-wavelength $\lambda(\theta)$ reflectivity spectra. With this custom-built setup as seen in

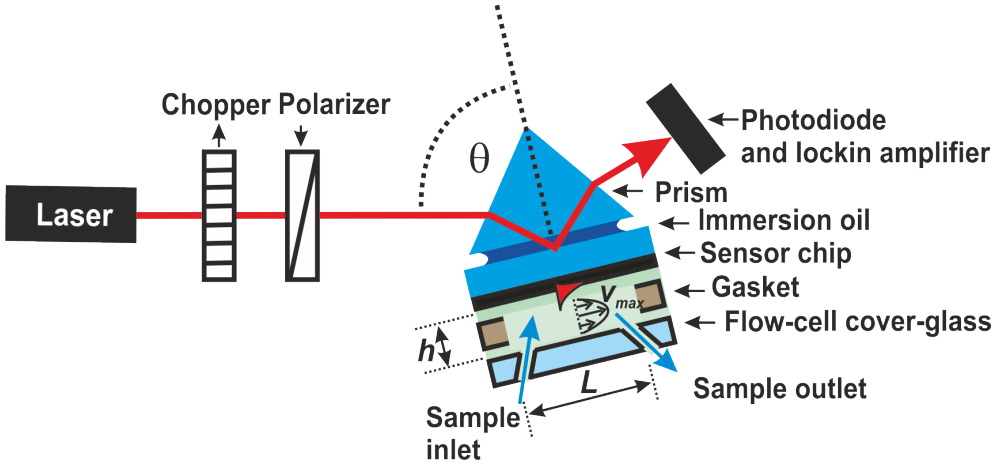

Figure 3.3: Schematics of the setup used for measuring SPR.

Figure (3.4), a wavelength range of 400 – 1000 nm and angles between 0.6° – 90° can be covered. The optical system used for the reflectivity measurement consisted of a white light source (halogen lamp LSH102, LOT-Oriel, Germany) that was connected to an optical fibre (M25L02, Thorlabs, USA). The light emitted from the optical fiber output end was collimated by an achromatic lens (f = 6 cm, 14 KLA 001, CVI Melles Griot, Germany) [121]. This collimated white light beam after passing through a polarizer was coupled to a LASFN9 glass prism and reflected from the base of prism for an angle of incidence θ. A sample chip was optically matched to the prism base by using index matching immersion oil. The complete setup was mounted on a two stepper motor system with resolution of coupling angle $\theta = 0.005°$ (Huber GmbH, Germany). One motor controls the incident angle θ of the incident beam to the sample, while the second motor controls the position of the detection optics at angle 2θ. The reflected light was coupled via a lens (F810SMA-635, Thorlabs, USA) into a multimode optical fibre (M26L02, Thorlabs, USA) that was connected to a high-resolution spectrometer (HR4000, Ocean Optics, USA).

An in-house developed system was used for the reflectivity measurement. Using this software [121], typically from an angle of 45° to 62° with an angular step size of 0.1°, requires three steps:

1. Background : Measuring the background spectrum by blocking the incident light. This background will be subtracted from all the subsequent measurements.

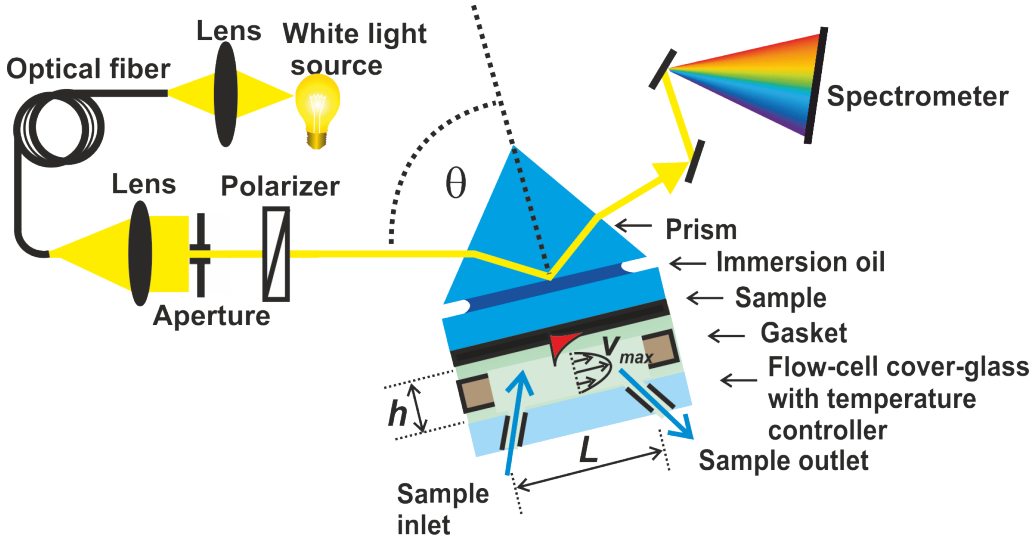

Figure 3.4: Schematics of the angular wavelength measurement setup.

2. Reference : The unique spectrum of white light source would overlap with all measurements which are performed. To overcome this, a reference spectra on the sample needs to be measured. In this work, the reflectivity spectra measured for TM polarisation of incident beam are normalised with that measured for TE polarisation.

3. Signal : The last step is to record the spectra of the reflected light of the investigated region.

The reflectivity spectra normalized to the reference spot is then achieved by the intensities of the three measurements by:

$$R = \frac{I_{\text{sample}} - I_{\text{background}}}{I_{\text{reference}} - I_{\text{background}}} \tag{3.4}$$

The reflectivity R was measured for transverse magnetic polarized incident beam (TM) and normalized with that measured for transverse electric polarization (TE).

3.2.5 Transmission Spectroscopy

Transmission spectroscopy is the oldest and most basic technique for analysing samples. Light from a source passes through a sample to be registered by a detector. The method of analysis is based upon the absorption of the light beam by a sample at specific wavelengths

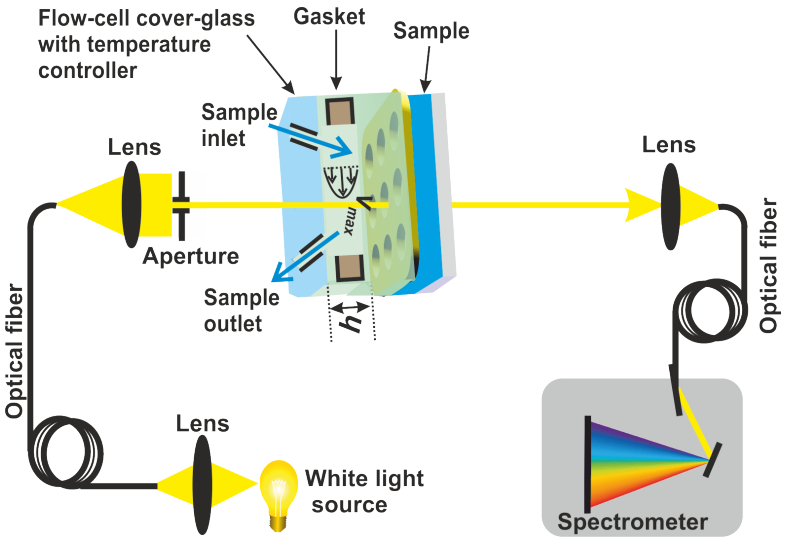

Figure 3.5: Schematics of the nanoimprinting process.

or frequencies of light. The resulting spectrum carries the signature of path length or sample thickness, the absorption coefficient of the sample, the reflectivity of the sample, angle of incidence, the polarization of the incident radiation, and, for particulate matter, on particle size and orientation.

An in-house developed system used for the transmission measurement consisted of a white light source (halogen lamp LSH102, LOT-Oriel, Germany) that was connected to a multimode optical fibre (M26L02, Thorlabs, USA). The light emitted from the optical fiber output end was collimated by an achromatic lens (f = 6 cm, 14 KLA 001, CVI Melles Griot, Germany). This collimated white light beam was allowed to pass through the sample arrangement. A sample chip was fixed to the base plate having space to hold sample as seen in Figure (3.5). This whole assembly was arranged on a movable rail which allows bringing the reason of investigation into path of light. The transmitted light was coupled via a lens (F810SMA-635, Thorlabs, USA) into a multimode optical fibre (M26L02, Thorlabs, USA) that was connected to a high-resolution spectrometer (SR-303i-B, Andor, USA). A temperature controlled flow cell was attached to the top surface of sample chip and measurements were performed as described in section (3.4).

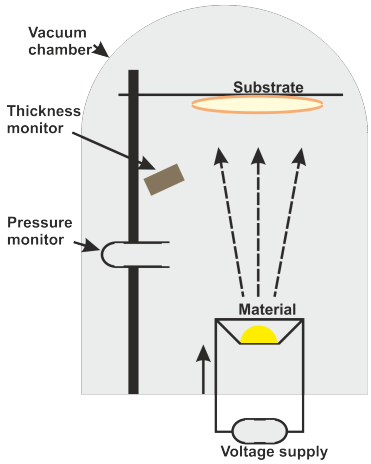

Figure 3.6: Schematics of the vacuum chamber used for thermal vapor deposition.

3.3 Metallic Gold Deposition

Evaporation is a common method for thin-film deposition. The source material is fed onto Molybdenum dimple boat (HHV Ltd, UK) and evaporated in a vacuum, i.e. vapors other than the source material are almost entirely removed before the process begins. In high vacuum (with a long mean free path), evaporated particles can travel directly to the deposition target (cleaned glass substrate) without colliding with the background gas, where they condense back to the solid state. Purity of the deposited film depends on the quality of the vacuum, and on the purity of the source material. At a given vacuum pressure the film purity will be higher at higher deposition rates as this minimizes the relative rate of gaseous impurity inclusion [122]. As seen in Figure (3.6), thickness of metal film deposited is monitored by a quartz crystal.

Glass substrate (BK7 or LaSFN9) were cleaned by sonication in 1% Hellmanx solution, followed by water and ethanol for 15 min. each and dried with air gun. Cleaned substrates were put inside the thermal evaporator (Model HHV FL400, HHV Ltd, UK) and a thin film of gold layer was prepared.

3.3.1 Surface Functionalization

Gold surface was chemically modified to support the adhesion of hydrogel layer on top of it.

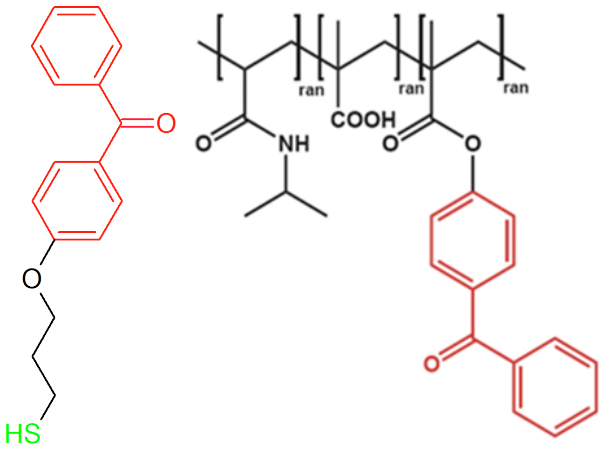

(a) (b)

Figure 3.7: (a) Chemical structure of benzophenone-thiol and (b) chemical structure of poly (N-isopropylacrylamide-co-methacrylic acid-co-4-methacryloyloxy benzophenone) (pNIPAAm)

Self-Assembled Mono-layer

Self-assembled mono-layer (SAM) are organic assemblies formed by the adsorption of molecular constituents from solution onto the surface of solids. The molecules that form SAMs have three different parts: *terminal*, *backbone* and *head* group. Head group has a specific affinity for a surface. There are a number of headgroups that bind to specific metals, metal oxides, and semiconductors. The thickness of a SAM is typically 1-3 nm; they are the most elementary form of a nanometer-scale organic thin-film material [123].

In this study, (3-thiopropyl)oxybenzophenone (BP-thiol) was used for adhesion promoting. As the Figure (3.7a) shows the chemical structure of the BP-thiol molecules used in this study, *terminal* group is benzophenone, canbon chain is the *backbone* and thiol is the *head-group*. Typically, the SAM was prepared by immersing fresh prepared Au substrates in a mixed benzophenone thiol solution at 1 mM total concentration in ethanol for at least 24 h. The substrates modified with SAM were then rinsed with ethanol and dried with air and stored in nitrogen filled environment.

3.3.2 Hydrogel Thin Layer

In this study, pNIPAAm based polymer composed of N-isopropylacrylamide, methacrylic acid, and 4-methacryloyloxy benzophenone in a ratio of 94:5:1, respectively, was used to prepare thin film of hydrogel (see Figure (3.7b)). The polymer was synthesized [99] to carry two functional groups: i) the benzophenone groups which offers the photo-crosslinking capability and, ii) the carboxylic groups which serve the chemical immobilizations of ligands. During the UV-crosslinking of hydrogel, oxygen radical is formed in the benzophenone group which is highly reactive. This oxygen radical attack the carbon chain and thus crosslinking occurs, see Figure (3.8a) to follow the sequence of steps leading to crosslinking of polymers. The amount of crosslinking or crosslinking density depends upon the irradiation dose of the UV-lamp. Higher the dose, higher the crosslinking density. In a hydrogel, this dose dependent is directly related to the swelling ratio of hydrogel, which is defined as the ratio of thickness in swollen state to the thickness in dry state. It is express as:

$$\mathrm{SR} = \frac{d_h}{d_{h-dry}} \tag{3.5}$$

Highly crossliniked hydrogel will have less access for swelling and thus will have less swelling ratio. Figure (3.8b) shows the decrease in swelling ratio from *ca.* 10 to 5 as the irradiation dose increases from 5 to 25 Jcm^{-2}. This pNIPAAm based hydrogel is temperature sensitivea and have its lower critical solution temperature (LCST) around $32°C$. As seen in Figure (3.8c) increasing the temperature beyond the LCST will cause the hydrogel to collapse and in effect swelling ratio will decrease and refractive index (n_{h}) will approach the dry state value ($n_{\mathrm{h-dry}}$). Hydrogel thickness was adjusted by changing the concentration of pNIPAAm solution with ethanol, as seen in Figure (3.8d).

To prepare the substrate with thin layer of hydrogel, two methods were employed to modify the gold surface:

1. SAM of BP-thiol : A gold coated glass substrate was immersed into a thiol-benzophenone solution with ethanol at the concentration of 1 mM overnight to form a functionalized thiol mono-layer on gold surface. After rinsing with ethanol and drying in air stream,

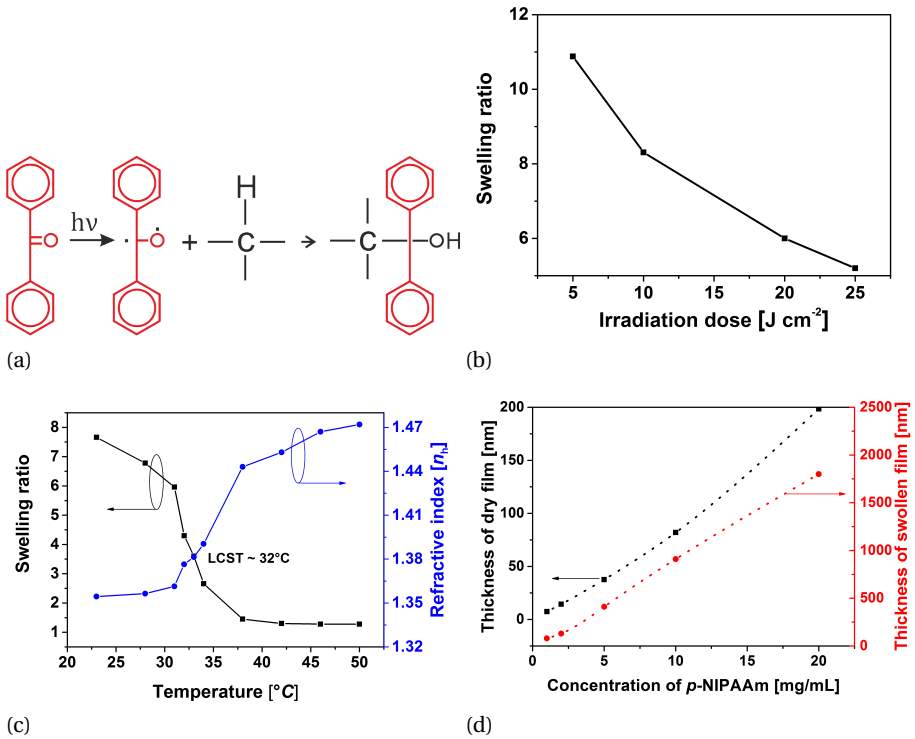

Figure 3.8: (a) Chemical reaction occurring during the UV-crosslinking of hydrogel, (b) variation of swelling ratio of hydrogel with the change in irradiation dose of UV-lamp for 4% wt. of pNIPAAm from $5-25\,\mathrm{Jcm^{-2}}$, (c) variation of swelling ratio and refractive index with the change in temperature for 4% wt. of pNIPAAm from $23-50°\mathrm{C}$ and (d) variation in thickness of hydrogel in dry state and in swollen state for a change in concentration $c_h = 0.125-2\,\%$ wt. for a irradiation dose of 2 $\mathrm{Jcm^{-2}}$.

the pNIPAAm polymer solution with ethanol is spin-coated on the substrates.

2. SU-8 layer : On top of the gold surface, a SU-8 polymer film with a thickness of about 10 nm was spin-coated from $c = 4.8\,\mathrm{vol}\,\%$ solution (dissolved by SU-8 thinner) at spin rate 6000 rpm. After the spin-coating of SU-8, substrates were dried in a vacuum oven at $50°C$ for 2 hours and after this pNIPAAm polymer solution with ethanol is spin-coated on the substrates.

Hydrogel layer were spin-coated (G3P-8, SCG) with 2000 rpm for 2 minutes, and dried at $50°C$ in a vacuum oven (VT6025, Thermo scientific) overnight then crosslinked by using a lamp (Bio-Link 365, Vilber, Germany) with ($\lambda = 365\,\mathrm{nm}$) with a irradiation dose of 25 $\mathrm{Jcm^{-2}}$. The density and thickness of the hydrogel layer were controlled by the rate of spin-coating, the concentration of polymer used in spin-coating and UV-light irradiation dose.

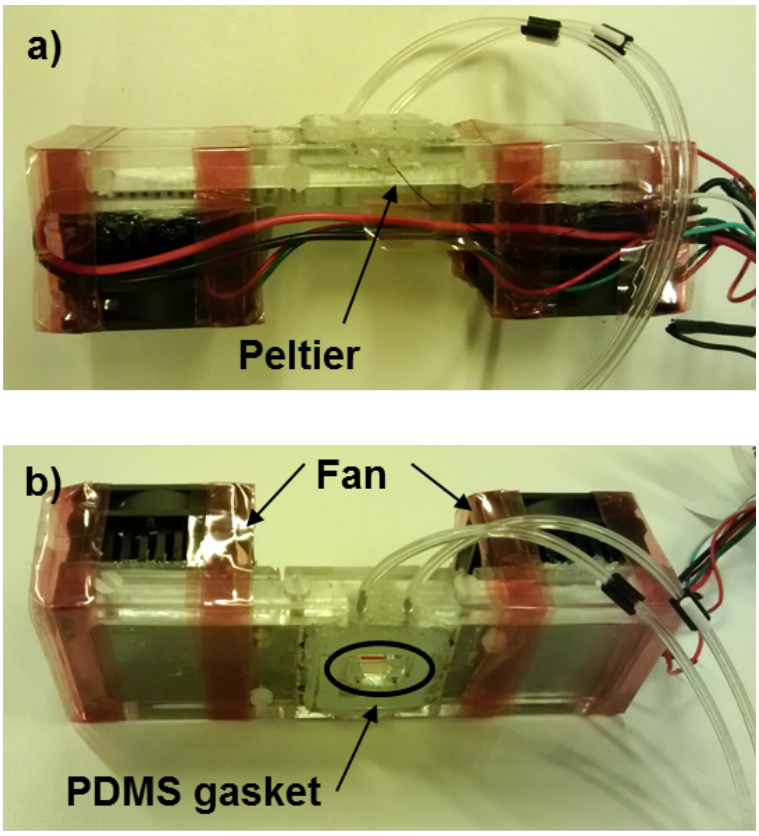

Figure 3.9: a) Side view of custom made temperature controlled flow-cell showing the Peltier element along with electronics attached into it and b) shows the two mini-fans mounted on the metal slab and at the center of it lays the gasket region where the buffer flows.

3.4 Temperature Controller

As seen in Figure (3.9), an in-house designed flow cell with temperature-stabilization at a background temperature T_0 by a Peltier device connected to its driver (LFI3751, Wavelength Electronics, USA) was attached to the sample chip and water was pumped by using a peristaltic pump with a tubing (ID 0.76, SC0008, IDEX Health & Science SA, Switzerland). Two mini fans were mounted on flow cell to prevent it from overheating. Fans were controlled by electronics from VOLTCRAFT (VLP-1303 PRO, Conrad Electronics SE, Germany). Temperature was changed from T_0 (generally room temperature) upto 50 ° C in a series of steps. The data acquisition and system control was performed by an in-house developed software tool developed in LabVIEW (National Instruments, USA) [121].

4 Responsive Hydrogel Nanostructures Studied by Waveguide-enhanced diffraction

4.1 Introduction

Microstructuring of hydrogel has been focus of interest for many applications, including drug delivery [73–76, 78, 79], dry adhesives that mimic gecko foot fibrillars [124, 125], adaptive microlenses [126], photonics crystals [127, 128] and label-free contact lens biosensors [129]. Thin hydrogel films were structured by using modern fabrication techniques, including e-beam lithography [130], nano-imprint lithography (NIL) [131, 132], laser interference lithography (LIL) [133] and colloidal lithography [134]. Among these, NIL is widely used methods because of its low cost, high throughput and high resolution. Replica molding [131] from poly(dimethylsiloxane) PDMS has been applied to pattern hydrogels from polyerms [135]. Amongst the responsive polymers, poly(N-isopropylacrylamide) (pNIPAAm)-based polymer holds a prominent stage due to its strong swelling and collapsing by variations of temperature around its lower critical solution temperature (LCST) ~ 32°C. Subsequently pNIPAAm have been used in the form of 2D films [89], composites [79] showing their great potential in biomedical fields. Surface plasmon enhanced diffraction measurement was shown to be an important technique to investigate the periodically patterned hydrogel films. The reversible swelling and collapsing of the structured hydrogel triggered by an external stimulus could be greatly enhanced the diffraction efficiency by using SP as the diffracted electromagnetic wave [112].

This work presents a new technique to observe the responsive hydrogel nanostructures based on waveguide mode-enhanced diffraction measurement. NIL is used to imprint thermo-

responsive photo-crosslinkable pNIPAAm – based hydrogel over large area with arrays of high aspect ratio nanopillars. 3D swelling and collapsing of nanopillars is observed *in situ* optically and by atomic force microscopy measurements. it is being compared to the 1D swelling of a film from identical pNIPAAm hydrogel.

4.2 Materials and Method

4.2.1 Polymer Synthesis

A random pNIPAAm-based terpolymer (composed of *N*-isopropylacrylamide, methacrylic acid, and 4-methacryloyloxy benzophenone at a ratio of 94 : 5 : 1, respectively is depicted in Figure (4.1)a) was synthesized by free radical polymerization as described elsewhere [99]. The N-isopropylacrylamide provided the thermo-responsive characteristics of the terpolymer, the benzophenone moieties enabled its photo-crosslinking, and the MAA allowed the post-synthetic modification [92] and it improved the swelling properties.

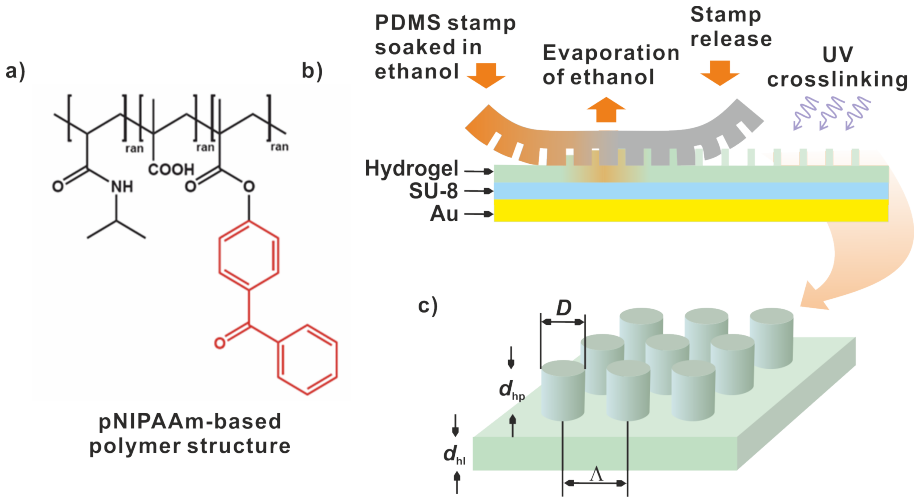

Figure 4.1: a) Chemical structure of poly (*N*-isopropylacrylamide-co-methacrylic acid-co-4-methacryloyloxy benzophenone) (pNIPAAm)-based photo-crosslinkable polymer, b) schematics of the methods employed to prepare arrays of hydrogel nanopillar by nanoimprint lithography, and c) geometry of the final imprinted nanopillar arrays on hydrogel.

4.2.2 Working Stamp Preparation

Arrays of nanoholes on a Si wafer were fabricated by e-beam lithography at Temicon GmbH (Germany). The SEM observation was used to determine the diameter of nanoholes of D=90 nm, their depth was d_{hp}=260 nm, and the array period of Λ=460 nm. The structured area of 1 cm^2 was transferred to a PDMS working stamp in two following steps. In the first step, an Ormostamp polymer from Micro Resist Technology GmbH (Germany) was dispensed on the Si master and contacted with a glass substrate that was previously coated with adhesion promoting OrmoPrime08 from Micro Resist Technology GmbH (Germany). The Ormostamp polymer was crosslinked by UV light (irradiation dose 1 J cm^{-2} at a wavelength of λ = 365 nm), detached from the Si master, and a final thermal treatment at 130 °C for 30 minutes was applied. The Ormostamp copy with inverse structure (arrays of nanopillars) was modified with an anti-sticking layer by vapor-deposition of 1H,1H,2H,2H perfluorooctyl-trichlorsilane from Sigma Aldrich in an desiccator at 250 °C. In the second step, PDMS working stamp was prepared from Sylgard 184 from Dow Corning (USA) that was mixed at ratio of 1:10 with its curing agent and poured over the Ormostamp. After curing the PDMS elastomer at 60 °C, it was detached from the Ormostamp copy forming about 3 mm thick PDMS working stamp with arrays of nanoholes at its bottom surface.

4.2.3 Preparation of Arrays of Hydrogel Nano-pillars

pNIPAAm hydrogel film was prepared on high-refractive index LaSFN9 glass substrate that was subsequently coated with 2 nm Cr and 47 nm Au film by vacuum thermal evaporation (FL400, HHV Ltd, UK). In order to promote adhesion of pNIPAAm layer to the Au surface, a thin SU-8 film was spun on its top. SU-8 from Micro Resist Technology GmbH (Germany) was diluted with SU-8 thinner at ratio of 1:50 and spun at 500 rpm for 1 second followed by 5000 rpm for 60 seconds. Then, the substrates were dried in a vacuum oven for 2 h at 50°C. Afterward, pNIPAAm layer was prepared on the top of SU-8 linker. A 6 %wt pNIPAAm polymer solution in ethanol was spun at 2000 rpm for 2 minutes and dried overnight at 50 °C in a vacuum oven. The thickness of a dry pNIPAAm film of $d_{hl-s} \sim 300$ nm and the thickness of SU-8 linker layer of ~ 10 nm were measured by surface plasmon resonance (SPR).

The imprinting of pNIPAAm polymer layer with arrays of nanopillars by using the PDMS working stamp is illustrated in Figure (4.1)b). Firstly the permeable PDMS working stamp was soaked in ethanol for several minutes. Then, the working stamp was removed, its surface was quickly dried with a stream of air, and it was allowed to form a conformal contact with the pNIPAAm film. After the placing of PDMS working stamp onto the pNIPAAm layer, additional $10\,\mu L$ of ethanol was dispersed on its top. The ethanol diffused from PDMS to the surface and partially dissolved the pNIPAAm polymer so its upper part become fluid and filled the PDMS nanoholes. The PDMS working stamp soaked with ethanol was kept in contact with pNIPAAm at room temperature for 1 hour and then it was dried overnight in vacuum at room temperature. Afterwards, the PDMS working stamp was released leaving the imprinted arrays of pNIPAAm nanopillars. The imprinted pNIPAAm surface was dried kept in vacuum oven at 50 °C for several hours and subsequently cross-linked with UV light at wavelength $\lambda = 365\,\text{nm}$ and irradiation dose of 10 $\text{J}\,\text{cm}^{-2}$ by using a UV lamp Bio-Link 365, Vilber (Germany). Further, the geometry of pNIPAAm imprinted surface is described by the period Λ, diameter of cylindrical pillars D and height d_{hp}.

4.2.4 Imaging of Nanopillars by AFM

Ex situ observation of imprinted pNIPAAm surface was performed in air at room temperature by atomic force microscope (AFM) from PicoPlus from Molecular Imaging (USA) in tapping mode. The used n^+-silicon cantilever (PPP-NCHR) was purchased from NANOSENSORS™(Switzerland).

For the *in situ* measurements, investigated substrate with nanostructured pNIPAAm surface was placed in a flow-cell that contains water and allows to control temperature in the range $T = 15 - 60\,°\text{C}$. The surface with swollen and collapsed nanopillars was observed in situ by silicon-nitride probes (DNP-S10, Bruker, USA) with a nominal spring constant of 0.24 N/m. Prior to its use in the AFM, the cantilever was cleaned with UV/Ozone for 20 minutes. AFM images (AFM Nanowizard II, JPK Instruments, Germany) were obtained in tapping mode, at low forces to prevent sample damage, at a scan rate lower than 2 Hz.

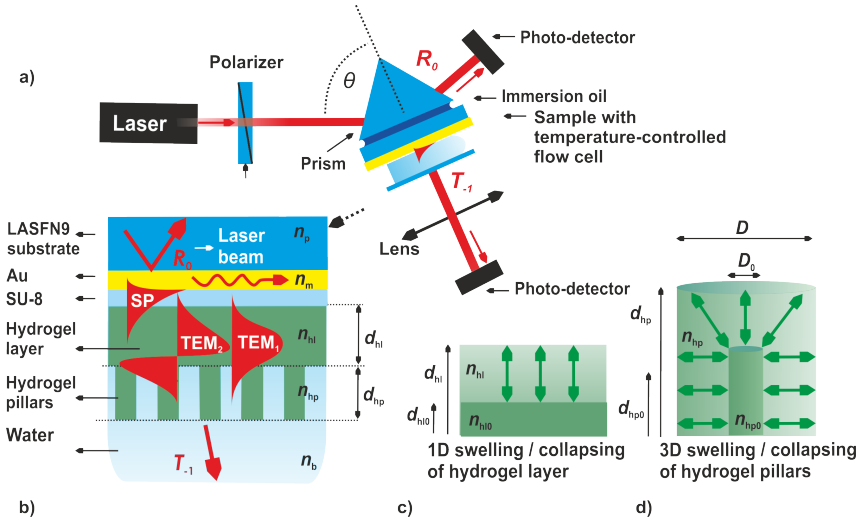

Figure 4.2: a) Optical system for probing the swelling and collapsing of hydrogel films and nanopillars arrays by optical waveguide spectroscopy and diffraction, b) schematics of the layer architecture showing hydrogel layer and hydrogel pillars, c) one dimensional swelling and collapsing of hydrogel layer, and d) three dimensional swelling and collapsing of hydrogel nanopillars.

4.2.5 Optical Setup

An optical setup utilizing attenuated total reflection (ATR) with Kretschmann configuration was used for the excitation of surface plasmons and optical waveguide modes that probes the nanostructured hydrogel film. The system is showed in Figure (4.2) and it utilizes a laser beam emitted from He-Ne laser (Uniphase, 5 mW) at wavelength $\lambda = 632.8\,\text{nm}$ that propagates through a chopper and polarizer and is coupled to a 90° prism made of LaSFN9 glass. To the prism base a glass substrate with Au layer and nanostructured pNIPAAm layer is optically matched by immersion oil from Cargille Laboratories Inc. (USA). Against the polymer surface, a flow cell is pressed in order to flow aqueous samples over the nanostructured hydrogel surface. The flow cell was made from a PDMS gasket and was sealed by transparent glass substrate. Temperature of water that was flowed over the surface by using a peristaltic pump from IDEX Health & Science SA (Switzerland) was controlled in the range between T=22 and 50 °C by a Peltier device connected to a respective driver LFI3751 from Wavelength Electronics (USA). More details on this system can be found in section (3.4).

The whole assembly of prism, glass substrate and flow cell was mounted on two co-axial goniometer with an angular resolution of 0.001° (Huber GmbH, Germany) for the control of the angle of incidence θ. Upon the incidence of the laser beam, its intensity is partially reflected

and partially scattered to series of diffraction orders on the periodic arrays of hydrogel pillars. The intensity of reflected light beam R_0 was detected by a photodiode that is connected to lock-in amplifier EG & G 7260. The intensity of -1^{st} order diffracted beam T_{-1} that propagates through the flow-cell was measured by an identical detector. These intensities were normalized with that of the incident beam and were measured as the function of angle of incidence θ. Let us note that this angle describes the propagation of the beam in air before is coupled to the prism and is refracted at its surface. The data acquisition and system control was performed an in-house developed software tool developed in LabVIEW (National Instruments, USA) and by the Wasplas software developed at the Max Planck Institute for Polymer Research in Mainz, Germany.

4.2.6 Evaluation of Reflectivity and Diffraction Spectra

Measured angular dependence of reflectivity $R_0(\theta)$ was fitted with a Fresnel-based model implemented in the software Winspall that was developed at Max Planck Institute for Polymer Research in Mainz (Germany). In this analysis, refractive indices of Au, Cr and SU-8 were assumed to be $0.2 + 3.51\,i$, $3.14 + 3.3\,i$ and 1.48, respectively. The respective thicknesses of these layers were determined by fitting reflectivity spectra $R_0(\theta)$ measured on a reference sample prior to the coating with pNIPAAm. For the investigation of 1D swelling of pNIPAAm hydrogel film, a "box model" was used as prepared films were assumed to be homogeneous perpendicular to the surface and described by its thickness d_{hl} and refractive index n_{hl}. The linear swelling ratio of the pNIPAAm hydrogel film was defined from determined thickness in water and after drying as $SR_{1D} = d_{hl}/d_{hl0}$. In order to capture the changes in the geometry of nanopillars from the variations in T_{-1} spectrum, a numerical model based on finite element method (FEM) was implemented in a diffraction grating solver DiPoG (Weierstrass Institute, Germany). The refractive index of LaSFN9 was assumed as $n_p = 1.845$ and that of water as $n_s = 1.33$. Refractive index of gold was assumed to be dispersive $n_m(\theta)$ and it was taken from Palik [136]. Refractive index of SU-8 was set to 1.48 and the presence of chromium was omitted. The attached pNIPAAm hydrogel refractive index was $n_h = 1.356$ in swollen state and $n_h = 1.47$ in collapsed state.

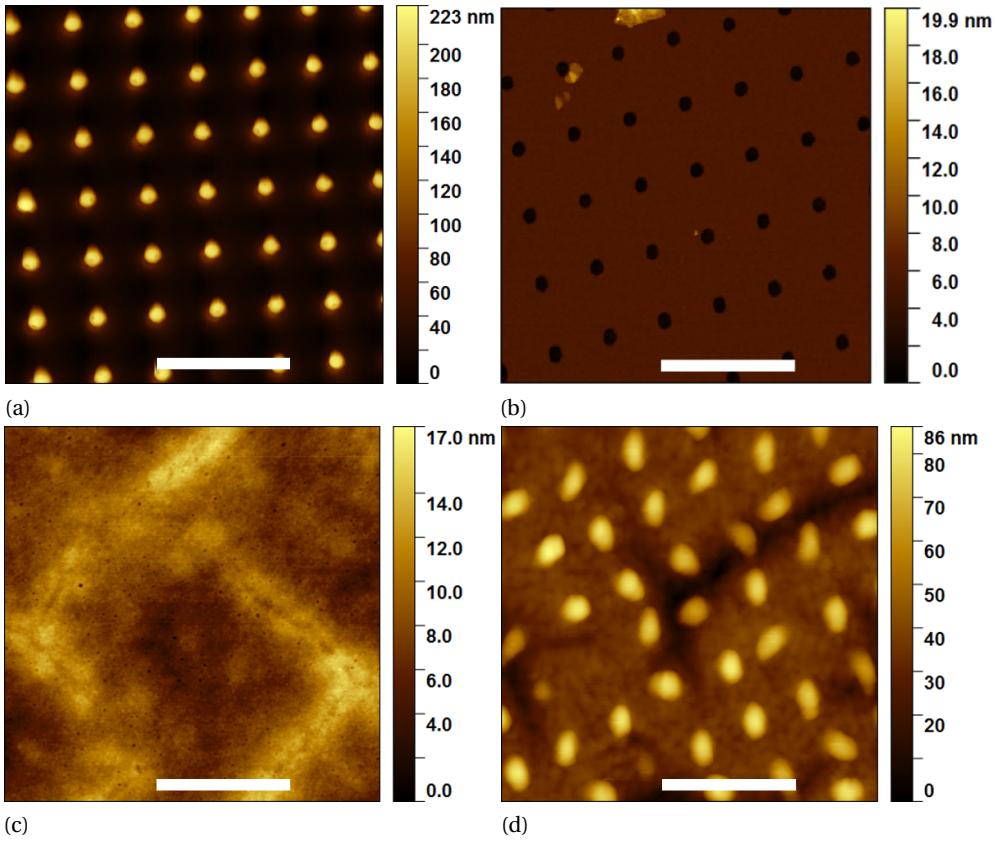

Figure 4.3: (a) *Ex situ* AFM observation in a) air of a freshly prepared hydrogel nanopillars arrays compared to b) Si master with nanohole arrays. The observation of structured hydrogel surface that was swollen in water and dried at at temperature c) below LCST at $T = 22\,°C$ and d) above LCST at $T = 38\,°C$. Scale bar shows the length $1\,\mu m$.

4.3 Results and Discussion

4.3.1 *Ex situ* AFM

The arrays of imprinted pNIPAAm hydrogel nanopillars that is presented in Figure (4.3) were first observed *ex situ* in air by AFM. It reveals that the freshly prepared pNIPAAm nanopillar arrays exhibited identical period of $\Lambda = 460\,nm$, but their height $d_{hp} \sim 208\,nm$ and diameter of about $D \sim 143\,nm$ (measured at 40 % of maximum height). The height of the pillars was about 25 % lower and diameter was 50 % wider compared to the original Si structure. This can be attributed to the deviations in the multi-step replication process. The image of pNIPAAm arrays are presented in Figure (4.3a) and are compared to the characterization of the arrays on nanoholes on Si master in Figure (4.3b). After the imprinting and crosslinking with UV, the

pNIPAAm nanopillar arrays and the underneath pNIPAAm layer were allowed to swell in water at temperature $T = 22$°C. After drying the pNIPAAm arrays at the same temperature $T = 22$°C, the surface was observed again with AFM. As seen in Figure (4.3c), after swelling the structure in water and drying at room temperature, the surface flattens and the structure disappears.

Interestingly, when the surface is swollen in water again at $T = 22$°C and subsequently dried at higher temperature of $T = 38$ °C that is above pNIPAAm LCSST, the arrays of pillars was partially recovered on the surface as seen in Figure (4.3d). The erasure of the structure probably occurs due to the re-arrangement of swollen polymer chains upon the drying when the surface tension strongly competes with retraction of the polymer network to original shape that was imprinted. This hypothesis was confirmed by the observation of structure recovery when the drying was performed at elevated temperature above the LCST. In this case, the temperature-induced collapse of pNIPAAm network allows re-establishing of pillars in water which was then rigid enough to withstand the subsequent water evaporation. It indicates that collapsing of the pNIPAAm polymer in water at temperature above its LCST leads to the formation of pillars which stays after the solvent evaporation. As can be seen from the comparison of Figure (4.3a) and Figure (4.3d), the shape of the pillars that are freshly imprinted and those that were swelled and dried dramatically changed. The freshly prepared pillars exhibited cylindrical shape with volume of $\pi/4D^2 d_{hp} = (3.35 \pm 0.5) \times 10^{-3}\,\mu\text{m}^3$. After the subsequent swelling, collapsing at temperature $T = 38$ °C, and drying the surface the height of the pillars decreased by a factor of ~ 3 to $d_{hp} = 76$ nm but the pillar diameter increases to a value $D \sim 242$ nm and their volume was estimated as $(3.51 \pm 0.52) \times 10^{-3}\,\mu\text{m}^3$. In addition, the randomly oriented prolonged shape of pillars in the direction parallel to the surface indicates that they bend upon the pNIPAAm collapse.

4.3.2 *In situ* AFM

In order to shed light on the contraction of pNIPAAm network and recovery of imprinted nanopillars, *in situ* AFM measurements were carried out upon gradually increasing temperature of water from $T = 22$ °C to $T = 50$ °C. At low temperatures $T < 30$ °C, the imprinted structure was not detectable by used AFM. As seen in Figure (4.4)a), topology of soft pNIPAAm surface exhibited irregular features that can be attributed to the buckling associated with a

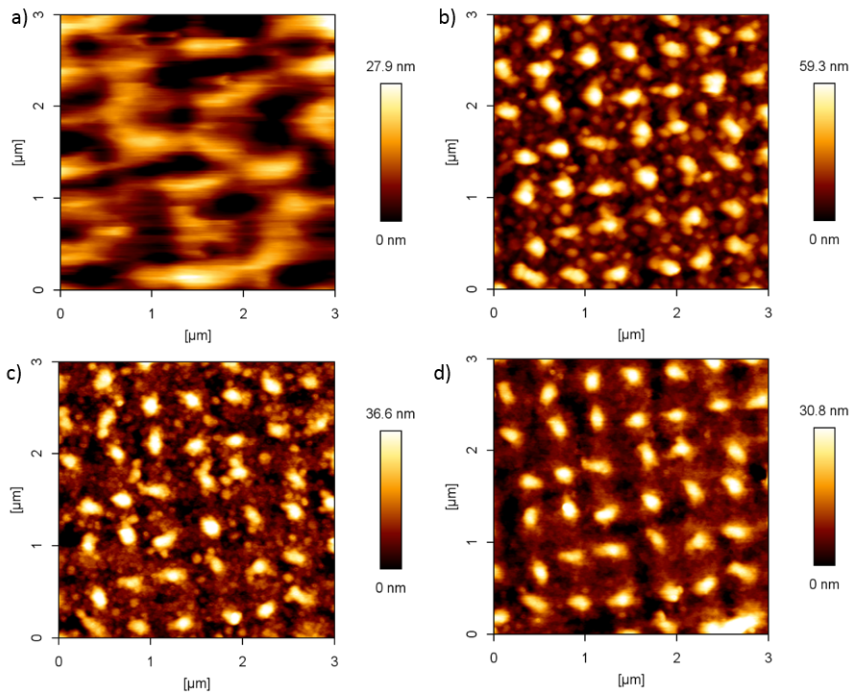

Figure 4.4: In situ AFM observation of swelling of pNIPAAm hydrogel nanopillars in water at temperature a) $T = 22\,°C$, b) $T = 31\,°C$, c) $T = 38\,°C$ and d) $T = 50\,°C$.

stress induced by swelling of residual pNIPAAm layer that is constrained to the direction perpendicular to the surface. Such behavior was observed for other hydrogel films that exhibited thickness of about several tens of μm and a gradient in the cross-linking density perpendicular to the surface [137]. It should be noted that crosslinking density gradient was also observed by OWS for the herein used pNIPAAm-based films with a thickness in swollen state of several μm [138]. When approaching LCST of pNIPAAm, the regular imprinted structure become apparent in acquired AFM images. Figure (4.4)b-d) illustrate that the height and area of periodic imprinted features gradually decreases with the temperature. These features exhibit stronger contrast as the height of irregular features associated with the buckling in between imprinted pillars decreases with increasing temperature as well. The height of contracting pillars of ~ 45 nm was observed at $T = 31\,°C$ and it shrunk to ~ 30 nm at $T = 50\,°C$. In addition, Figure (4.4)d) clearly indicates that the imprinted pillars bend and lay randomly oriented parallel to the surface in water at temperature well above the polymer LCST. This is similar to the observations made in air as seen in Figure (4.3d) which indicates that this effect does not occur due to the surface tension upon the drying and it was probably associated with hydrophobic

interaction. Hydrophobicity of polymer in pillars as well as that of the underneath residual layer gradually increases when increasing the temperature as reported by previous AFM study on similar pNIPAAm-based material [139].

4.3.3 *In situ* Optical Waveguide Spectroscopy

Further, the temperature-induced changes in pNIPAAm nanostructures was investigated optically. The swelling and collapse of residual pNIPAAm layer was observed by OWS that was implemented in the optical system showed in Figure (4.2). As can be seen in Figure (4.5)a) and b), pNIPAAm layer in contact with water was probed by resonantly excited $TE_{0,1}$ and $TM_{1,2}$ modes that manifests itself as series of characteristic dips in the reflectivity spectrum $R_0(\theta)$. The thickness d_{hl} and refractive index n_{hl} of pNIPAAm layer were determined at temperature between $T = 22\,°C$ and $T = 50\,°C$ by fitting the resonant angles at which the modes were excited.

Results summarized in Figure (4.5)c) show that at room temperature $T = 22\,°C$, the pNIPAAm layer swells in the direction perpendicular to the surface and exhibit the thickness of about $d_{hl} = 2280\,nm$ and refractive index of $n_{hl} = 1.356$. When increasing the temperature, the hydrogel layer abruptly collapses at pNIPAAm LCST = 32 °C and at a temperature of $T = 50\,°C$ the thickness drops to $d_{hl} = 380\,nm$ and the refractive index increases to $n_{hl} = 1.47$. The imprinting of the upper surface of pNIPAAm layer weakly affected the spectrum of guided waves in $R_0(\theta)$ and thus the evaluated thickness d_{hl} and refractive index n_{hl} of structured and flat surface were similar. The reason is that the volume of imprinted pillar is only about few percent of that a unit cell of the residual layer ($d_{hl}\Lambda^2 = 6.4 \times 10^{-2}\,\mu m^3$ for the dry state). Therefore, the imprinting only slightly decreased the thickness of residual layer d_{hl}. In addition, effective refractive index of the upper layer with pNPAAm pillars is too thin and low to support additional guided waves. The swelling ratio of the pNIPAAm layer of $SR \sim 6$ at room temperature $T = 22\,°C$ was determined as the ratio of the thicknesses d_{hl} in swollen and dry state. This parameter is inversely proportional to the polymer volume content f_p which can be obtained from effective medium theory as:

$$f_p = \frac{(n_{hl}^2 - n_{hl0}^2)(n_s^2 + 2n_{hl0}^2)}{(n_{hl}^2 + 2n_{hl0}^2)(n_s^2 - n_{hl0}^2)} \tag{4.1}$$

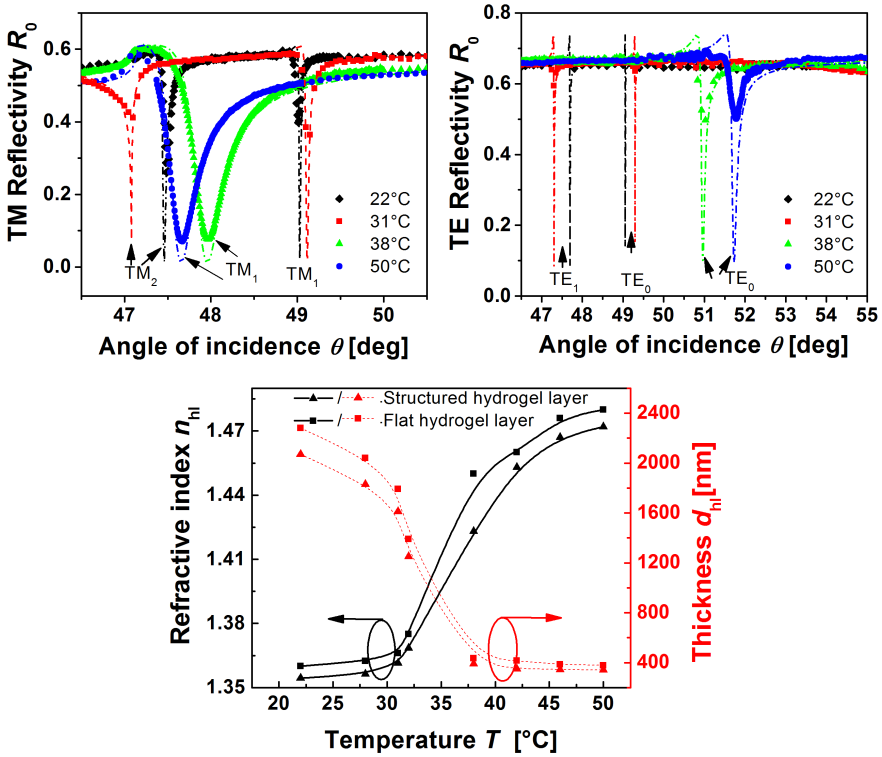

Figure 4.5: Angular reflectivity spectra for a) TM and b) TE polarization of light for structured hydrogel layer with varied temperature (symbols shows the measured data and lines represents the respective fitting) and c) determined refractive index n_{hl} and thickness d_{hl} of hydrogel layer with flat and imprinted surface.

where $n_{hl0} = 1.48$ is the refractive index of (dry) polymer and n_s is the refractive index of water solvent $n_s = 1.332$ at $\lambda = 633\,\text{nm}$ [140]. Based on Equation (4.1), polymer volume content in swollen state at room temperature $T = 22\,°\text{C}$ was determined as $f_p = 0.17$ which is consistent with the swelling ratio calculated from the volume change.

4.3.4 *In situ* Diffraction Efficiency

The optical observation of 3D swelling of pNIPAAm nanopillars was carried out by the measurement of changes in the intensity of diffraction beam T_{-1}. The sample with arrays of pNIPAAm nanopillars was optically matched to the prism in such orientation that one of its axis was in the plane of incidence. The light beam hitting the surface at angles $\theta > 47°$ partially totally internally reflected back into the prism (R_0 signal) and is partially diffracted to -1^{st} diffraction order towards to prism (R_{-1}) and towards the water (T_{-1}). It is worth of mentioning

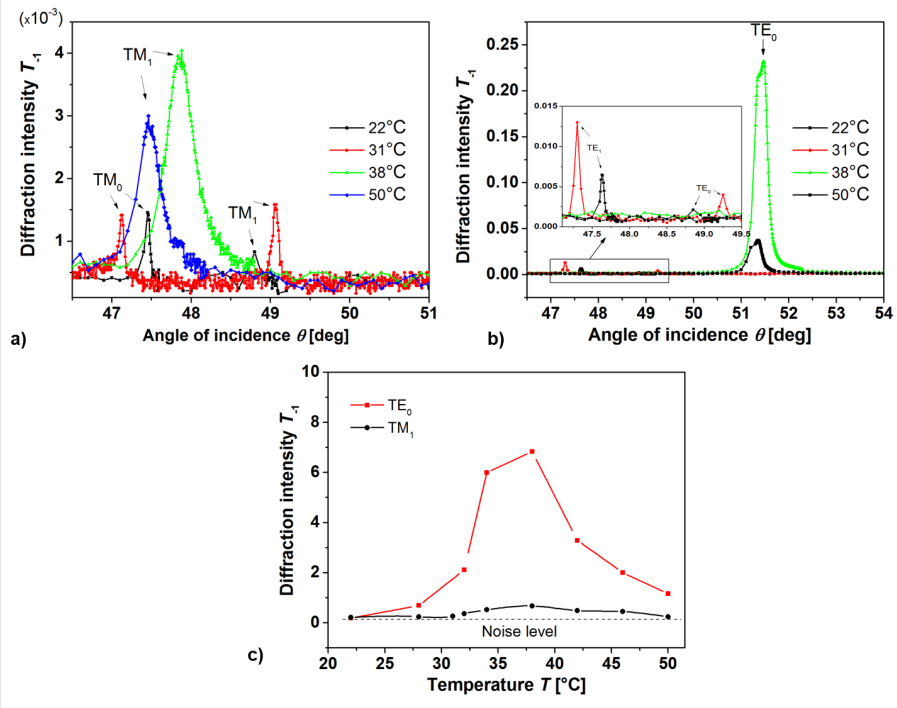

Figure 4.6: Measured angular spectrum of transmitted beam intensity $T_{-1}(\theta)$ for varied temperature and a) TM and b) TE polarization. c) Peak diffraction intensity T_{-1} measured upon the resonant excitation of TE_0 and TM_1 modes. Lines are guide for eyes.

that the -1^{st} diffraction orders travel at angles that are close to zero $\theta = 0$. Unlike the reflected diffraction order R_{-1}, the transmitted beam T_{-1} propagates through the transparent flow-cell and thus its intensity changes can be easily detected with the optical system described in Figure (4.2).

Figure (4.6) shows the angular dependence of T_{-1} intensity for a) TM and b) TE polarized light beam. These spectra were measured at temperatures between $T = 22\,°C$ and $T = 50\,°C$ and they reveal that the overall background (relative) intensity $\sim 5 \times 10^{-5}$ does not change with temperature. However, there occurs a series of peaks above this background at angles where $TE_{0,1}$ and $TM_{1,2}$ modes are resonantly exited. The intensity of the T_{-1} peaks strongly responds to temperature variations. Interestingly, the TE spectrum displays much stronger diffraction peaks than those measured for TM polarization and they can be observed for all investigated temperatures. As summarized on Figure (4.6)c), the diffraction intensity of peak TE_0 and TM_1-enhanced transmission intensity increases by a factor of up to 30 when increasing the temperature from $T = 22\,°C$ to $T = 38\,°C$. This can be attributed to gradual shrinking of the

hydrogel pillars that translates to increasing their refractive index n_{hp} and leading to a stronger contrast of the hydrogel diffraction grating. The measured diffraction intensity peaks at the temperature $T \sim 38\,°C$ and then drops when further increasing temperature. At temperature $T = 50\,°C$ the diffraction efficiency is about 6 times lower than the maximum one at $T = 38\,°C$ for the TE_0-enhanced peaks. For the transmission peak amplified by TM_1 the observed changes are lower which is due to the fact that the overall signal is weaker and particularly at low intensities masked by the background (indicated as a dashed line in Figure (4.6)c). The decrease of T_{-1} diffraction efficiency is probably ascribed to the bending of pillars which was observed by AFM (see Figures (4.3) and Figure (4.4)).

4.3.5 Simulations

The measured dependence of the diffracted beam intensity T_{-1} on the swelling of nanopillars was compared with simulations in order to estimate the 3D swelling degree of pNIPAAm nanopillars. In these simulations, the optical parameters of residual pNIPAAm layer were determined by the analysis of $R_0(\theta)$ spectrum as described in the previous sections. 3D swelling of nanopillars was assumed to change height h_{hp} and diameter D of nanopillars. Refractive index of the nanopillar was homogenous and it fulfills the following equation which was derived based on effective medium theory:

$$n_{hp} = n_s \sqrt{\frac{n_p^2(1+2f_p) + n_s^2(2-2f_p)}{n_p^2(1-f_p) + n_s^2(2+f_p)}} \tag{4.2}$$

where f_p is the polymer volume fraction in hydrogel nanopillars and it can be described as $f_p = D_0^2\, h_{hp0} / D^2\, h_{hp}$, where D_0 and h_{hp0} is the diameter and height of the dry nanopillars. When raising temperature from $T = 22\,°C$ to $T = 38\,°C$, the observed change in T_{-1} diffraction efficiency amplified by TE_0 mode is ~ 30. In order to translate this increase to a volumetric change of nanopillars, dependence of T_{-1} intensity on the polymer volume content f_p was simulated at angles θ where TE_0 and TM_1 modes were resonantly excited. The obtained data are plotted in Figure (4.7)a) and they show that in the TE, diffraction efficiency is ~ 100 times higher than that in TM polarization. This difference is more pronounced than that observed experimentally which is due to the fact that much weaker coupling strength to TE

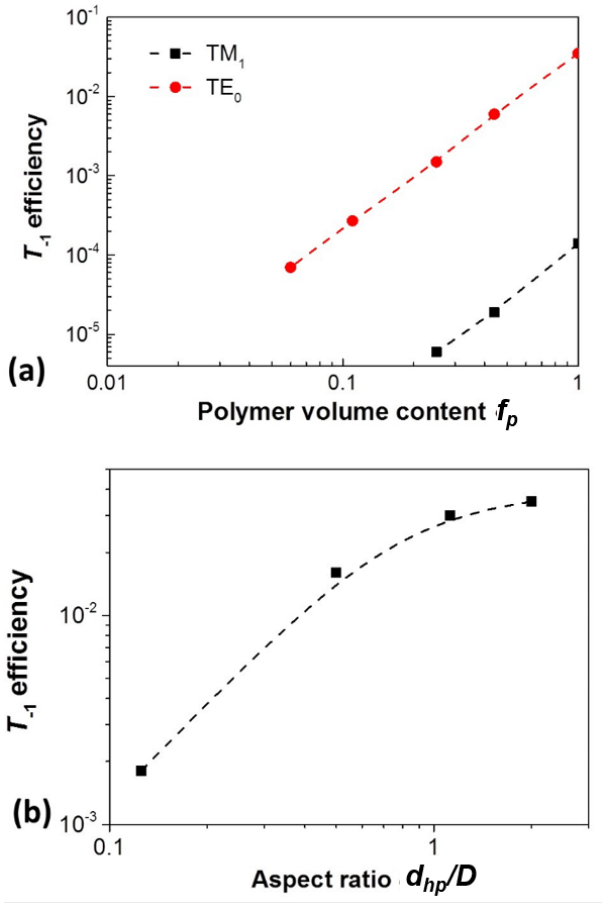

Figure 4.7: a) Simulated diffraction efficiency of T_{-1} mode amplified by the resonantly excited TM_1 and TE_0 modes (supported by a swollen hydrogel film) depending on the polymer volume fraction of the nanopillar f_p. b) Simulated dependence of T_{-1} diffraction efficiency amplified by TE_1 mode (supported by the collapsed gel) for varied aspect ratio of the collapsed nanopillar ($n_{hp} = 1.47$). Lines are guide for eyes.

modes we achieved in the experiments (see measured data and simulations in Figure (4.5)b). This can be ascribed to small variations of the thickness which smeared the TE resonances that exhibit much narrower reflectivity dips than TM resonances (which is associated with intrinsically lower Ohmic losses at the Au film). Diffraction efficiency in the log-log plot presented in Figure (4.7)a) decreases linearly when decreasing the polymer volume content f_p. The experimentally observed efficiency change by a factor of 30 corresponds to a polymer volume content change of about 5-fold. Assuming that the collapsed pillar exhibits $f_p \sim 1$ at around $T = 38\,°C$, the polymer volume content of a nanopillar in the swollen state at $T = 22\,°C$ is $f_p \sim 0.2$. This value describing the 3D swelling of a nanopillar is similar to that observed for a layer composed of identical polymer network attached to a solid support that swells in 1D. It

is contradictory to theory which suggests the volume of a hydrogel that is allowed to swell in 3D increases by a higher factor of α^3 when compared to 1D swelling with a factor of α [141]. The reason can be that this behavior observed for larger hydrogel objects may not be valid for small hydrogel nanostructures exhibiting a size comparable to the gyration radius of polymer chains.

In addition, we simulated the dependence of diffraction efficiency on the aspect ratio of arrays of pillars in the collapsed state. It confirms that lowering the aspect ratio decreases the diffraction efficiency which is consistent with the measured drop of the diffraction efficiency when raising temperature from $T = 38\,°C$ to $T = 50\,°C$ as seen in Figure (4.6)c). By comparing with the simulations, the decrease in aspect ratio observed in the experiment corresponds to a value ~ 6. This value is about twice higher than that observed with AFM (see Figure (4.4)d) and take into account h_{hp}/D).

4.4 Conclusions

A new method for in situ observation of highly swollen hydrogel nanostructures is reported and applied for the investigation of unusual properties of thermo-responsive hydrogel arrays of nanopillars. These structures were prepared from photo-crosslinkable pNIPAAm-based polymer by nano-imprint lithography. The swelling and collapsing of periodic arrays of imprinted pNIPAAm nanopillars were observed by AFM and by a combination of diffraction and OWS. *In situ* AFM was capable to capture topology of nanopillars in contact with water at temperatures above the LCST while the optical waveguide-enhanced diffraction allowed for the observation of their swelling and collapsing both below and above the LCST. With the aid of appropriate models, the key characteristics were determined from optical measurements and these results were consistent with AFM observations. Interestingly, 3D swelling degree of nanopillars was similar to the 1D swelling of a film from identical pNIPAAm hydrogel. The temperature-induced collapsing of pNIPAAm leads to the collapse of nanopillars at LCST and these structures bend when temperature in raised above LCST due to the hydrophobic interaction with underneath surface. The structure can be reversibly erased by drying at temperature below the LCST and recovered by swelling at temperature below LCST and drying at elevated temperature above the LCST. The presented approach provides versatile platform

for in situ observation of low refractive index contrast nanostructures from materials like highly swellable hydrogels. The investigated thermo-responsive material can find its applications in areas such as sensing (e.g. humidity sensor in food packaging with naked eye readout of diffraction) or safety features which will be subject to following research.

5 Tunable Plasmonic Bandgap by Responsive Hydrogel Grating

5.1 Introduction

Surface plasmon polaritons (SPPs) are optical waves that originate from collective oscillations of charge density and associated electromagnetic field at surface of metals. Optical excitation of these modes allows for tight confinement of light energy at the metal surface which is associated with enhanced field strength. These phenomena found numerous applications in areas ranging from detection and interaction analysis of biomolecules [19], light harvesting in thin film optical devices [142], to highly integrated optical circuits [143, 144]. In order to manipulate with SPPs on a 2D surface, elements such as directional couplers [145], lens [146], splitters [147], and mirrors [148, 149] were developed. Many of such elements can be designed in the form of dense periodic gratings on a metallic surface. These structures often rely on diffractive coupling of counter propagating SPPs which induces a plasmonic bandgap [150]. At wavelengths that coincide with the bandgap where Bragg scattering occurs, SPPs cease to exist and at the edges of the bandgap new coupled SPP modes with long range and short range surface plasmon characteristics occurs. Such phenomena becomes the subject of interest in studies where SPP-mediated local density of states alters emission properties of fluorescence emitters [121,151] and they were showed to provide versatile means for focusing, reflecting and splitting of 2D SPP beams [143,148]. Up to now, the majority of diffractive structures that allow for 2D control of SPP propagation are static and after they are prepared their characteristics are fixed. A possible means to actuate diffractive structures is by using thermos-responsive polymers. poly(N-isopropylacrylamide) (pNIPAAm) polymer represents a prominent example

of material that can "on demand" swell and collapse by variations of temperature around lower critical solution temperature (LCST). The swelling-collapsing strongly alters refractive index and for the crosslinked pNIPAAm hydrogel networks it can reach values as high as $\Delta n = 0.1$ [152]. It should be noted that this value is order of magnitude higher than that for other polymers used for thermo-actuating surface plasmons [153]. pNIPAAm gratings with periods of several μm were prepared by contact mask lithography and surface plasmon resonance (SPR) spectroscopy was demonstrated as an efficient tool to probe SPP-enhanced diffraction [107]. Another types of plasmonic structures that benefited from pNIPAAm in form of a microgel [154] or thin brush [155] were reported. This work reports development of dense and tunable pNIPAAm gratings on a gold surface that allows reversibly open and close the plasmonic bandgap. Large-area structures were prepared by using a photo-crosslinkable pNIPAAm-based terpolymer and UV laser interference lithography. The thermo-actuating of polymer gratings is investigated and their ability to actively tune SPP dispersion relation is demonstrated.

5.2 Materials and Method

5.2.1 Materials

A pNIPAAm-based polymer having composition of *N*-isoproprylacrylamide, methacrylic acid, and 4- methacryloyloxy benzophenone in a ratio of 94:5:1, respectively as seen in Figure (3.7b) was synthesized as reported earlier [138]. Ethanol of analysis grade was purchased from Merck Milipore. SU-8 2000 and its thinner (SU-8 2000 thinner) was purchased from Micro Resist Technology GmbH, Germany. Pre-cut BK7 glass substrates of dimension 20 mm x 20 mm x 1 mm were purchased from VWR International GmbH, Austria.

5.2.2 Substrate Preparation

BK7 glass substrates were coated by vacuum thermal evaporation with 1.5 nm thick chromium and 47 nm thick gold layers. On the top of the gold surface, a thin SU-8 polymer layer of thickness about 5 nm was spin-coated from $c = 2$ vol% solution (dissolved by SU-8 thinner) at a spin rate of 5000 rpm for 60 seconds, in order to serve as a linker for the subsequent attachment

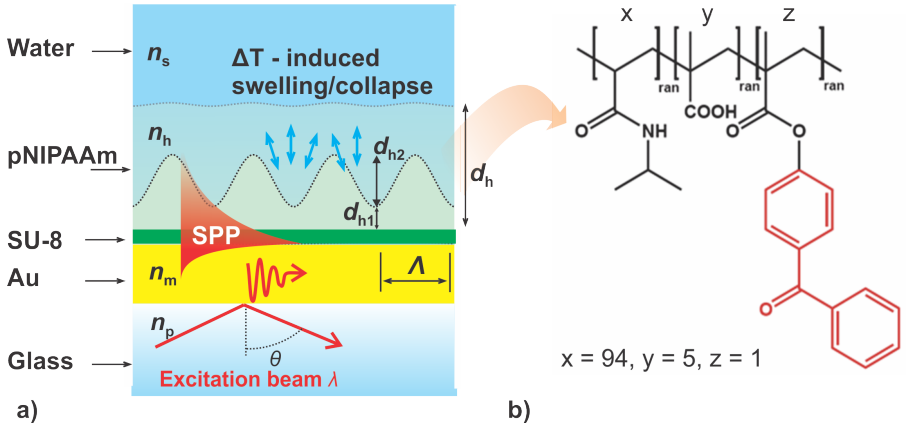

Figure 5.1: (a) Schematics of prepared grating structures with a pNIPAAm-based hydrogel and b) chemical structure of used photo-crosslinkable poly(*N*-isopropylacrylamide-co-methacrylic acid-co-4-methacryloyloxy benzophenone) (pNIPAAm) polymer.

of the hydrogel film. After the spin-coating of SU-8, substrates were dried in vacuum oven at $T = 50°\text{C}$ for 2 hrs. For the preparation of hydrogel layers, an ethanol solution with pNIPAAm polymer ($c_{\text{pp}} = 2\,\text{wt\%}$) were spin-coated at the spin rate of 2000 rpm for 2 min. Subsequently polymer layers were dried in a vacuum oven overnight at $T = 50°\text{C}$ and was exposed to interfering collimated beams of intensity $360\,\mu\text{W}\,\text{cm}^{-2}$ (in LIL setup as seen in Figure (3.1)) that were emitted by a He-Cd laser ($\lambda = 325\,\text{nm}$). Angle between the interfering beams was adjusted between $\theta = 35.48°$ and $21.17°$ which corresponds to the period of harmonically oscillating intensity of $\Lambda = 280\,\text{nm}$ and $450\,\text{nm}$. In order to prepare crossed gratings, the interference field of two beams was sequentially recorded onto the sample oriented at 0 and 90°. Irradiation time was adjusted between $t = 20 - 30$ min in order to take into account different angles of incidence of interfering beams θ so that the average the dose was kept constant at $0.69\,\text{Jcm}^{-2}$. In the areas with high laser beam intensity, crosslinking of polymer layer networks occurs due to the benzophenone groups attached to the pNIPAAm polymer backbone. Afterwards the substrates were thoroughly rinsed with water and dried on a hot plate at $T = 150\,°\text{C}$. The morphology of dried pNIPAAm gratings were observed by using Atomic Force Microscopy (AFM) in air.

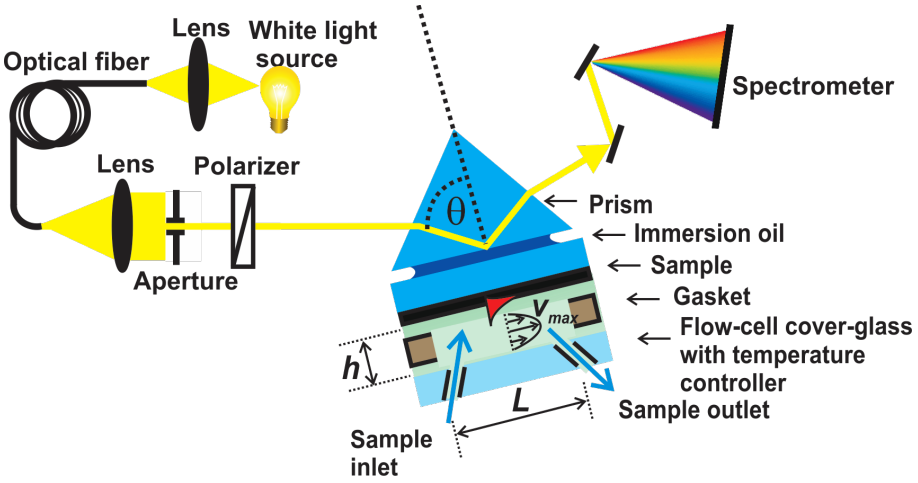

Figure 5.2: Schematic of used optical setup for the measurement of SPR reflectivity spectra as a function of wavelength λ and angle of incidence θ for a gold surface in contact with water and controlled temperature T.

5.2.3 Imaging of Cross-grating

The observation of morphology of prepared cross-grating layers were performed by using Atomic force microscopy (AFM) in tapping mode. Two different type of observation were made for these cross-gratings: (1) swelling the hydrogel in water and collapsing it on hot plate at elevated temperature $T = 150\,°C$ and (2) swelling the hydrogel in water and drying with stream of air. All measurement were made in air at room temperature.

5.2.4 Optical Setup

Angular-wavelength spectra $\lambda(\theta)$ was measured by an optical setup (see Figure (5.2)) utilizing ATR method with the Kretschmann configuration as described in section (3.2.4). In brief, the light from a white light source is coupled to an optical fibre and the output light from fibre is collimated by an achromatic lens ($f = 6$ cm). This collimated white light beam after passing through a polarizer was coupled to a LASFN9 glass prism and reflected from the base of prism for an angle of incidence θ. A glass substrate with prepared layer supporting SPPs and pNIPAAM grating was optically matched to the prism base by using index matching immersion oil. The excitation of SPs and appearance of bandgap by the light beam hitting the gold layer was observed from the angular-wavelength spectra $\lambda(\theta)$ measured by using a high-resolution spectrometer and a rotation stage with resolution of coupling angle $\theta = 0.005°$ through an

in-house built software tool developed in LabVIEW (National Instruments, USA) [121]. An in-house developed flow-cell with temperature control by Peltier device was used as described in section (3.4). The reflectivity measured for transverse magnetic (TM) polarization was normalized with that measured for transverse electric (TE) polarization.

5.2.5 Simulations

Simulation of diffraction coupling of between counter-propagating SPPs by the hydrogel grating was performed numerically by using finite element method (FEM) that was implemented in a diffraction grating solver DiPoG (Weierstrass Institute, Germany). The refractive index of LaSFN9 was assumed as n_p = 1.845 and that of water as n_s = 1.33. Refractive index of gold was assumed to be dispersive $n_m(\lambda)$ and it was taken from Palik [136]. Refractive index of SU-8 was set to 1.48 and the presence of chromium was omitted. The attached pNIPAAm hydrogel refractive index was n_h = 1.36 in swollen state and n_h = 1.48 in collapsed state. It should be noted that for simplicity the grating was assumed as one dimensional (surface was modulated only in one lateral direction that lied in the place of incidence). The modulation profile was assumed to be sinusoidal with a period Λ modulation depth of d_{h2}. Additional residual hydrogel layer with a thickness d_{h1} in between the modulated zone and SU-8 was assumed.

5.2.6 Optical Properties of Nanostructure

Angular reflectivity spectra $R(\theta)$ were analyzed by using a Fresnel reflectivity-based model implemented in Winspall software (developed at Max Planck Institute for Polymer Research in Mainz, Germany). This tool allows fitting of refractive indices and thickness of used stack of layers (in which we assumed that the birefringence is negligible) by least squares method. It should be noted that a "box" model was used as prepared composite films were assumed to be homogeneous perpendicular to the surface. Prior to fitting of n_h and d_h parameters of chromium, gold and SU-8 layers were determined on reference samples.

5.3 Results and Discussion

5.3.1 SPR and OWS Measurement

Firstly, the swelling of a pNIPAAm layer that was crosslinked by only one beam emitted from HeCd laser was measured by SPR and optical waveguide spectroscopy. In this experiment one of the UV interfering beams was blocked in order to crosslink the pNIPAAm layer homogeneously with a dose of 0.69 Jcm^{-2}. After the rinsing with water and drying, the thickness of pNIPAAm layer was determined as $d_h \sim 72$ nm and the refractive index was $n_h = 1.48$ as seen in Figure (5.3) by the fitting angular reflectivity spectra $R(\theta)$ measured by SPR. When the layer swelled in contact with water at room temperature $T = 22\,°C$, its thickness increased to $d_h \sim 370$ nm and refractive index decreased to $n_h = 1.36$ which corresponds to the swelling ratio of about SR~ 5. The reason for the refractive index decrease is the replacement of the polymer by water which exhibits lower refractive index $n_s = 1.33$. When increasing the temperature, the hydrogel layer collapses at pNIPAAm LCST of $T = 32\,°C$. At the temperature of $T = 37\,°C$ the hydrogel layer exhibited thickness similar to that measured in the dry state $d_h \sim 69$ and the refractive index of $n_h = 1.48$. It should be noted that these observations on one-dimensional swelling constrained perpendicular to the layer surface are in accordance with our previous studies when identical pNIPAAm film was crosslinked with a broad spectrum of non-coherent UV light centered at a wavelength of $\lambda = 365\,$nm with a dose $5 - 20\,$Jcm^{-2} [156].

5.3.2 Observation of Structures by AFM

Series of pNIPAAm gratings with period $\Lambda = 280 - 450\,$nm were recorded with two (interfering) coherent UV beams and same average dose of 0.69 Jcm^{-2}. After recording sinusoidally modulated crosslinking density, the pNIPAAm layer was rinsed with water in order to remove loosely bound polymer chains from areas that were exposed to weak UV light intensity. In water at room temperature $T = 22\,°C$, the polymer network swells and polymer chains rearrange in order to minimize the swelling-induced stress. After subsequent drying the pNIPAAm grating surface, such rearrangement occurs also due to the surface tension and it completely erases the structure (see the completely flat surface at Figure (5.4)a) for a structure with recorded $\Lambda = 310\,$nm). Interestingly, as seen in Figure (5.4)b) when the same structure is allowed to

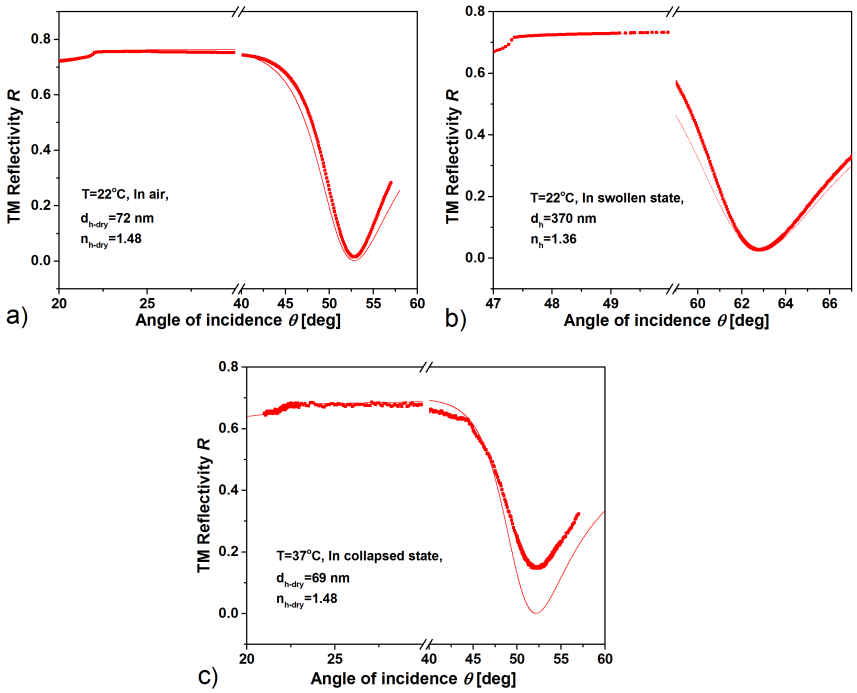

Figure 5.3: Angular reflectivity spectra measured for structured hydrogel in trans-magnetic (TM) polarization upon contact with a) air at $T = 22\,°C$, b) swollen in water at $T = 22\,°C$ and c) collapsed at $T = 37\,°C$ on hotplate and measured in contact with air. The spectra were fitted with transfer matrix-based model as indicated by lines.

swell in water at temperature $T = 22\,°C$ and it is subsequently dried at a higher temperature above the LCST, the written pattern is recovered. The reason is that when raising temperature the hydrophobicity of pNIPAAm gradually increases [139] and the polymer collapses to form a structure that resembles the original recorded cross-linking density pattern. Afterwards, the water evaporates from the surface and recorded modulated crosslinking density can be observed as a relief grating (see Figure (5.4)).

As can be seen in Figure (5.4)b), the relief grating with $\Lambda = 310\,nm$ exhibits deep features with a depth of about $d_{h2} = 80\,nm$ in air but its periodicity is perturbed which can be attributed to the process of collapsing and drying. Upon the collapsing of pNIPAAm chains at elevated temperature the polymer becomes hydrophobic and thus neighboring domains interact and disturbs the (originally periodic) structure. This effect can be expected to be more pronounced when the thickness in the swollen state d_h is comparable with the period Λ. In order to check this effect, two gratings with the same thickness d_h, and one with a shorter period $\Lambda =$

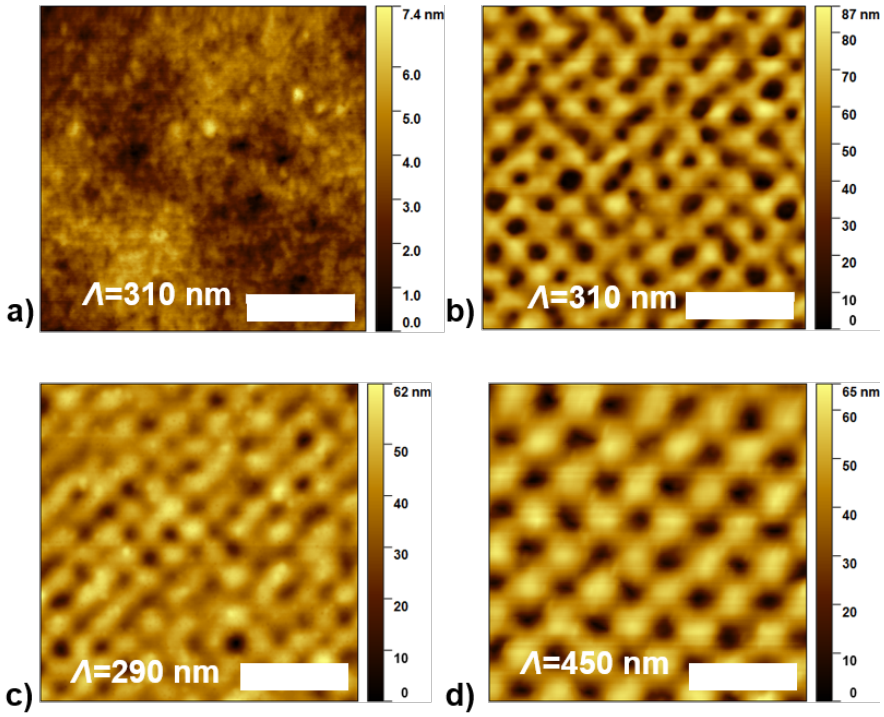

Figure 5.4: AFM observation of pNIPAAm grating with $\Lambda = 310\,\text{nm}$ that was dried at a) room temperature $T = 22°\text{C}$ and at b) elevated temperature of $T = 150°\text{C}$. Comparison of the c) denser grating with $\Lambda = 290\,\text{nm}$ and d) sparser grating with $\Lambda = 450\,\text{nm}$ observed after drying at elevated temperature. Scale bar corresponds to the length of $1\mu\text{m}$.

290 nm and another with longer period $\Lambda = 450\,\text{nm}$ were examined. As seen in Figure (5.4)c), the shorter period structure is significantly more perturbed than the longer period one in Figure (5.4)d) which confirms that the ratio of thickness d_h and period Λ plays a crucial role in the swelling and collapsing of the highly open pNIPAAm network nanostructure.

5.3.3 Selection of Period by Simulations

For the diffraction coupling of counter propagating SPPs on the Au surface, the period has to fulfill the following phase matching condition:

$$2\text{Re}\{k_{SPP}\} = 2\pi/\Lambda\,, \tag{5.1}$$

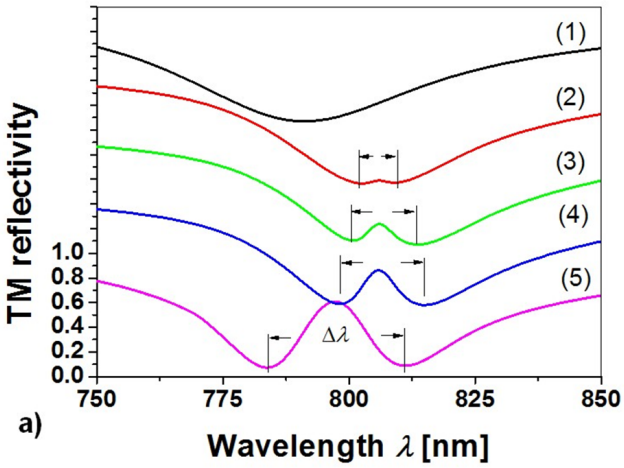

b)

	d_{h1} [nm]	d_{h2} [nm]	n_h	θ [deg]	$\Delta\lambda$ [nm]
(1)	372	0	1.36	51.1	0
(2)	60	25	1.48	51.4	7.4
(3)	47	50	1.48	51.3	11.5
(4)	37	70	1.48	51.3	17
(5)	2	140	1.48	50.5	28

Figure 5.5: a) Simulated wavelength reflectivity spectra for a flat swollen pNIPAAm film (1) and series of combinations of modulation depth d_{h2} and residual layer thickness d_{h1} of a collapsed pNIPAAm film. Subsequent reflectivity curves are offset by 0.2. b) Summary of parameters used in the above simulations with the angle of incidence θ and plasmonic bandgap width $\Delta\lambda$.

where k_{SPP} is the (complex) propagation constant of SPPs. In order to induce the plasmonic bandgap at the wavelength around $\lambda \sim 800\,\text{nm}$ on a gold surface in contact with water, the period $\Lambda = 280\,\text{nm}$ was determined by series of following numerical simulations presented in Figure (5.5).

As seen in Figure (5.5)a), wavelength reflectivity spectra were simulated for the geometry representing the swollen and collapsed hydrogel grating. In the swollen state, a homogeneous layer with the thickness of $d_h = 372\,\text{nm}$ and refractive index $n_h = 1.36$ was assumed [curve (1)]. For the collapsed state, refractive index of the pNIPAAm of $n_h = 1.48$ was assumed and the outer interface with water was sinusoidally modulated [curves (2)-(5)]. As summarized in the table presented in Figure (5.5)b), the thickness of residual layer d_{h1} was adjusted for each modulation depth d_{h2} so the volume of the collapsed layer was kept fixed. The reflectivity curve (1) shows that for a swollen hydrogel film the coupling of incident light and the angle of incidence $\theta = 51.1°$ is manifested as a resonant dip centered at $\lambda = 780\,\text{nm}$. For the collapsed

state of the polymer [curves (2)-(5)], this resonances is split to two branches that become stronger separated when increasing the modulation depth d_{h2}. The reason for the splitting is opening of plasmonic bandgap due to the Bragg scattering of SPPs described by Equation (5.1). This scattering leads to the cancelling of SPP propagation in a band centered at wavelength $\lambda \sim 800\,\text{nm}$ and when increasing the modulation depth d_{h2} the spectral width $\Delta\lambda$ is increasing. As the average refractive index probed by the SPPs for each geometry is slightly changing, the angle of incidence θ was adjusted for each configuration so the reflectivity curve crosses through the middle of the gap and the minima associated to the lower wavelength SPP branch and higher wavelength SPP branch are the same. It is worth of noting that these two branches correspond to the ω^+ and ω^- modes at the edges of plasmonic bandgap [151] with the field confined in the polymer or water. The low frequency mode is confined closer to the surface of the samples while the higher frequency component has a longer evanescent tail. The reflectivity curves (2)-(5) indicate that the collapsed linear hydrogel grating allows for opening a bandgap with the width $\Delta\lambda$ that approximately changes linear with d_{h2} and can reach $\Delta\lambda = 28\,\text{nm}$ for the modulation depth $d_{h2} = 140\,\text{nm}$ of a linear grating.

5.3.4 Angular Wavelength Spectroscopy

The optical characteristics of the dense pNIPAAm grating with period $\Lambda = 280\,\text{nm}$ were observed in contact with water at different temperatures by angular-wavelength spectroscopy using Kretschmann configuration of the attenuated total reflection (ATR) method that was implemented as shown in Figure (3.4). In this optical setup, structured polymer film attached to the gold surface were probed by resonantly excited SPPs and changes in their dispersion relation was measured upon swelling and collapsing the responsive polymer structure. The spectra was measured by using a polychromatic white light beam that was launched into a high refractive index prism with optically matched glass substrate carrying a stack of layers consisting of 47 nm of gold, a thin SU-8 linker layer, and the structured hydrogel film. The angle of incidence θ of the light beam hitting the surface was varied by using a rotation stage and the reflected beam intensity was detected by using a photodiode. In order to excite optical modes with transverse magnetic (TM) or transverse electric (TE) polarization, a rotational polarizer was used.

The opening and closing of plasmonic bandgap was experimentally observed on pNIPAAm grating with a period of $\lambda = 280\,\text{nm}$. As seen in Figure (5.6), there was measured reflectivity dependence on the angle of incidence θ and wavelength λ. These measurements were carried out at temperature $T = 22°\,\text{C}$ where pNIPAAm structure swells in water (see Figure (5.6)a) and it was increased to $T = 34, 37, 40$ and $45\,°\,\text{C}$ when it collapses. The resonant excitation of SPPs manifests itself as a dark band in the reflectivity spectrum which shifts to higher angles θ when decreasing the wavelength λ. At temperature above the pNIPAAm LCST ($T > 32°\,\text{C}$) the average refractive index of the polymer layer probed by SPPs increases due to the collapsing of the pNIPAAm structure which is accompanied with the occurrence of SPR band at higher angles θ. In addition, the collapse of the pNIPAAm is associated with periodic modulating of refractive index. This grating induces splitting in the SPP dispersion relation due to the diffraction coupling of counter propagating SPPs on the surface as predicted by simulations in Figure (5.5). In order to evaluate the width of the bandgap a cross-section of SPR reflectivity at θ_r indicated in Figure (5.6)a-e) was taken and plotted in Figure (5.6)f). These plots show that the gradual collapse of the grating leads to the opening of plasmonic bandgap. Interestingly, the width of the bandgap increases with temperature and reaches its maximum of $\Delta\lambda = 12\,\text{nm}$ at around $T = 37°\,\text{C}$. When further increasing the temperature to 40 and $T = 45°\,\text{C}$, the bandgap width $\Delta\lambda$ slightly decreases which can be attributed to increasing hydrophobicity of the polymer and possible additional changes in the structure. When comparing the experimentally measured maximum bandgap width in Figure (5.6) with simulations in Figure (5.5), the modulation depth of pNIPAAm grating can be estimated as $d_{h2} \sim 50\,\text{nm}$ which is lower than values typically observed by AFM on prepared samples (see Figure (5.4)). This discrepancy can be attributed to two following effects. Firstly, the grating observed *ex situ* in air exhibit probably more defects and flatter structure than that which is probed in water by SPPs. Secondly, the experimental data were measured on a crossed grating and the simulations were (for simplicity) carried out for a linear grating. Therefore, the modulation depth used in experiments is effectively decreased by a factor of two by averaging in the direction perpendicular to SPP propagation.

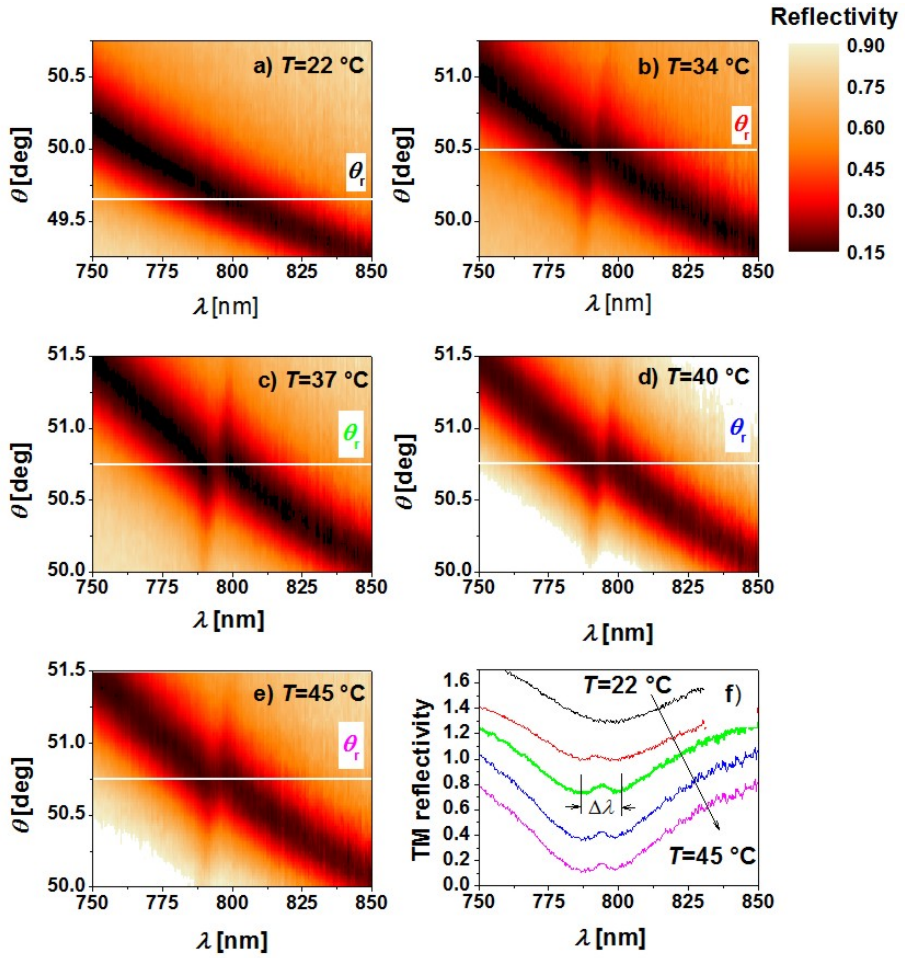

Figure 5.6: Measured reflectivity dependence on θ and λ for a pNIPAAm grating with the period $\lambda = 280\,\text{nm}$ and temperature a) $T = 22°\text{C}$, b) $T = 34°\text{C}$, c) $T = 37°\text{C}$, d) $T = 40°\text{C}$, and e) $T = 45°\text{C}$. f) Cross-section of reflectivity at each temperature for indicated angle of incidence θ_{res} at which bandgap occurs for a pNIPAAm grating with the period $\lambda = 280\,\text{nm}$. Subsequent reflectivity curves are offset by 0.3.

5.4 Conclusions

This work show that laser interference lithography can be used for the preparation of nanogratings from a photo-crosslinkable pNIPAAm-based polymer. Series of experiments were performed which shows that bandgap can be controlled by varying the temperature and their position can be controlled by choosing a suitable period for the cross-grating structure. Reversible swelling and collapsing of structure with refractive index contrast of about $\Delta n \sim 0.1$ when brought into contact with water with temperature is able to switch *on* and *off* Bragg scattering of surface plasmon that is associated with opening a bandgap in the dispersion relation.

A crossed grating structure with period as small as 280 nm and modulation depth in collapsed state of 60-80 nm was prepared and employed for opening and closing of a bandgap of SPPs. The angular and wavelength spectroscopy of surface plasmon polaritons demonstrated that a bandgap width of about 12 nm can be open for SPPs on gold surface and wavelength of $\lambda \sim 800$ nm. In order to further enlarge the spectra width of plasmonic bandgap the modulation depth of the structure can be further increased or the upper surface of the responsive polymer can be decorated with material that increases the refractive index contrast. We believe that this approach in conjunction with e.g. embedded ITO microheaters [156] may find its application to 2D plasmonic optics and provide facile means to actively manipulate with SPP beams.

6 Plasmonic Nanohole Arrays Actuated by Responsive Hydrogel Cushion

6.1 Introduction

Extraordinary transmission of light through metallic nanohole arrays (NHAs) has been the focus of intense research in last decade [157–160]. This enhanced transmission phenomenon has been attributed to the resonant excitation of surface plasmon polaritons (SPPs) and it allows for efficient tunneling of light through (otherwise opaque) metallic film at narrow wavelength bands [160, 161]. Numerous factors affecting the transmission spectrum has been studied in details, including shape, depth, periodicity, aperture area and aspect ratio of the holes and type of metal [40, 159–163], respectively. Simplicity at which the spectral peaks in transmission spectrum can be tuned by modifying the geometry of nanohole arrays by modern nano-fabrication techniques such as focused ion beam (FIB) milling [40], laser interference lithography (LIL) [164], electron beam lithography [165], and template stripping [166], has paved the way for their application in label-free biosensing [40, 165, 167], fluorescence spectroscopy [168], and in spectral filtering devices [169]. Among these applications, label-free surface plasmon resonance (SPR) biosensing, in particular, has been widely explored because of its commercial success in pharmaceutical research [166]. Conventional designs of plasmonic nanostructures are static and their optical properties are fixed after they are prepared. In order to actuate resonant coupling to surface plasmons on metallic nanostructures, they have been interfaced with inorganic materials exhibiting electro-optically [170, 171] or magneto-optically [172, 173] modulated refractive index. In parallel, other organic materials have been explored for stronger actuating of surface plasmon resonance by refractive index-

variations associated with photochromic effect [174] and liquid crystal phase transitions [175] as well as by mechanical changes induced by specific molecular binding [176] and responsive polymers [177]. Among systems that utilize responsive polymers, poly(N-isopropylacrylamide) (pNIPAAm) holds a prominent stage due to its strong swelling and collapsing by variations of temperature around its lower critical solution temperature (LCST) ~ 32°C. This polymer was explored in form of a brush for SERS applications in order to tune the near field coupling between Au nanoparticles and a continuous Au surface [155]. pNIPAAm-based networks with dispersed Au nanoparticles [178] displayed tunable LSPR wavelength due to the changes in near field plasmonic coupling. Long range surface plasmons were actuated by crosslinked pNIPAAm-based hydrogel layer on the top of a small ITO micro-heater [156].

This work presents a new plasmonic nanostructure that is tunable by thermo-responsive pNIPAAm-based hydrogel and that can be prepared by template stripping. It consists of a thin Au film with NHA that allows for diffraction coupling of propagating SPP. This structure is tethered to a solid surface by pNIPAAm-based hydrogel cushion which respond to temperature variations. It can rapidly swell and collapse which triggers flow of water through the plasmonic pores and strongly modulates the refractive index leading to changes in the transmission spectrum mediated by surface plasmon modes.

6.2 Materials and Method

6.2.1 Materials

Off-Stoichiometry Thiol-Enes polymer (OSTEmer 321) was purchased from Mercene Labs. Ethanol of analysis grade was purchased from Merck Millipore. Ethylene glycol (EG) was purchased from Sigma-Aldrich. Polydimethylsiloxane (PDMS, Sylgard 184) was purchased from Sigma-Aldrich. pNIPAAm based terpolymer (composed of N-isoproprylacrylamide, methacrylic acid, and 4-methacryloyloxy benzophenone in a ratio of 94:5:1) was synthesized as reported before [99]. (3-thiopropyl)oxybenzophenone (BP-thiol) was synthesized as described in literature [179].

6.2.2 Preparation of Metallic Nanohole Arrays

The nanohole arrays were fabricated by e-beam lithography (EBL). The designed nanoholes with diameter $D = 208\,\text{nm}$ and period $\Lambda = 406\,\text{nm}$ were written in an area of $1.2 \times 1.2\,\text{mm}^2$ on electron beam resist (220 nm thick of NEB22) coated on a $600\,\mu\text{m}$ thick silicon wafer, by using ELS-7000 (Elionix) with an exposure of $178\mu C\,\text{cm}^{-2}$ at a current of 800 pA. Oxylene was used to develop the resist. A 50 nm thick Au layer was deposited on the developed patterns in a Denton Explorer E-beam deposition machine at deposition rate of $2\,\text{Å}/s$. After that, the e-beam resist and gold lift-off process was accomplished by soaking the wafer inside Remover 1165.

6.2.3 Polymer Deposition

The silicon wafer with Au NHA was incubated in 1 mM BP-thiol ethanol solution for 24 hrs in order to form a self-assembled mono-layer (SAM). Afterwards, the surface was rinsed with ethanol and dried in a stream of air. Then, a thin pNIPAAm layer was prepared by spin-coating (Model G3P-8, SCG) an ethanol solution with polymer concentration of 3 wt%. The spin rate was set to 2000 rpm for 2 min. Subsequently polymer layer was dried in a vacuum oven (VT6025, Thermo scientific) overnight at $T = 50°\text{C}$ and crosslinked by using a UV-lamp (Bio-Link 365, Vilber, Germany) with ($\lambda = 365\,\text{nm}$) with an irradiation dose of $25\,\text{J}\,\text{cm}^{-2}$. Crosslinked polymer layer were rinsed thoroughly with water to remove any loosely bounded polymer chains and dried with stream of air.

6.2.4 Template Stripping

OSTEmer 321 epoxy was dropped on a surface of BK7 glass substrate and contacted with a flat block of PDMS in order to spread homogeneously. Then OSTEmer 321 polymer was crosslinked through the PDMS by a UV-lamp at $\lambda = 365\,\text{nm}$, irradiation dose of $3\,\text{J}\,\text{cm}^{-2}$. Afterwards, PDMS stamp was peeled-off leaving the glass substrate with rubbery polymer layer on top. This glass substrate was pressed against pNIPAAm layer on a silicon wafer with Au NHA and put into oven at $T = 50°\text{C}$ overnight in order to heat cure. The silicon wafer substrate is then stripped off using sharp blade leaving the glued surface on glass substrate

and detaching from silicon wafer.

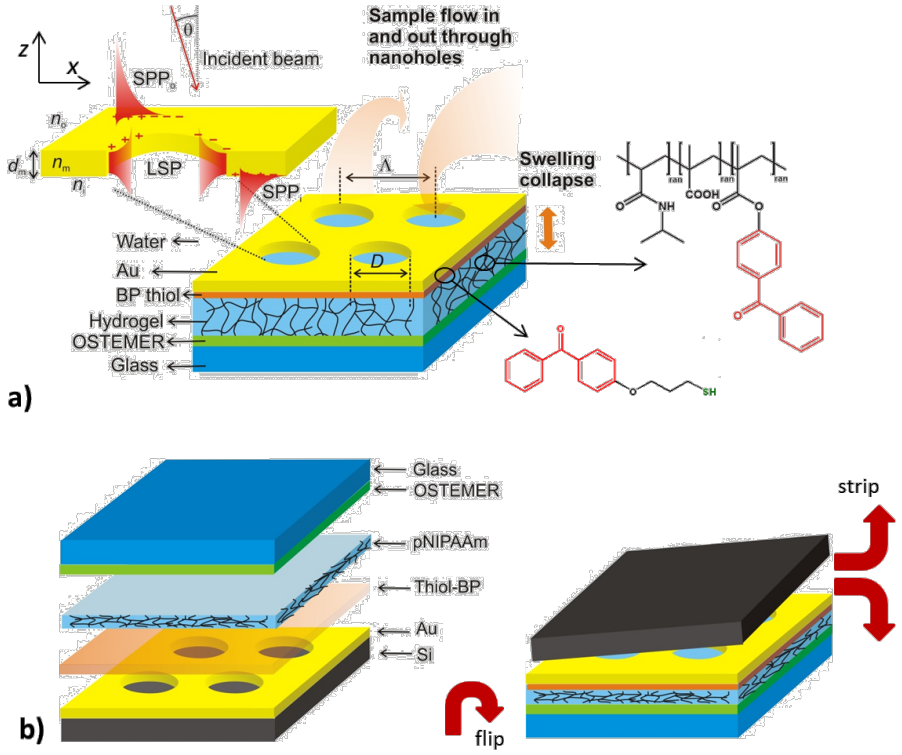

Figure 6.1: a) Schematics of the investigated structure with Au nanohole arrays attached to a responsive pNIPAAm-based hydrogel cushion by a thiol-BP monolayer. b) Preparation of the structure by using template stripping from a Si wafer.

6.2.5 Imaging of Nanohole Array

Stripped substrate with NHAs on top and hydrogel underneath were observed using scanning electron microscopy (SEM) (Carl Zeiss EVO, a low voltage of 5 kV was used). In order to image the cross-section of the prepared layers, a substrate was broken and an angular stage was used for SEM imaging of the exposed layer edge. In addition to SEM imaging, atomic force microscopy (AFM) (Molecular Imaging PicoPlus) was used in tapping mode to observe the morphology of the surface. Stripped substrate with nanohole surface was also looked through microscope (Olympus soft Imaging Solution, Model BX51M, camera SC30) in dry and swollen state.

6.2.6 Optical Setup

Transmission spectra were measured using an in-house developed system and it consists of a white light source (halogen lamp LSH102, LOT-Oriel, Germany) that was connected to a multimode optical fiber (M26L02, Thorlabs, USA). Polychromatic light from the optical fiber output was focused by an achromatic lens (f = 6 cm, 14 KLA 001, CVI Melles Griot, Germany) at the tunable plasmonic structure. The focused light beam passed through the glass substrate with Au NHA attached by a responsive hydrogel cushion under angles of incidence spanning between $\theta = 0°$ and $\theta = 4°$. The plasmonic structure was mounted on a translation stage for selecting area with Au NHA and a reference pad with flat Au. Transmitted light was coupled via a lens (F810SMA-635, Thorlabs, USA) into a multimode optical fiber (M26L02, Thorlabs, USA) that was connected to a high-resolution spectrometer (SR-303i-B, Andor, USA). The acquired spectra were dark current compensated and the raw spectrum measured on Au NHA was normalized with that obtained on a flat Au surface. Temperature dependent measurements were performed by using a flow-cell with a Peltier device which was pressed against the sample chip with Au NHA.

6.2.7 Simulations

Finite difference time domain (FDTD) model implemented by Lumerical Inc. (Canada) was used for simulation of near field and far field optical properties of investigated structures. A unit cell with the width equal to the period Λ was defined and symmetric boundary conditions in x and y axis was used. In the z direction, perfect matched layer was placed at the distances of $1\,\mu m$ above and below the layer stack, respectively. A transmission monitor was placed $0.7\,\mu m$ below the metal layer. For simulating the near field distribution of electric field intensity there was employed a 2D monitor in the xz plane.

6.3 Results and Discussion

6.3.1 Template Stripped NHA with Responsive Hydrogel Cushion

As illustrated in Figure (6.1)a), the investigated plasmonic structure consists of Au film with NHA that is attached to a pNIPAAm-based hydrogel layer. When brought in contact with aqueous environment, water flows though the pores in the perforated Au film into the underneath hydrogel which swells. pNIPAAm polymer exhibits thermo-responsive properties which enables collapsing the polymer network when the structure is heated above the LCST and thus to expel water through the structured Au membrane. The thermo-responsive pNIPAAm / Au NHA structure was prepared from a 50 nm thick perforated Au film on a silicon wafer with native oxide film. In order to attach the pNIPAAm-based hydrogel to the Au surface, it was modified by a thiol self-assembled monolayer with benzophenone functional groups (BP-thiol). The modified Au surface was subsequently coated by pNIPAAm-based terpolymer that carries benzophenone groups covalently attached to polymer chains. After the pNIPAAm polymer layer was dried, it was exposed to UV light in order to crosslink the polymer chains and simultaneously attach them to the Au surface by using the benzophenone moieties. Afterwards, the Au NHA with pNIPAAm polymer networks was stripped by using a UV pre-cured OSTEmer layer, see Figure (6.1)b). This rubbery film was pressed against the pNIPAAm-based surface and bonded via epoxy groups at elevated temperature. Finally, the stack of layers was stripped from the Si wafer leaving the Au NHA film on the top of a crosslinked pNIPAAm-based hydrogel cushion.

As seen in Figure (6.2)a), the developed process allowed for successful stripping of Au film with NHA. SEM images revealed that the arrays of nanoholes exhibited a diameter of $D = 208\,\text{nm}$ and period $\Lambda = 406\,\text{nm}$. It should be noted that the structured area with NHA was square shaped with dimensions of $1.2 \times 1.2\,\text{mm}$. Optical microscopy was used to image a corner of the structured pad as rendered in Figure (6.2)b). Dark area in this figure represents the NHA structure and the brighter more reflective area is flat Au. The left figure shows an optical microscope image of structured area that was brought in contact with water at temperature of $T = 22°\text{C}$. It reveals that the Au layer wrinkles due to the swelling of the underneath pNIPAAm hydrogel film. Such wrinkling was observed for other hydrogel films and it is associated with

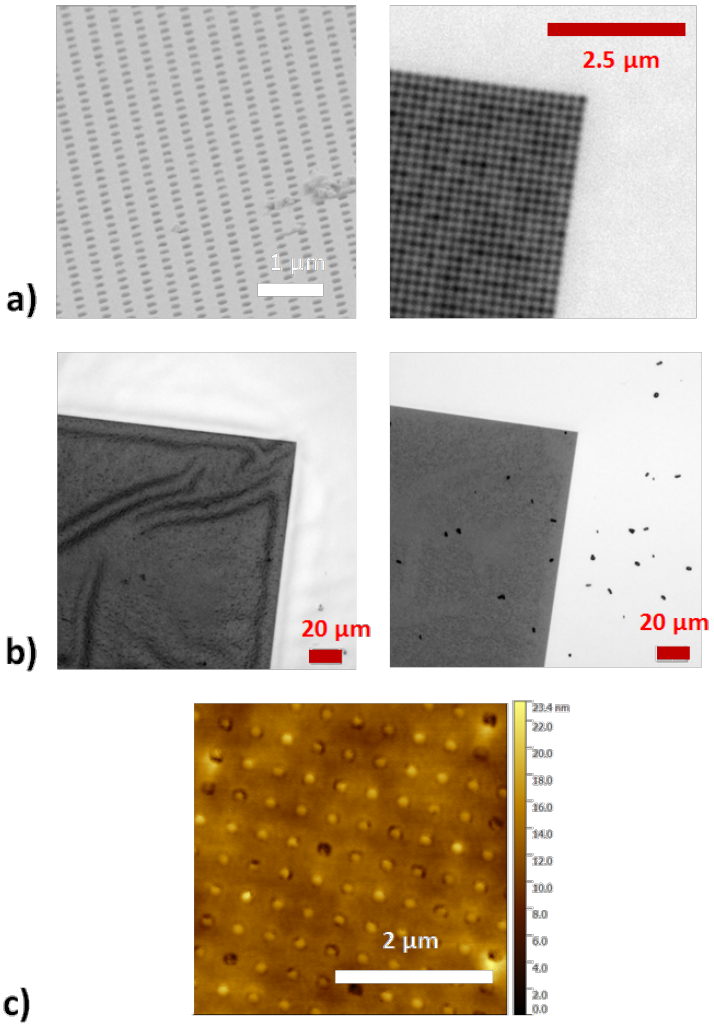

Figure 6.2: a) Observation of stripped surface of Au NHA by using SEM (left) and optical microscopy with the magnification of 100x (right). b) Optical microscope images of an Au NHA surface with a structured pad (dark area) when swollen in water (left) subsequently dried (right). c) AFM observation of the stripped Au surface with NHAs after exposing to water and drying.

stress induced by the swelling constrained to the direction perpendicular to the surface [156]. Afterwards, the surface was dried and water rapidly diffused through the NHA pores away from the hydrogel film. Interestingly, the 50 nm thick Au film did not exhibit cracks and defects after the swelling and drying as seen in the right image in Figure (6.2)b) acquired by optical microscopy. In addition, AFM was used for the characterization of Au NHA on the top of the hydrogel cushion after it was swollen and dried. The acquired image in Figure (6.2)c) shows that most of the pores in Au film were filled with the pNIPAAm-based polymer which partially protrudes above the Au surface. In addition, one can see that the Au surface between the

pores was smooth (rms roughness of 0.5 nm) and without cracks. At larger scale the Au surface become slightly undulated after swelling and collapsing of pNIPAAm-based hydrogel which can be probably ascribed to the rearrangement of pNIPAAm polymer chains below the Au membrane after the swelling and drying.

6.3.2 Swelling of Hydrogel Cushion Layer

Optical waveguide spectroscopy was used to characterize the swelling and collapsing of pNIPAAm-based polymer film. In this study, identical pNIPAAm layer was prepared on flat 50 nm Au layer deposited on a glass substrate. Attenuated total reflection method with Kretschmann geometry was used to probe the polymer film with resonantly excited surface plasmons and dielectric waveguide modes. As described in our work [180], the analysis of observed resonances allowed us determining thickness and refractive index of pNIPAAm-based film. The thickness of dry pNIPAAm polymer film was measured as $d_{h-dry} = 212\,\text{nm}$ and refractive index as $n_{h-dry} = 1.48$. When the film was brought in contact with water at temperature of $T = 22°\text{C}$, it swells and increases its thickness to $d_h = 1158\,\text{nm}$ which corresponds to the swelling ratio of $SR = 5.5$. As the polymer chains are diluted after the swelling, refractive index of layer decreases to $n_i = 1.36$ which is close to that of water $n_o = 1.33$ at the used wavelength $\lambda = 633\,\text{nm}$. The thickness of the film was measured in temperature range $T = 22 - 40°\text{C}$ and the LCST has been observed around 32°C. At the temperature of $T = 40°\text{C}$, the refractive index of the hydrogel film was $n_i = 1.46$ which about 0.1 higher than that in swollen state at $T = 22°\text{C}$.

6.3.3 Actuating Spectrum of Surface Plasmons Modes

The thin Au film supports SPP modes at its upper and bottom interfaces. When the upper surface is in contact with air with $n_o = 1$, SPP_o modes that travel along this interface are leaky into the polymer below with refractive index of $n_i = 1.48$. At the opposite interface, guided SPP_i modes propagate and their field is mostly confined at the inner interface between Au and the polymer. The structuring of Au film with periodic NHA allows for diffraction coupling of light to SPP_o and SPP_i modes via $(\pm 1, 0)$ and $(0, \pm 1)$ orders. As presented in Figure (6.3), this coupling manifests itself as distinct resonant features in the wavelength transmission

spectrum. These spectra were measured with a polychromatic light beam that was focused (the angular range of $\theta = 0 - 4°$) at NHA and transmitted light was collected and analyzed by a spectrometer. The obtained spectra were normalized by those measured on a reference pad with flat 50 nm thick Au film. For the structure in contact with air, there can be seen two Fano resonances that exhibit themselves as a spectral band where the transmission drops down at lower wavelengths and increases at higher wavelengths, see Figure (6.3)a). The first resonance is associated with the excitation of surface plasmon SPP_o at the outer interface (between Au / air) and exhibits a minimum at around 500 nm and peaks at around 640 nm. The second resonance is due to the excitation of surface plasmon SPP_i at the inner interface (between Au and dry pNIPAAm) and it has its minimum at around 720 nm and peaks at a wavelength above 800 nm. As the same figure shows, SPP_i resonance blue shifts after flowing water over the surface kept at temperature of $T = 22°$C. The SPP_i resonance minimum decreases by about 15 nm which can be attributed to diffusing of water through nanoholes, swelling of the pNIPAam cushion, and accompanied decrease in its refractive index from $n_i = 1.48$ to 1.36. The minimum of the SPP_o resonance increases by about 50 nm as the refractive index above the structure changes from $n_o = 1$ to 1.33.

The permeability of the Au membrane with NHA was tested by a series of refractometric experiments in which the upper and bottom interfaces were probed by SPP_o and SPP_i modes. Firstly we changed refractive index of an aqueous solution that was flowed over the surface by spiking with ethylenglycol (EG). Samples with EG concentrations between 0 - 40 vol% were prepared which correspond to refractive indices of $n_o = 1.33 - 1.37$. Transmission spectra were measured for swollen pNIPAAm cushion at temperature of $T = 22°$C as presented in Figure (6.3)b). These results show that both SPP_o and SPP_i resonances shift to longer wavelength when increasing the concentration of EG. The SPP_o resonance is increased by about 12 nm when changing the refractive index n_o by 0.04. SPP_i resonance responds stronger and it shifts by about 26 nm upon such a change in n_o. This observation indicates that the EG can diffuse through the NHA into the underneath swollen hydrogel that is probed by SPP_i. It should be noted that the change of SPP_i resonance to EG is much stronger than that observed for the SPP_o mode which is probably due to a collapse of pNIPAAm and additionally enhanced n_i associated with the presence of EG.

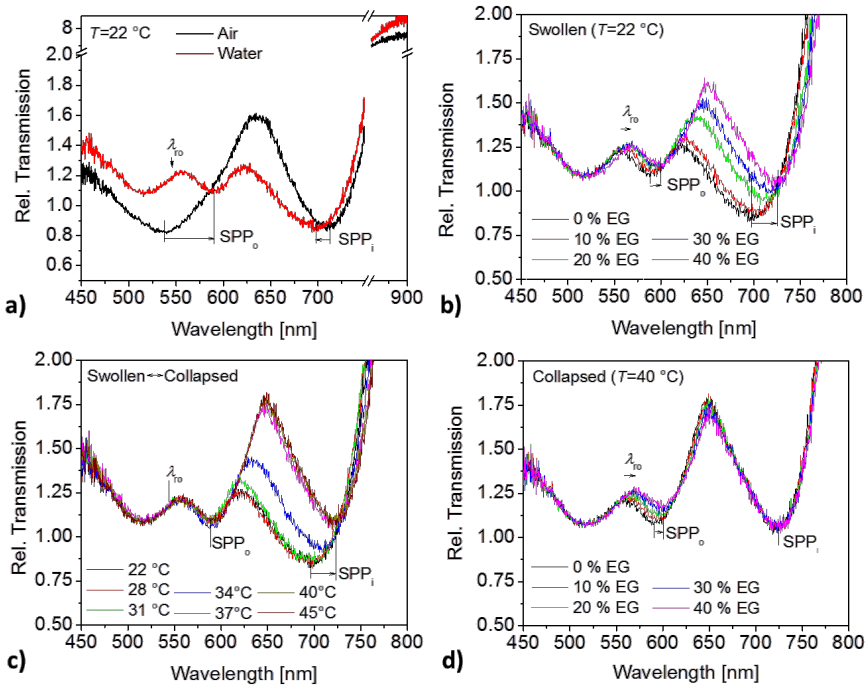

Figure 6.3: Measured transmission spectra for the Au NHA on a responsive pNIPAAm hydrogel cushion a) in contact with air and water at $T = 22°$C, b) in contact with water spiked by ethylenglycol (n_o = 1.33 – 1.37) swollen cushion at $T = 22°$C, c) in contact with water ($n_0 = 1.33$) and temperature changed in the range $T = 22 - 45°$C in order to actuate the pNIPAAm cushion, and d) in contact with water spiked with ethylenglycol ($n_o = 1.33 - 1.37$) with collapsed cushion at $T = 40°$C.

In order to prove the identity of transmission features that were assumed to be associated with the excitation of SPP$_i$ and SPP$_o$, refractive index at was changed only at the inner side of the structure by the collapse of pNIPAAm cushion. In order to do so, temperature of water flowed over the structure was gradually raised from $T = 22°$C to $T = 40°$C. As Figure (6.3)c) reveals, SPP$_o$ resonance that probes the upper water medium shifts negligibly with the temperature (refractive index of water changes only by $\sim 0.002\,°\text{C}^{-1}$ at 632 nm). However, SPP$_i$ resonance that probes the inner interface shifts strongly by 26 nm which is due to the expelling of water through the pores and collapsing of the hydrogel. The presented data confirm that the collapse of pNIPAAm occurs above LSCT of 31°C similar to pNIPAAm film without the metallic structure on the top. For the collapsed pNIPAAm cushion at $T = 40$°C, we repeated identical experiment when samples spiked with EG were flowed over the surface. The measured data in Figure (6.3)d) indicate that SPP$_o$ resonance responds similar as at $T = 22$°C (see Figure (6.3)b) and shifts by about 11 nm due to the increase of n_o from 1.33 to 1.37. No change in SPP$_i$ resonance occurs which confirms that the hydrogel at collapsed state prevents diffusing of

aqueous sample through the Au pores.

6.3.4 Simulations

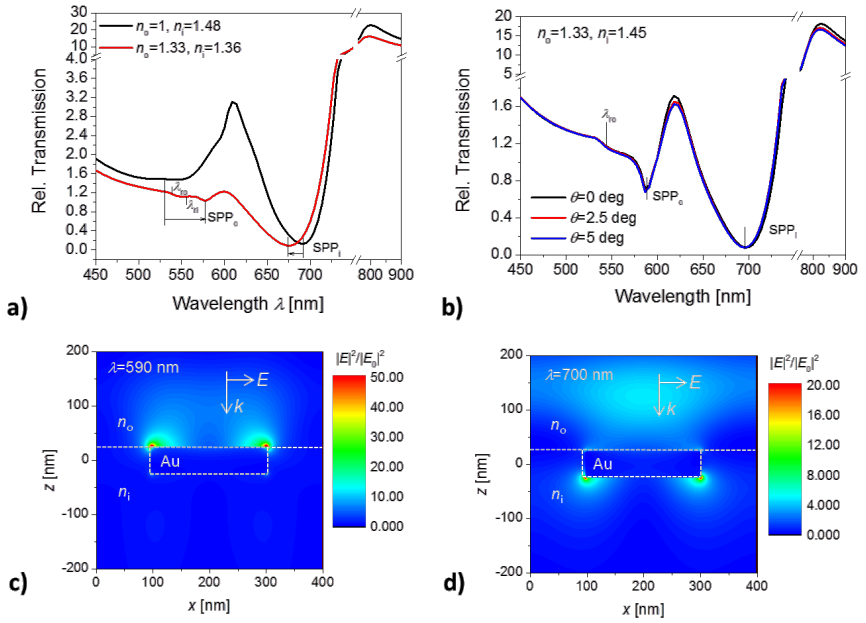

Figure 6.4: Simulated transmission spectra for Au NHA that is a) in contact with air ($n_o = 1$, $n_i = 1.48$) and water ($n_o = 1.33$, $n_i = 1.36$) and the optical beam hits normally the surface $\theta = 0$. b) Comparison of transmission spectra for collapsed geometry ($n_o = 1.33$, $n_i = 1.46$) and varied angle of incidence between $\theta = 0$ and 5°. Near field distribution of electric field intensity $|E/E_0|^2$ normalized with that of the incident plane wave that was simulated for collapsed NHA structure ($n_o = 1.33$, $n_i = 1.45$) c) at wavelength of $\lambda = 590\,\text{nm}$ where SPP_o is excited and d) at $\lambda = 800\,\text{nm}$ where SPP_i occurs.

The experimental data were verified by simulations presented in Figure (6.4) and Figure (6.5). The simulated transmission spectrum for geometry with $n_o = 1.33$ and $n_i = 1.36$ qualitatively agree with that measured at $T = 22°\text{C}$ when the hydrogel cushion swells in water (compare Figure (6.4)a) and Figure (6.3)a). The SPP_o resonance minimum occurs at around 590 nm and the one associated with SPP_i at around 690 nm. It should be noted that the refractive index below and above the Au film is similar ($n_o \sim n_i$) when the hydrogel swells which leads to the coupling of surface plasmons across the Au layer. SPP_o mode excited at lower wavelengths exhibit nature of long range surface plasmons with electric field weakly confined in the Au layer. Contrary to this, the SPP_i mode exhibit nature of short range surface plasmons with field strongly confined in the Au film. When the hydrogel film is collapsed ($n_o = 1.33$ and $n_i = 1.46$), the symmetry is broken and SPP_i and SPP_o modes travel at individual interfaces.

Figure (6.4)b) illustrates that resonances for such geometry does not shift substantially when angle of incidence θ is varied which is due to the fact that the NHA opens a bandgap and flattens dispersion relation of these modes. In order to check for the identity of the observed resonances, near field distribution of electric intensity was simulated at the resonance wavelength 590 nm and 700 nm as seen in Figure (6.4)c) and d), respectively. These images confirm that the lower wavelength resonance SPP$_o$ is associated with probing the upper surface of Au film in contact with water and the bottom interface with polymer attached is probed by the longer wavelength resonance SPP$_i$.

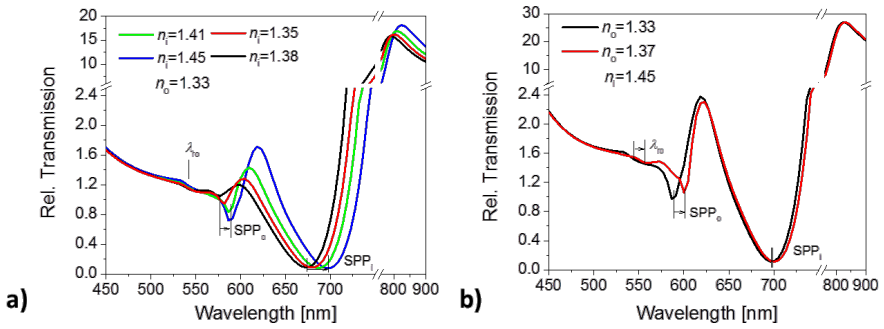

Figure 6.5: a) Transmission spectra simulated for increasing refractive index n_i from 1.35 to 1.45 representing the collapse of pNIPAAm cushion in contact with water (n_0 = 1.33). b) Transmission spectra for increasing the refractive index n_0 from 1.33 to 1.37 that represents varying the liquid refractive index above a collapsed pNIPAAm cushion (n_i = 1.45).

Finally, the simulations of sensitivity of SPP$_o$ and SPP$_i$ resonances to the refractive index above n_0 and below n_i the Au NHA were carried out. The simulated transmission spectrum for n_i varied between 1.36 and 1.46 resembles the experiment with collapsing the gel (presented in Figure (6.3)c). The simulated data in Figure (6.5)a) show a shift in SPP$_i$ minimum of 24 nm which is similar to the measured value. However, the simulated changes in SPP$_o$ resonance are much stronger than experimentally observed. We assume that this can be attributed to the fact that the hydrogel present in the pores protrudes to above upper interface. This can lead to additional refractive index changes that are not taken into account in the model. The complementary case when the refractive index of the medium above the surface is presented in Figure (6.5)b). These simulations are related to the experiment in Figure (6.3)d) when refractive index n_o was changed from 1.33 to 1.37 and pNIPAAm hydrogel cushion with n_i = 1.46 when collapsed. The obtained results predict shift of about 13 nm of the SPP$_o$ resonance which is

close to the measured value. In addition, in agreement with the experiment the response of SPP_i mode is negligible.

6.4 Conclusions

Facile approach for tethering a thin Au NHA to a thermo-responsive hydrogel cushion is reported and the optical properties of structure are characterized in detail. Series of experiments show that water can pass through the pores in Au NHA and swell the underneath hydrogel. Refractometric experiment confirms that molecules dissolved in water can diffuse through the pores into the swollen polymer networks. When the hydrogel collapses by a temperature stimulus, water is expelled through the pores and then they are closed. In the swollen state the hydrogel generates refractive index symmetrical geometry that leads to establishing long range and short range SPPs. When the gel is collapsed, the refractive index symmetry is perturbed and SPPs at individual interfaces are exited. Reversible swelling collapsing of the hydrogel is accompanied with strong refractive index change of 0.1 which can be used for tuning of wavelength at which plasmonically enhanced transmission occurs. In conjunction with rapid control of temperature around the LCST [156], this approach may find its applications in actively tunable optical filters. In addition, the reported structure can be implemented to plasmonic biosensors where analyzed samples are flowed through the nanoholes in order to overcome diffusion-limited transfer of analyte to the surface. Such architecture typically relies on thin nitride membranes with metallic nanoholes fabricated by multiple lithography steps [39, 165]. The presented approach may provide simpler means for its preparation and enable to fully harness this intriguing biosensor concept.

7 MIP Waveguides for Detection of Low Molecular Weight Analytes

7.1 Introduction

Numerous label-free optical sensor platforms were combined with molecularly imprinted polymers (MIP) [181] for detection of chemical and biological analytes including those utilizing surface plasmon resonance (SPR), [182, 183] dielectric optical waveguides, [184, 185] reflection interference spectroscopy (RIfS), [186, 187] and diffractive structures [188–190]. These optical sensors rely on the measurement of refractive index variations that are associated with a capture of target molecules by MIP on the sensor surface. With respect to established antibody recognition elements, the bio-mimetic MIP materials offer the advantage of superior stability and potentially lower cost. MIPs have been most often synthesized on the sensor surface in-situ in the form of bulk polymer films by using thermal or photo-initiated polymerization in the presence of template molecules [191, 192]. However, this approach provides only limited density of accessible binding sites in close proximity to the outer surface of the MIP layer, which impedes the sensor sensitivity. In order to provide a more open structure, which can carry higher amounts of binding sites that are available for capture of diffusing target analyte, there were investigated MIP films, which were structured by using sacrificial colloidal crystals [189, 193] and optical lithography [192] or formed by imprinting of loosely crosslinked hydrogels [89, 194]. These systems were reported to be capable of direct detection of small molecular analytes at typically μM−mM concentrations [183]; however, several works reported the limit of detection at as low as pM concentrations [189, 195].

Besides MIP layers, well-controlled synthesis of molecularly imprinted polymer micro and

nanoparticles (nanoMIP) was carried out by using precipitation, emulsion, or miniemulsion polymerization with a template dispersed in solution [196] or attached to particle or bead carriers [197]. NanoMIPs represent versatile materials that can be further processed and, e.g., their affinity purification allowed selecting nanoMIP fractions with dissociation affinity constants K_d as good as $10^{-8} - 10^{-9}$ M that makes them competing with regularly used antibodies [197, 198]. In optical sensor applications, nanoMIP monolayers were attached to the sensor surface by means of physisorption [199], affinity reactions [200], or covalent binding [187] for the capture of target analyte.

The present work reports on a new material that holds potential to improve the sensitivity of MIP optical sensors. It is based on a composite film architecture comprising a hydrogel polymer network that is loaded with nanoMIPs. Such 3D structure can accommodate increased amounts of nanoMIPs compared to a 2D monolayer systems and it exhibits an open structure through which target molecules can rapidly diffuse into the imprinted binding pockets. Moreover, swollen hydrogel nanoMIP composite film can simultaneously serve as a waveguide, which confines probing optical field in the region where specific molecular binding events occur [201, 202].

7.2 Materials and Methods

7.2.1 Materials

L-Boc-phenylalanine-anilide (L-BFA) with the molecular weight of 353 $g\,\mathrm{mol}^{-1}$ and reference non-target analytes including ethylene glycol (EG) with 62.07 $g\,\mathrm{mol}^{-1}$, L-Boc -phenylalanine (L-BPA) with 265.3 $g\,\mathrm{mol}^{-1}$, L-Boc-Tryptophan (L-BTP) with 304.3 $g\,\mathrm{mol}^{-1}$, and L-Boc-tyrosine (L-BTS) with 281.3 $g\,\mathrm{mol}^{-1}$ were obtained from Sigma–Aldrich. Methanol and ethanol of analysis grade was purchased from Merck Millipore. Sodium dihydrogen phosphate (NaH_2PO_4) was purchased from Sigma–Aldrich. Working buffer was prepared from 80×10^{-3} NaH_2PO_4 aqueous solution (with the pH adjusted to 7 by titrating NaOH) that was mixed with methanol at volumetric ratio of 1:1. After adding the methanol and spiking the working buffer with specific and reference analytes, all salts in the solution were dissolved. SU-8 2000 and its thinner (SU-8 2000 thinner) was purchased from Micro Resist Technology GmbH, Germany.

7.2.2 Synthesis of Polymers

Molecularly imprinted polymer nanoparticles were synthesized by thermal initiated miniemulsion polymerization as reported previously [196, 203]. Two sets of poly[(ethylene glycol dimethylacrylate)-(methacrylic acid)] nanoparticles were prepared, one was imprinted with L-BFA template molecule (nanoMIP) and the second was not imprinted with the template molecule (nanoNIP). pNIPAAm-based hydrogel (composed of *N*-isopropylacrylamide, methacrylic acid, and 4-methacryloyloxy benzophenone at a ratio of 94 : 5 : 1, respectively, as seen in Figure (7.1)b) was synthesized as reported before [99].

7.2.3 Preparation of NanoMIP Composites

LASFN9 glass substrates were coated by vacuum thermal evaporation with 1.1 nm thick chromium and 47 nm thick gold layers. On the top of the gold surface, an SU-8 polymer film with a thickness of about 10 nm was spin-coated from $c = 4.8\,\text{vol\%}$ solution (dissolved by SU-8 thinner) at spin rate 6000 rpm in order to serve as a linker for the subsequent attachment of a composite film. After the spin-coating of SU-8, substrates were dried in a vacuum oven at 50° C for 2 hrs. For the preparation of composite layers, an ethanol solution with nanoparticles ($c_{\text{NP}} = 0 - 6\,\text{wt\%}$) and pNIPAAm polymer ($c_{\text{pp}} = 1\,\text{wt\%}$) were spin-coated at the spin rate 2000 rpm for 2 min. Prior to the spin-coating, the particle solution was sonicated (Elmasonic S10) for 30 min in order to reduce aggregation. Composite polymer layers were dried in a vacuum oven overnight at 50° C and cross-linked by UV light ($\lambda = 365\,\text{nm}$) with the irradiation dose of $25\,\text{Jcm}^{-2}$. Then, layers were extensively rinsed with ethanol in order to remove loosely bound polymer chains and polymer nanoparticles followed by drying in a stream of air.

7.2.4 Imaging of NanoMIP Composites

The observation of morphology of prepared layers was performed by using SEM (Carl Zeiss EVO, a low voltage of 5 kV was used). In order to image the cross-section of the prepared layers, a substrate was broken and an angular stage was used for SEM imaging of the exposed layer edge.

7.2.5 Optical Setups

Angular reflectivity spectra $R(\theta)$ were measured by SPR spectrometer with Kretchmann configuration that was described in our previous works [201]. Briefly, monochromatic laser beam from a He–Ne laser ($\lambda = 632.8\,\text{nm}$) was coupled to a LASFN9 glass prism and reflected from the base of prism for an angle of incidence θ. A sensor chip was optically matched to the prism base by using index matching immersion oil. The excitation of SP and OW waves by the laser beam hitting the gold layer was observed from the angular reflectivity spectra $R(\theta)$ measured by using a photodiode detector and a rotation stage with resolution of coupling angle $\theta = 0.005°$. The kinetics of affinity binding reactions was observed by using an another SPR spectrometer that utilized wavelength modulation of resonant coupling to guided waves [204]. In this system, a polychromatic light from a supercontinuum source (WhiteLase micro, Fianium, UK) was collimated and made incident on BK7 glass prism at a fixed angle θ. Reflected light was coupled into a spectrometer (S2000, Ocean Optics, USA) to perform spectral analysis and wavelength shifts in resonant dips occurring in the wavelength reflectivity spectrum $R(\lambda)$ were determined in time by a dedicated software SPR UP (developed at the Institute of Photonics and Electronics in Prague, Czech Republic). In both measurements with angular and wavelength modulation, identical composite layers were used. Against the sensor surface carrying composite waveguide with nanoMIP or nanoNIP, a flow cell was attached and analyzed samples prepared from a working buffer were pumped by using a peristaltic pump with a Tygon MHLL tubing (IDEX Health & Science SA, Switzerland).

7.2.6 Optical Properties of the Composites

Thickness and refractive index of composite layers were determined by the fitting angular reflectivity spectra $R(\theta)$ measured by an optical setup with angular modulation of SPR. These spectra were analyzed by using a Fresnel reflectivity-based model implemented in Winspall software (developed at Max Planck Institute for Polymer Research in Mainz, Germany). This tool allows fitting of refractive indices and thicknesses of used stack of layers (in which we assumed that the birefringence is negligible) by least squares method. From the fitted refractive index of the composite film that is swollen n_h, the polymer volume fraction f in the swollen

state was obtained from effective medium theory as:

$$f = \frac{(\{\mathrm{Re}(n_h)\}^2 - n_b^2)(\{\mathrm{Re}(n_{h-dry})\}^2 + 2n_b^2)}{(\{\mathrm{Re}(n_h)\}^2 + 2n_b^2)(\{\mathrm{Re}(n_{h-dry})\}^2 - n_b^2)} \tag{7.1}$$

where n_b is refractive index of the solvent (working buffer) and $n_{h-dry} = 1.48$ is the refractive index of the used polymers. It should be noted that a "box" model was used as prepared composite films were assumed to be homogeneous perpendicular to the surface. Prior to fitting of n_h, d_h, and d_{h-dry}, parameters of other chromium, gold and SU-8 layers were determined on reference samples.

7.3 Results and Discussion

7.3.1 Preparation of nanoMIP Composites

As illustrated in Figure (7.1), composite polymer films were prepared by deposition from an ethanol solution with dispersed imprinted (nanoMIP) or control non-imprinted (nanoNIP) poly[(ethylene glycol dimethylacrylate)-(methacrylic acid)] nanoparticles (diameter D ≈ 190 nm) that were mixed with a photo-crosslinkable poly(*N* -isopropylacrylamide)(pNIPAAm)-based hydrogel. After the solution was spun over the sensor surface, the layer was dried and crosslinked by irradiation with UV light ($\lambda = 365$ nm). The density of nanoparticles embedded in the film was controlled by the concentration of nanoMIP or nanoNIP (c_{NP}) and photo-crosslinkable pNIPAAm polymer (c_{pp}) in ethanol.

7.3.2 Imaging of nanoMIP Composites by SEM

The cross-section of dry composite layers with varied nanoMIP density was observed by scanning electron microscopy (SEM). The obtained results presented in Figure (7.2)a) reveal that the amount of loaded nanoparticles increases with their concentration in solution (c_{NP} varied between 3 and 6 wt%) that was blended with pNIPAAm polymer at a fixed concentration ($c_{\mathrm{pp}} = 1$ wt%) and spun on the sensor surface. Thickness of the dry composite films d_{h-dry} is increasing with polymer nanoparticle concentration c_{NP} and its morphology is changing. For

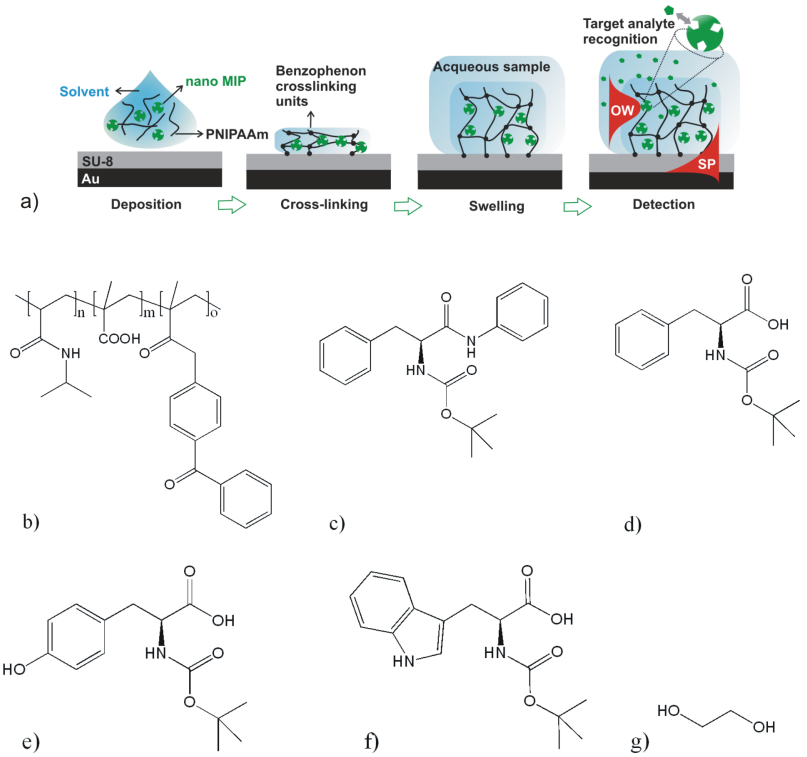

Figure 7.1: a) Preparation of composite layer with embedded nanoMIPs and chemical structure of used materials, b) poly (*N*-isopropylacrylamide-co-methacrylic acid-co-4-methacryloyloxy benzophenone) (pNIPAAm), c) L-Boc-phenylalanine-anilide (L-BFA), d) L- Boc-phenylalanine (L-BPA), e) L-Boc-tyrosine (L-BTS), f) L-Boc-tryptophan (L-BTP), g) ethylene glycol (EG).

high polymer nanoparticle concentrations c_{NP}, the interstitial volume between the nanoparticles is mostly void and pNIPAAm hydrogel is present only at contact areas between the polymer nanoparticles. For small polymer nanoparticle concentration c_{NP}, the volume of the film is mostly occupied by pNIPAAm hydrogel with sparsely distributed nanoparticles inside. Figure (7.2)b) shows that the morphologies of composite films loaded with same amounts of nanoMIP and nanoNIP are similar when using an identical protocol (c_{NP} = 6 wt% and c_{pp} = 1 wt%).

7.3.3 Optical Setup

The characteristics of composite films before and after their swelling in a working buffer (mixture of 80×10^{-3} M phosphate buffer and methanol at 1:1 ratio, pH = 7) were observed by optical waveguide spectroscopy (OWS) that was implemented as shown in Figure (7.3)a). In

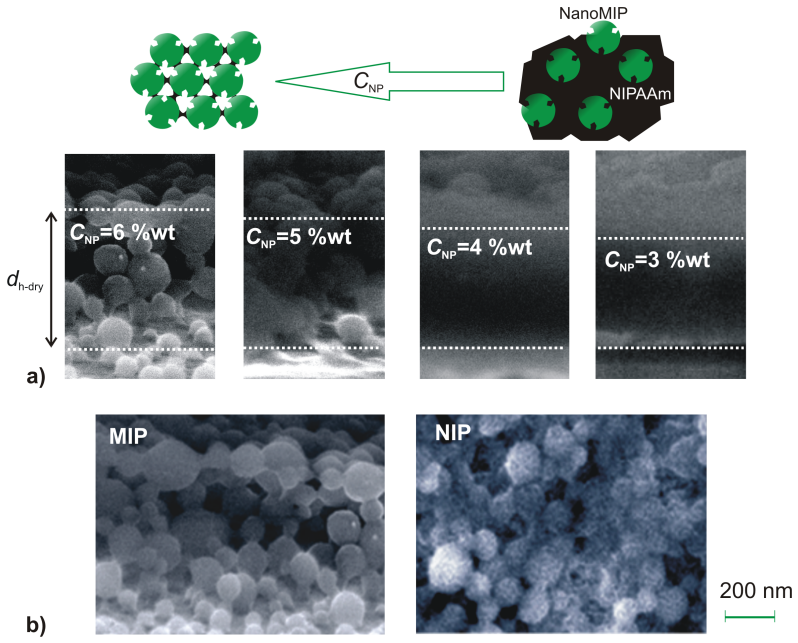

Figure 7.2: SEM cross-section images of dry a) nanoMIP composite films prepared from a solution with $c_{pp} = 1$ wt% and $c_{NP} = 3-6$ wt% and b) comparison of nanoMIP (left) and nanoNIP (right) structures.

this optical setup, composite polymer film attached to the gold surface served as a waveguide, which confines light propagation by the highly reflective metallic surface and by total internal reflection at the interface between the composite film and liquid medium. Such films support multiple guided optical waves (OW - marked further as $TM_{1,2}$ and $TE_{0,1}$) that can be coupled with far field optical waves by using the Kretschmann configuration of the attenuated total reflection (ATR) method. The spectrum of guided waves was measured by using a laser beam with the wavelength of $\lambda = 632.8$ nm that was launched into a high refractive index prism with optically matched glass substrate carrying a stack of layers consisting of 47 nm gold, a thin SU-8 linker layer, and the composite film. The angle of incidence θ of the light beam hitting the surface was varied by using a rotation stage and the reflected beam intensity was detected by using a photodiode. In order to excite optical modes with transverse electric (TE) or transverse magnetic (TM) polarization, a rotational polarizer was used.

7.3.4 Reflectivity Measurements

Figure (7.4)a-d) shows that the resonant excitation of guided waves in the composite polymer film is manifested as series of dips in the TM and TE angular reflectivity spectrum $R(\theta)$. As

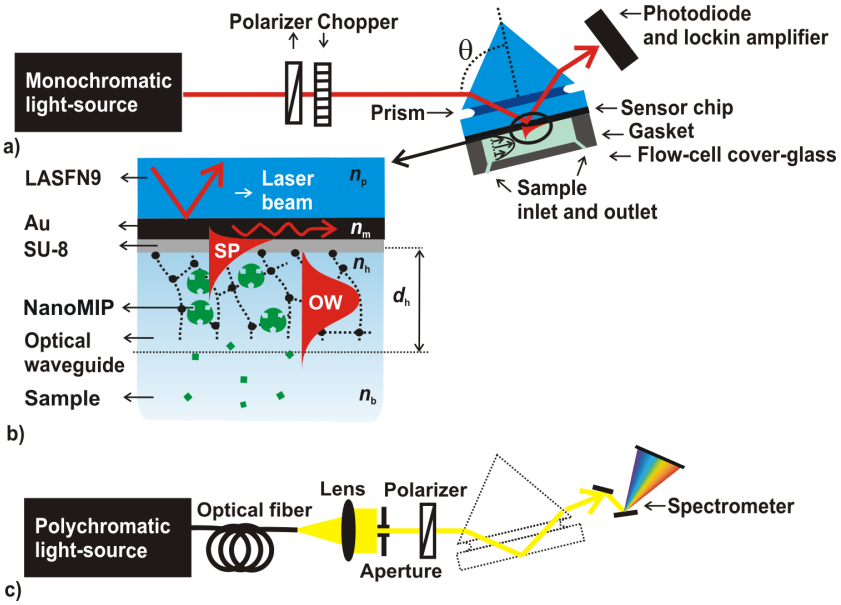

Figure 7.3: Schematic of sensor surface architecture and optical setup used for optical waveguide spectroscopy utilizing a surface plasmon resonance spectrometer with a) angular and c) wavelength interrogation. b) Detail of the sensor surface architecture with the polymer composite waveguide.

described further, fitting of these curves by a Fresnel reflectivity-based model was used for the determining of (complex) refractive index n_h of prepared layers as well as of their thicknesses in swollen d_h or dry d_{h-dry} states. The real part of the refractive index Re$\{n_h\}$ relates to the density of the film and allowed us determining the total polymer volume fraction of the film f. Let us note that the polymer volume fraction is inversely proportional to the swelling ratio $f = 1/\mathrm{SR}$, which is defined as the ratio of thicknesses in the swollen and dry states $\mathrm{SR} = \frac{d_h}{d_{h-dry}}$. Imaginary part of the refractive index Im$\{n_h\}$ reflects the damping of OW modes due to the scattering at nanoparticles embedded in the waveguide. In general, Re$\{n_h\}$ can be obtained by fitting the angular position of the resonance (angle θ_r at which the minimum of reflectivity dip occurs) and Im$\{n_h\}$ can be determined from the angular width of the resonance $\delta\theta_r$. Example of measured and fitted reflectivity curves in Figure (7.4) shows that studied films supported at least two OW modes in TE and TM polarizations. The simultaneous analysis of multiple OW modes allowed for independent determining of thicknesses d_h and d_{h-dry} as well as respective refractive index n_h. As can be seen in Figure (7.4)b), the resonant coupling to SP mode occurs at significantly lower angle than model based on fitting OW modes suggests. The reason is that the average refractive index of the composite slice, which is probed by SPs (distance up to about 100 nm from the gold surface) comprises only a small portion of nanoparticles with the

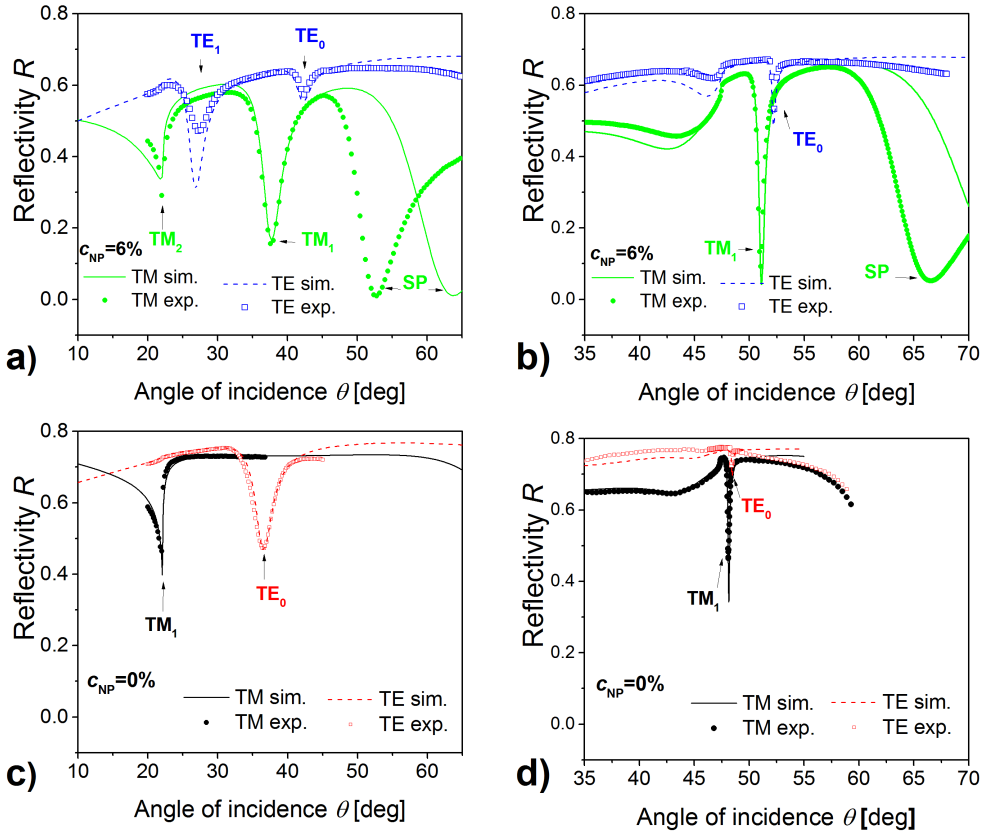

Figure 7.4: Angular reflectivity spectra for dry (left a and c) and swollen (right b and d) layers prepared from a solution with concentration of nanoMIP $c_{NP} = 6\,wt\%$ and pNIPAAm $c_{pp} = 1\,wt\%$ (top a and b) compared to that prepared from a solution with $c_{NP} = 0\,wt\%$ and $c_{pp} = 3\,wt\%$ (bottom c and d). Measured and fitted curves for transverse magnetic (TM) and transverse electric (TE) polarization are shown as indicated in graphs.

diameter D $\approx 190\,nm$ and thus obtained n_h is different from that determined by the analysis of OWs (that is averaged across the whole, around micrometer thick, composite film). Therefore, only OW resonances $TE_{0,1}$ and $TM_{1,2}$ were fitted and the SP resonance was omitted in further analysis.

The thickness of dry composite film that was prepared from the solution with dissolved pNIPAAm at the concentration of $c_{pp} = 1\,wt\%$ and polymer nanoparticles with the concentration $c_{NP} = 6\,wt\%$ was fitted as $d_{h-dry} = 587\,nm$ (Figure (7.4)a), which is in accordance with SEM observations presented in Figure (7.2). In working buffer, pNIPAAm in this composite layer swells, which leads to an increase in its thickness to $d_h = 814\,nm$ and corresponds to the swelling

Table 7.1: Comparison of fitted parameters for composite structures with and without nanoMIP.

c_{NP}/c_{pp} (wt%)	d_h or d_{h-dry} (nm)	Re$\{n_h\}$	Im$\{n_h\}$	SR	f
0/3(Dry)	206	1.480	$< 10^{-3}$	5.42	1.00
0/3(Swollen)	1116	1.361	$< 10^{-3}$		0.19
6/1(Dry)	587	1.335	0.014	1.39	0.73
6/1(Swollen)	814	1.420	0.002		0.59

ratio of SR = 1.39 (see Figure (7.4)b). This value is much smaller than SR = 5.42 obtained for a film, which was prepared in identical way from only pNIPAAm polymer (c_{pp} = 3 wt% and c_{NP} = 0 wt%), see Figure (7.4)c, d). The reason for the hindered expansion of the composite films is that the embedded nanoMIP (or nanoNIP) nanoparticles swell much weaker compared to pNIPAAm-based hydrogel. In addition, they react with the benzophenon groups and thus can serve as an additional "supercrosslinking" nodes as was shown by previous studies with other nanoparticles [205].

As the overview in Table (7.1) presents, the imaginary part of fitted refractive index Im$\{n_h\}$ is order of magnitude higher for dry composite film than for a dry film composed of only pNIPAAm-based polymer. However, Im$\{n_h\}$ of the composite film with nanoMIP drops after the swelling in a working buffer and its value reaches Im$\{n_h\}$ for the film without nanoMIP. The reason is that the filling of voids in the composite structure with working buffer decreases the refractive index difference between nanoMIP (n_p = 1.48) and surrounding environment (n_b = 1 for air and ≈ 1.325 for working buffer), which reduces of the scattering losses of the waveguide.

For dry composite films, the total polymer volume fraction f (including both the nanoMIP and pNIPAAm polymers) is decreasing with the nanoMIP concentration c_{NP} due to the occurrence of void interstitial space as seen in Figure (7.2). However, an opposite behavior is observed when the films are swollen in working buffer due to the restricted swelling. For example, swollen layer composed of only a pNIPAAm hydrogel (prepared with c_{NP} = 0 wt% and c_{pp} = 3 wt%) exhibited the polymer volume fraction of f = 19%. When nanoMIP were loaded into the pNIPAAm network (composite layer prepared from a solution with c_{NP} = 6 wt% and c_{pp} = 1 wt%), a significantly higher total polymer volume fraction of f = 59% was determined. Let us note that SEM observations in Figure (7.2)b) suggest that the majority of polymer

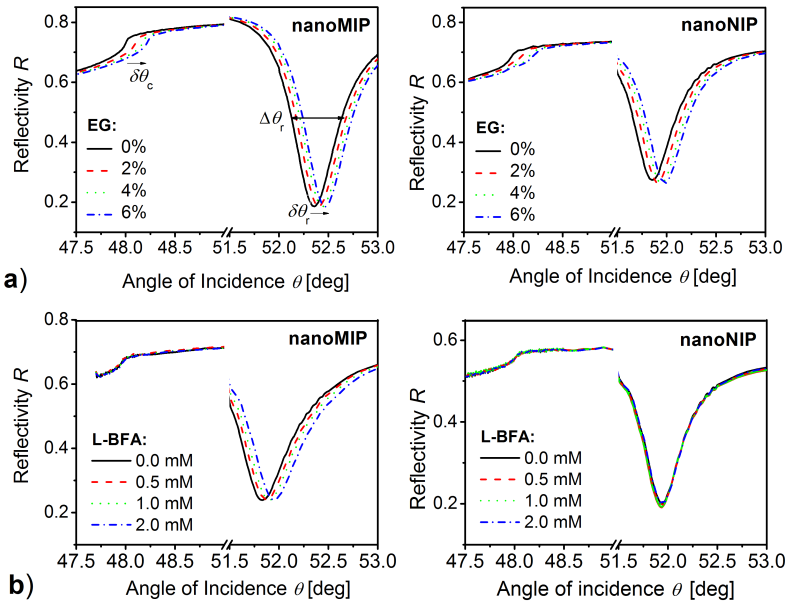

Figure 7.5: Measured angular reflectivity spectra for nanoMIP (left) and nanoNIP (right) composite film ($c_{NP} = 6$ wt% and $c_{pp} = 1$ wt%) that were brought in contact with a buffer spiked with a) reference ethylene glycol and b) target analyte L-BFA.

volume in such composite film is occupied by nanoMIPs and the polymer volume fraction measured by OWS approaches the value corresponding to maximum space filling for ordered colloidal crystals ($f = 74\%$) [206]. Assuming that the volume of spherical nanoMIPs is $\pi D^3/6$, the average number of nanoparticles per volume can be estimated as $6\left(f\pi D^3\right)^{-1}$, which yields $\approx 4 \times 10^2\, \mu m^{-3}$ for the composite layer prepared from a solution with $c_{NP} = 6$ wt% and $c_{pp} = 1$ wt%. Such composite films with high density of nanoMIP or nanoNIP were stable upon repeated swelling and drying cycles and we observed no changes in their binding characteristics when stored at ambient environment for over 4 months.

7.3.5 Refractometric Studies

The prepared composite films exhibit voids (with the relative volume $1 - f$) through which small molecules can rapidly diffuse. In order to prove this, refractive index changes induced by ethylene glycol (EG, molecular weight 67 g mol^{-1}) diffusing through the composite film were observed by OWS. Figure (7.5)a) shows measured angular reflectivity spectra with TM_1 resonance on the sensor surface carrying composite film loaded with nanoMIP (left) and

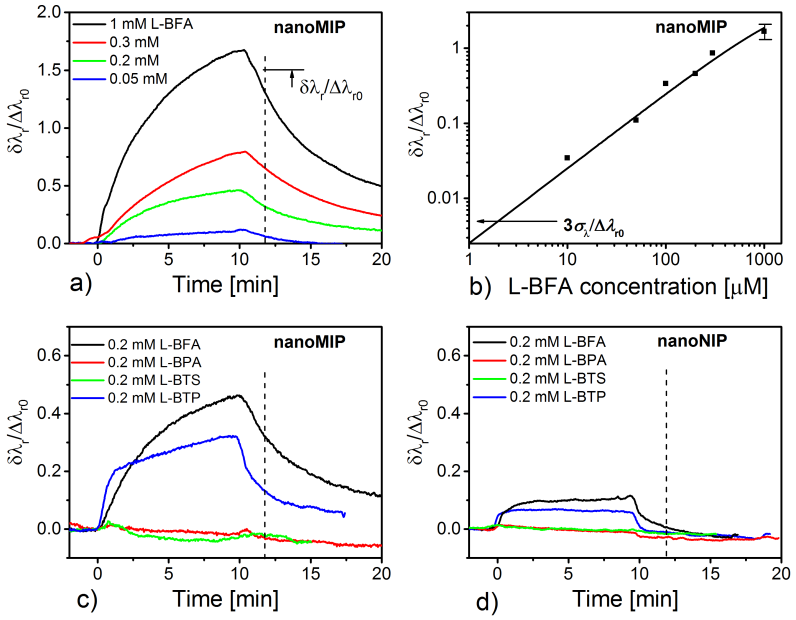

Figure 7.6: a) Kinetics of affinity binding of target L-BFA to nanoMIP waveguide at concentrations indicated in the inset and b) corresponding calibration curve with the error bar showing standard deviation of the response measured in triplicate on different waveguide chips. Comparison of binding kinetics of target analyte L-BFA and structurally similar reference analytes L-BTP, L-BPA, and L-BTS on c) measuring nanoMIP and d) control nanoNIP waveguides.

nanoNIP (right). Both layers were prepared by identical protocol from a solution with $c_{\mathrm{NP}} = 6\,\mathrm{wt\%}$ and $c_{\mathrm{pp}} = 1\,\mathrm{wt\%}$ and they were successively brought in contact with working buffer spiked with increasing concentration of EG. An increase in the refractive index of working buffer $\delta \mathrm{n}_b$ due to the spiking with EG is manifested as a shift in the critical angle θ_c. In addition, as EG molecules diffuse from a solution into composite film they change its (effective) refractive index n_h which leads to the shift in the resonant coupling angle θ_r. Shifts of $\delta\theta_r = 0 - 0.12°$ were observed upon successive flow of working buffer spiked with EG at concentrations between 0 and 6 vol% (which corresponds to the buffer refractive indices of $n_b = 1.325 - 1.331$ as determined from changes in θ_c). The TM_1 resonant angle shifts linearly with the refractive index sensitivity (slope) of $S = \frac{\delta\theta_r}{\delta n_b} = 24.5°$ per refractive index unit (RIU) for both nanoMIP and nanoNIP composite films. This value translates to the figure of merit in refractometric measurements of FOM = 52 (FOM = S/θ_r - defined as the ratio of refractive index sensitivity S and the resonance full width at half minimum θ_r) taking into account the width of TM_1 resonant dip of $\theta_r = 0.47°$. Such FOM is more than two-fold better than that for regular SPR at

the same wavelength (FOM = 20.8 RIU^{-1}) but it is about 15 times lower than that observed for similar pNIPAAm hydrogel waveguide that was modified with small biomolecules (FOM = 810 RIU^{-1}) [201]. The reason is that the loading of nanoMIPs or nanoNIPs into the waveguide leads to the increased imaginary part of the refractive index $\mathrm{Im}\{n_h\}$ (due to the scattering of the guided mode on nanoparticles) and subsequently to higher resonance width θ_r (increased by a factor of about five). In addition, the presence of nanoMIP increases the total polymer volume fraction f and thus smaller volume accessible for diffusing of analyte (sensitivity S and accessible volume proportional to $(1-f)$ is decreased by a factor of $2-3$ with respect to the structure without nanoMIP) [201].

7.3.6 Specificity and Affinity Studies

In order to characterize the specificity and binding capacity of imprinted cavities on the sensor surface, measuring (nanoMIP) and reference (nanoNIP) composite films were probed by TM_1 resonance upon a flow of series of samples spiked with L-BFA at concentrations between 0 and 2×10^{-3} M. As respective angular reflectivity curves in Figure (7.5)b) show, the flow of L-BFA is accompanied with a shift of the resonant angle $\delta\theta_r$ due to the binding-induced refractive index changes, which are about nine times higher for the nanoMIP composite film than for the reference surface with nanoNIPs. Such results indicate that the interaction of L-BFA with imprinted cavities leads to efficient accumulation of analyte in the film and that the non-specific interaction of L-BFA with used polymers is much weaker. The accumulation of target analyte in composite films was estimated from refractive index changes determined from measured shifts of the resonance coupling angle $\delta\theta_r$ and critical angle $\delta\theta_c$ (we assumed that the change in the thickness d_h due to the swelling of nanoMIP or nanoNIP that is associated with the affinity interaction with target L-BFA molecules was negligible and that the composite films change only their refractive index n_h). This analysis shows that the presence of target analyte at the 1×10^{-3} M concentration increases refractive index in the liquid sample by $\delta n_b \approx 7\times10^{-5}$ RIU and leads to the increase of refractive index of nanoMIPs composite layer of $\delta n_h \approx 3\times10^{-3}$ RIU. Assuming the refractive index increases linearly with the concentration of L-BFA and the composite film has slightly higher RI (so that the same amount of L-BFA will cause about 10% less RI change δn_h than δn_b), these data indicate that the concentration of L-BFA

accumulated in the nanoMIP composite film is increased by a factor of ≈ 46 with respect to that in the bulk sample solution. Much weaker accumulation was observed for the control nanoNIP films (measured value of $\delta n_h \approx 2.7 \times 10^{-4}$ RIU corresponds to the factor of ≈ 4), which indicates successful imprinting. It should be noted that nanoMIP nanoparticles exhibited surface area that was larger only by a factor of 1.23 with respect to that of nanoNIP as determined by gas adsorption experiment [207]. Therefore, the 10-times stronger accumulation of L-BFA in the nanoMIP composite film compared to that on the reference nano-NIP surface cannot be explained by unspecific interaction between the analyte and used polymers. Comparing the concentration of pre-concentrated analyte inside the nanoMIP layer with the density of imprinted nanoparticles, the number of binding pockets per nanoparticle can be estimated as $10^2 - 10^3$, which agrees with previous studies [207].

For more detailed studies of affinity interaction of specific L-BFA and other structurally similar control analytes with the nanoMIP and nanoNIP composite films, wavelength spectroscopy of guided waves was employed. As Figure (7.3)c) shows, a source of collimated polychromatic light beam was coupled to a glass prism and made incident at a fixed angle of incidence on the optically matched sensor chip with nanoMIP or nanoNIP layers (let us note that identical waveguides as in previous angular modulation studies were used). The angle of incidence θ was adjusted in such a way that the resonant excitation of TM_1 optical waveguide mode occurred in the vicinity to the wavelength of $\lambda = 632.8$ nm (the same as used in the previous angular modulation study). This TM_1 resonance is manifested as a narrow dip in the wavelength spectrum of reflected beam intensity, which was measured by a spectrometer. The refractive index-induced variations in the resonant wavelength $\delta\lambda_r$ were fitted in real time from measured wavelength spectra. The standard deviation of the sensor signal was $\sigma_\lambda = 3 \times 10^{-3}$ nm and the bulk refractive index sensitivity was about $S = \frac{\delta\lambda_r}{\delta n_b} = 5 \times 10^3$ nm/RIU, which translates to the refractive index resolution of $\sigma_\lambda / S \approx 6 \times 10^{-7}$ RIU (this resolution was more than order of magnitude better than that for previously used setup utilizing angular spectroscopy of guided waves). Prior to the measurement of resonance wavelength changes $\delta\lambda_r$ due to the affinity interaction of studied analytes, the sensor was calibrated in order to take into account small chip-to-chip variations and inaccuracies in the optical alignment. First, the resonant wavelength change $\delta\lambda_{r0}$ due to the flow of a working buffer with 0.5 vol%

of EG was measured and the sensor output was determined as the ratio $\frac{\delta\lambda_r}{\delta\lambda_{r0}}$.

As seen in Figure (7.6)a), a baseline in the sensor output was firstly established upon the flow of a working buffer. Afterwards, a series of samples spiked with L-BFA was sequentially injected to the sensor and let interact with the composite film for 10 min followed by rinsing for 10 min. Measured data show that the L-BFA binding results in a gradual shift in the sensor output $\frac{\delta\lambda_r}{\delta\lambda_{r0}}$ which saturates at levels that increases with the L-BFA concentration. Further, the sensor response was defined as the difference in the sensor output $\frac{\delta\lambda_r}{\delta\lambda_{r0}}$ before the injection of a sample and after the 2 min rinsing (indicated as a dashed line in Figure (7.6)a). The 2 min rinsing time was sufficiently long to replace the sample from the flow-cell by working buffer and thus eliminate the effect of the sensor output change due to the bulk refractive index change δn_b. Obtained calibration curve presented in Figure (7.6)b) reveals that the response increases with the L-BFA concentration. From these data, limit of detection (LOD) of 2×10^{-6} M was determined as $\frac{3\sigma_\lambda}{\mathrm{d}\lambda_r/\mathrm{d}c}$.

The specificity of the developed MIP OWS sensor for the detection of L-BFA was tested by comparing the response of nanoMIP and nanoNIP waveguides to target L-BFA and other structurally similar reference analytes summarized in Figure (7.1)c)–f): L-Boc-Tryptophan (L-BTP), L-Bocphenyl alanine (L-BPA), and L-Boc-tyrosine (L-BTS). First, the obtained data show that the response $\frac{\delta\lambda_r}{\delta\lambda_{r0}}$ to target L-BFA analyte at concentration of 0.2×10^{-3} M was around 14 times higher for the nanoMIP waveguide (Figure (7.6)c) than for the control nanoNIP (Figure (7.6)d), which is consistent with previous angular modulation measurements presented in Figure (7.5)b). The interaction of structurally similar L-BTP dissolved at same concentration of 0.2×10^{-3} M resulted in around two-fold lower response on nanoMIP surface than the target analyte L-BFA. On the control nanoNIP waveguide, the response to L-BTP was below values that can be reproducibly measured. The other reference analytes L-BPA and L-BTS showed non-measurable response on both nanoMIP and nanoNIP surfaces. Let us note that for L-BFA and L-BTP, a rapid change in the kinetics is observed in Figure (7.6)c) and d) after injecting the sample (t = 0) and working buffer (t = 10 min). It is probably caused by a bulk refractive index change, which was caused by a small variation in the amount of methanol (added due to the weaker solubility of these analytes). In general, the measured data on selectivity of L-BFA imprinted nanoMIP are in line with previous studies and reveal that using of pNIPAAm

hydrogel as a “glue” in the composite layer provided accessibility to MIP binding pockets, did not altered their affinity with target L-BFA analyte, and allowed improving sensitivity compared to other platforms for direct optical detection of small molecules that utilize 2D MIP coatings. For instance, the achieved limit of detection is about 30 times better than that reported for an optical sensor utilizing reflectometric interference spectroscopy (RIfS) with identically prepared L-BFA-imprinted nanoparticles that were attached to the surface in form of 2D layer [187]. This advancement can be attributed to the higher refractometric sensitivity of the OWS readout format and large-binding capacity that is offered by the 3D composite film architecture.

7.4 Conclusions

A new MIP architecture and readout method that is attractive for direct optical detection of low-molecular-weight analytes is reported. It is based on molecularly imprinted polymer nanoparticles (nanoMIP) that are embedded in a photo-crosslinkable hydrogel in order to provide high density of easily accessible imprinted moieties. Such composite films efficiently accumulate target analyte (about 10-fold increased concentration was observed as compared to films with non-imprinted nanoparticles nanoNIPs) and at the same time can act as an optical waveguide. The spectroscopy of guided waves supported by the composite nanoMIP film allowed for accurate readout of refractive index variations associated with the interaction of target analyte and MIP moieties. OWS can be performed using regular SPR optical setup and it enables direct label-free detection of a model low-molecular-weight analyte L-BFA - with an LOD as small as 2×10^{-6} M. The presented approach is generic and the using of photo-crosslinkable hydrogel allows for lithography or inject printing preparation of MIPs patterns. For instance, sensor chips carrying arrays of measuring and reference pads with different MIP moieties can be prepared in a much more straightforward and simple way than in case of traditional surface synthesis of MIPs on planar films. We believe that such advancements will allow harnessing current progress in the field of synthesis of high affinity MIP nanostructures (plastic antibody) and open a new door to development of next generation of sensitive and robust MIP sensors capable of multi-analyte and reference-compensated measurements.

8 Summary and Outlook

Summary

In this thesis, there are reports of four projects that cover new means to prepare and characterize responsive hydrogel nanostructures as well as their implementation to functional optical devices. In particular a photo-crosslinkable pNIPAAm-based polymer that forms a network under irradiation by UV light was used and structured by laser interference lithography, nanoimprint lithography, and template stripping. These techniques allowed for preparation of hydrogel structures tethered to a solid surface with feature size as small as 100 nm. Prepared thermo-responsive materials exhibited unusual and unique optical properties which hold potential to allow for actively controlled characteristics of plasmonic structures as well as provide ways in novel optical sensor concepts. Nanostructured hydrogel films were prepared on top of and below a thin Au film. Properties of such plasmonic structures were experimentally and theoretically investigated. Dense pNIPAAm relief grating was developed to reversibly open and close a plasmonic bandgap by collapsing and swelling the pNIPAAm structure immersed in water by temperature variations. This bandgap occurs at wavelength that can be tuned by the period of the grating and in the bandgap the surface plasmons propagating on the Au surface cease to exist. The limitation of such approach related to the swelling and collapsing of the pNIPAAm nanogratings concerning the aspect ratio is discussed. Gratings with the modulation depth up to 100 nm and periods below 300 nm were prepared. Another approach was employed to structure the same hydrogel by arrays of nanopillars based on nanoimprint lithography. The diameter of pNIPAAm nanopillars was of 143 nm and

the height reached 208 nm. This material was in situ investigated by a new optical method based on waveguide-mode enhanced diffraction measurements and it was complemented by atomic force microscopy study. Measurements suggest that pNIPAAm pillars swell in 3D with a swelling degree that is similar to that associated with 1D of from identical hydrogel film that is allowed to expand inly in one direction. In addition, effect of bending of pNIPAAm pillars is described and unusual behavior that allowed reversibly erase and re-form the structure is reported. Extraordinary transmission of light through nanohole array of gold mediated by thermo-responsive pNIPAAm hydrogel cushion layer was subject of research included in the thesis. Here a thin Au film with arrays of nanoholes was prepared by EBL, coated with pNIPAAm layer, attached to a transparent substrate and stripped. Results show that rapid swelling and collapsing of the hydrogel triggers flow of water through the plasmonic pores and strongly modulate the refractive index leading to changes in the transmission spectrum mediated by surface plasmon modes. The experiment results obtained were verified by the simulated results. An alternative approach to nano-structure the hydrogel material was employed by incorporating molecularly imprinted polymer nanoparticles. Composites films were prepared with a thickness chosen to support the optical waveguide modes and at the same time provide an open architecture to analyte molecules for diffusion when brought in contact with water. Polymer nanoparticles were imprinted with L-BFA – an amino acid derivative. The implemented sensor based on optical waveguide spectroscopy was demonstrated to directly detect this low molecular weight analyte at concentration as low as μM. The key characteristics of the biosensors was determined and compared to those for other state-of-the-art devices.

Future Outlook

Nanostructured hydrogels have gained considerable attention in recent years due to their unique properties to swell in response to the variation of some parameter of the medium. It can offer various advantages related to the network structure which makes it excellent candidates for biomedical fields such as drug delivery, tissue engineering, and biosensors. A range polymeric nanostructured hydrogel systems have been prepared and characterized in recent years [208], each one with its particular advantages and drawbacks. One of the most remarkable areas of research on hydrogels has been their stimulus sensitivity. In this

context poly (N-isopropylacrylamide) (pNIPAAm)-based hydrogel has received great attention having the photosensitive and thermo-responsive properties. It exhibits a well-defined lower critical solution temperature (LCST) in water around 31–34 °C, as this temperature is close to the body temperature this makes it suitable for a thermo-sensitive carrier to control drug activity. Various methods for structuring of hydrogels were developed including those based on microfluidics, photolithography or soft-lithography-based techniques. As nanostructured hydrogels exhibit a variety of functional properties such as swelling, surface, and optical properties, as well as the unique property of undergoing abrupt volume changes from their collapsed and swollen states in response to environmental stimuli, this feature can be successfully used to make carrier for drug delivery, micro-valves and micro-pumps, wavelength tunable optical filters, among others. The work described in this dissertation covers several topics that are expected to open door to follow up projects. Although many developments have taken place, there is still a huge space of research that concerns such stimuli-responsive materials in the future. Potential applications for these systems in our daily life should be devised and further developed. Here, many known challenges are still ahead, such as their use as stimuli-responsive nanocarriers, a general rapid responsiveness of the applied stimuli and the exact reproducibility, which requires prior attention. Potential future work based on this work may include:

- Plasmonic nanohole arrays that are functionalized with ligand molecules and tethered with a permeable hydrogel cushion are attractive for a flow-through biosensor. Such approach can be implemented with extremely simplified fluidic compared to those pursued now [40] and the response of the sensor is not hindered by slow diffusion to the surface.

- Active plasmonic application where spectrum of surface plasmon modes can be dynamically adjusted by responsive polymers. For instance, in implementation of plasmonic for amplification of signal in optical spectroscopy the enhanced field intensity can be tuned with respect to characteristics of studied analyte.

- 2D plasmonic optical circuits where propagation of surface plasmon beam is controlled by elements formed by responsive hydrogel nanostructures acting as mirrors, splitters or phase retarders.

- New adhesive, humidity sensor or safety features based on the unusual properties of imprinted responsive hydrogel nanostructures.
- Biosensors with array of detection format supported by hydrogel-functionalized spots in order to provide large binding capacity.
- New architectures of MIP sensors with nanoMIP materials printed and glued by a hydrogel to defined desired structures with good optical properties and open architecture for capture of large amounts of target analytes.

Bibliography

[1] M. W. G. de Bolster. Glossary of terms used in bioinorganic chemistry (IUPAC Recommendations 1997). *Pure and Applied Chemistry*, 69(6):1137–1152, jan 1997.

[2] Leland C. Clark and Champ Lyons. Electrode Systems for Continuous Monitoring in Cardiovascular Surgery. *Annals of the New York Academy of Sciences*, 102(1):29–45, dec 2006.

[3] Jiří Homola, Sinclair S Yee, and Günter Gauglitz. Surface plasmon resonance sensors: review. *Sensors and Actuators B: Chemical*, 54(1-2):3–15, jan 1999.

[4] Matthew A Cooper. Optical biosensors in drug discovery. *Nature Reviews Drug Discovery*, 1(7):515–528, jul 2002.

[5] Jeffrey N Anker, W Paige Hall, Olga Lyandres, Nilam C Shah, Jing Zhao, and Richard P Van Duyne. Biosensing with plasmonic nanosensors. *Nature Materials*, 7(6):442–453, jun 2008.

[6] Xudong Fan, Ian M. White, Siyka I. Shopova, Hongying Zhu, Jonathan D. Suter, and Yuze Sun. Sensitive optical biosensors for unlabeled targets: A review. *Analytica Chimica Acta*, 620(1-2):8–26, jul 2008.

[7] Dorothee Grieshaber, Robert MacKenzie, Janos Vörös, and Erik Reimhult. Electrochemical Biosensors - Sensor Principles and Architectures. *Sensors*, 8(3):1400–1458, mar 2008.

[8] Arben Merkoçi. Electrochemical biosensing with nanoparticles. *FEBS Journal*, 274(2):310–316, jan 2007.

[9] Joseph Wang. Electrochemical biosensors: Towards point-of-care cancer diagnostics. *Biosensors and Bioelectronics*, 21(10):1887–1892, apr 2006.

[10] Eric Bakker. Electrochemical Sensors. *Analytical Chemistry*, 76(12):3285–3298, jun 2004.

[11] Asha Chaubey and B.D. Malhotra. Mediated biosensors. *Biosensors and Bioelectronics*, 17(6-7):441–456, jun 2002.

[12] Mehrab Mehrvar and Mustafe Abdi. Recent Developments, Characteristics, and Potential Applications of Electrochemical Biosensors. *Analytical Sciences*, 20(8):1113–1126, jan 2004.

[13] S Weiss. Fluorescence Spectroscopy of Single Biomolecules. *Science*, 283(5408):1676–1683, mar 1999.

[14] M.S. Dresselhaus, G. Dresselhaus, R. Saito, and A. Jorio. Raman spectroscopy of carbon nanotubes. *Physics Reports*, 409(2):47–99, mar 2005.

[15] R. A. Potyrailo, S. E. Hobbs, and G. M. Hieftje. Optical waveguide sensors in analytical chemistry: today's instrumentation, applications and trends for future development. *Fresenius' Journal of Analytical Chemistry*, 362(4):349–373, oct 1998.

[16] J. A. De Feijter, J Benjamins, and F. A. Veer. Ellipsometry as a tool to study the adsorption behavior of synthetic and biopolymers at the air-water interface. *Biopolymers*, 17(7):1759–1772, jul 1978.

[17] Robert C Youngquist, Sally Carr, and D E N Davies. Optical coherence-domain reflectometry: a new optical evaluation technique. *Optics Letters*, 12(3):158, mar 1987.

[18] Jiri Homola. Present and future of surface plasmon resonance biosensors. *Analytical and Bioanalytical Chemistry*, 377(3):528–539, oct 2003.

[19] Jiří Homola. Surface Plasmon Resonance Sensors for Detection of Chemical and Biological Species. *Chemical Reviews*, 108(2):462–493, feb 2008.

[20] Claes Nylander, Bo Liedberg, and Tommy Lind. Gas detection by means of surface plasmon resonance. *Sensors and Actuators*, 3:79–88, jan 1982.

[21] Rebecca L. Rich and David G. Myszka. Survey of the 2009 commercial optical biosensor literature. *Journal of Molecular Recognition*, 24(6):892–914, nov 2011.

[22] Biacore : https://www.biacore.com/lifesciences/index.html.

[23] Windsor : http://www.windsorscientific.co.uk/index.php?main{_}id=27{\&}page{_}id=48.

[24] Bionavis : http://www.bionavis.com/.

[25] R. W. Wood. On a Remarkable Case of Uneven Distribution of Light in a Diffraction Grating Spectrum. *Proceedings of the Physical Society of London*, 18(1):269–275, jun 1902.

[26] Andreas Otto. Excitation of nonradiative surface plasma waves in silver by the method of frustrated total reflection. *Zeitschrift fur Physik*, 216(4):398–410, jul 1968.

[27] E. Kretschmann and Heinz Raether. Radiative decay of non-radiative surface plasmons excited by light. *Zeitschrift fur Naturforschung A*, 23:2135–2136, nov 1968.

[28] I. Pockrand, J.D. Swalen, J.G. Gordon, and M.R. Philpott. Surface plasmon spectroscopy of organic monolayer assemblies. *Surface Science*, 74(1):237–244, may 1978.

[29] J.G. Gordon and S. Ernst. Surface plasmons as a probe of the electrochemical interface. *Surface Science*, 101(1-3):499–506, dec 1980.

[30] G M Wysin, H J Simon, and R T Deck. Optical bistability with surface plasmons. *Optics Letters*, 6(1):30, jan 1981.

[31] Raffaele Colombelli. Quantum Cascade Surface-Emitting Photonic Crystal Laser. *Science*, 302(5649):1374–1377, nov 2003.

[32] Yu-Jung Lu, Jisun Kim, Hung-Ying Chen, Chihhui Wu, Nima Dabidian, Charlotte E Sanders, Chun-Yuan Wang, Ming-Yen Lu, Bo-Hong Li, Xianggang Qiu, Wen-Hao Chang, Lih-Juann Chen, Gennady Shvets, Chih-Kang Shih, and Shangjr Gwo. Plasmonic Nanolaser Using Epitaxially Grown Silver Film. *Science*, 337(6093):450–453, jul 2012.

[33] Volker J Sorger and Xiang Zhang. Spotlight on Plasmon Lasers. *Science*, 333(6043):709–710, aug 2011.

[34] Ren-Min Ma, Rupert F Oulton, Volker J Sorger, Guy Bartal, and Xiang Zhang. Room-temperature sub-diffraction-limited plasmon laser by total internal reflection. *Nature Materials*, 10(2):110–113, feb 2011.

[35] Peter Zijlstra, James W M Chon, and Min Gu. Five-dimensional optical recording mediated by surface plasmons in gold nanorods. *Nature*, 459(7245):410–413, may 2009.

[36] Bertrand Gauvreau, Alireza Hassani, Majid Fassi Fehri, Andrei Kabashin, and Maksim a Skorobogatiy. Photonic bandgap fiber-based Surface Plasmon Resonance sensors. *Optics Express*, 15(18):11413, aug 2007.

[37] Jian Qiang Liu, Ling-Ling Wang, Meng-Dong He, Wei-Qing Huang, Dianyuan Wang, B S Zou, and Shuangchun Wen. A wide bandgap plasmonic Bragg reflector. *Optics Express*, 16(7):4888, mar 2008.

[38] F. Argoul, K. Monier, T. Roland, J. Elezgaray, and L. Berguiga. High resolution surface plasmon microscopy for cell imaging. In *Proc. of SPIE*, page 771506, apr 2010.

[39] Carlos Escobedo, Alexandre G. Brolo, Reuven Gordon, and David Sinton. Optofluidic concentration: Plasmonic nanostructure as concentrator and sensor. *Nano Letters*, 12(3):1592–1596, feb 2012.

[40] Fatemeh Eftekhari, Carlos Escobedo, Jacqueline Ferreira, Xiaobo Duan, Emerson M. Girotto, Alexandre G. Brolo, Reuven Gordon, and David Sinton. Nanoholes as nanochannels: Flow-through plasmonic sensing. *Analytical Chemistry*, 81(11):4308–4311, may 2009.

[41] Heinz Raether. Surface plasmons on smooth surfaces. In *Surface Plasmons on Smooth and Rough Surfaces and on Gratings*, volume 111, pages 4–39. Springer Berlin Heidelberg, 1988.

[42] Yi Wang. *New Biosensor Applications Of Surface Plasmon and Hydrogel Optical Waveguide Spectroscopy*. PhD thesis, Johannes Gutenberg-Universität, 2010.

[43] P. B. Johnson and R. W. Christy. Optical Constants of the Noble Metals. *Physical Review B*, 6(12):4370–4379, dec 1972.

[44] Sabine Szunerits and Rabah Boukherroub. *Introduction to Plasmonics: Advances and Applications*. Pan Stanford Publishing Pte. Ltd., 2015.

[45] Sanong Ekgasit, Chuchaat Thammacharoen, and Wolfgang Knoll. Surface Plasmon Resonance Spectroscopy Based on Evanescent Field Treatment. *Analytical Chemistry*, 76(3):561–568, feb 2004.

[46] D.E. Aspnes. Optical properties of thin films. *Thin Solid Films*, 89(3):249–262, mar 1982.

[47] Wilford N. Hansen. Electric Fields Produced by the Propagation of Plane Coherent Electromagnetic Radiation in a Stratified Medium. *Journal of the Optical Society of America*, 58(3):380, mar 1968.

[48] T.J. Davis. Surface plasmon modes in multi-layer thin-films. *Optics Communications*, 282(1):135–140, jan 2009.

[49] Kazuyoshi Kurihara and Koji Suzuki. Theoretical Understanding of an Absorption-Based Surface Plasmon Resonance Sensor Based on Kretchmann's Theory. *Analytical Chemistry*, 74(3):696–701, jan 2002.

[50] Thorsten Liebermann and Wolfgang Knoll. Surface-plasmon field-enhanced fluorescence spectroscopy. *Colloids and Surfaces A: Physicochemical and Engineering Aspects*, 171(1-3):115–130, oct 2000.

[51] Bo Liedberg, Claes Nylander, and Ingemar Lunström. Surface plasmon resonance for gas detection and biosensing. *Sensors and Actuators*, 4:299–304, jan 1983.

[52] B K Oh, Y K Kim, Y M Bae, W H Lee, and J W Choi. Detection of Escherichia coli O157 : H7 using immunosensor based on surface plasmon resonance. *Journal of Microbiology and Biotechnology*, 12(5):780–786, oct 2002.

[53] V. Koubová, E. Brynda, L. Karasová, J. Škvor, J. Homola, J. Dostálek, P. Tobiška, and J. Rošický. Detection of foodborne pathogens using surface plasmon resonance biosensors. *Sensors and Actuators B: Chemical*, 74(1-3):100–105, apr 2001.

[54] Allen D. Taylor, Jon Ladd, Qiuming Yu, Shengfu Chen, Jiří Homola, and Shaoyi Jiang. Quantitative and simultaneous detection of four foodborne bacterial pathogens with a multi-channel SPR sensor. *Biosensors and Bioelectronics*, 22(5):752–758, jan 2006.

[55] Anand Subramanian, Joseph Irudayaraj, and Thomas Ryan. Mono and dithiol surfaces on surface plasmon resonance biosensors for detection of Staphylococcus aureus. *Sensors and Actuators B: Chemical*, 114(1):192–198, mar 2006.

[56] J. Spadavecchia, M. G. Manera, F. Quaranta, P. Siciliano, and R. Rella. Surface plamon resonance imaging of DNA based biosensors for potential applications in food analysis. *Biosensors and Bioelectronics*, 21(6):894–900, feb 2005.

[57] Declan A. Healy, Conor J. Hayes, Paul Leonard, Louise McKenna, and Richard O'Kennedy. Biosensor developments: application to prostate-specific antigen detection. *Trends in Biotechnology*, 25(3):125–131, 2007.

[58] Jingyan Wei, Ying Mu, Daqian Song, Xuexun Fang, Xia Liu, Lisha Bu, Hanqi Zhang, Guizhen Zhang, Jiahua Ding, Weizhong Wang, Qinhan Jin, and Guimin Luo. A novel sandwich immunosensing method for measuring cardiac troponin I in sera. *Analytical Biochemistry*, 321(2):209–216, oct 2003.

[59] K. Vengatajalabathy Gobi, Hiroyuki Iwasaka, and Norio Miura. Self-assembled PEG monolayer based SPR immunosensor for label-free detection of insulin. *Biosensors and Bioelectronics*, 22(7):1382–1389, jun 2007.

[60] Nuria Rojo, Guadalupe Ercilla, and Isabel Haro. GB virus C (GBV-C) / hepatitis G virus (HGV): towards the design of synthetic peptides-based biosensors for immunodiagnosis of GBV-C/HGV infection. *Current protein & peptide science*, 4(4):291–298, aug 2003.

[61] Maria Minunni and Marco Mascini. Detection of Pesticide in Drinking Water Using Real-Time Biospecific Interaction Analysis (BIA). *Analytical Letters*, 26(7):1441–1460, mar 1993.

[62] Marinella Farre, Elena Martinez, Javier Ramon, Alicia Navarro, Jelena Radjenovic, Elba Mauriz, Laura Lechuga, M. Pilar Marco, and Damia Barcelo. Part per trillion determination of atrazine in natural water samples by a surface plasmon resonance immunosensor. *Analytical and Bioanalytical Chemistry*, 388(1):207–214, mar 2007.

[63] Kyungsik Ock, Gabsoo Jang, Yongrae Roh, Sunghoon Kim, Jaeho Kim, and Kwangnak Koh. Optical detection of Cu2+ ion using a SQ-dye containing polymeric thin-film on Au surface. *Microchemical Journal*, 70(3):301–305, 2001.

[64] Jiri Homola and Marek Piliarik. *Surface Plasmon Resonance (SPR) Sensors*. Springer Series on Chemical Sensors and Biosensors. 2006.

[65] Volker Thomsen, Debbie Schatzlein, and David Mercuro. Limits of Detection in Spectroscopy. *Spectroscopy*, 18(12):112–114, dec 2003.

[66] Toyoichi Tanaka and David J. Fillmore. Kinetics of swelling of gels. *The Journal of Chemical Physics*, 70(3):1214, mar 1979.

[67] Mitsuhiro Shibayama and Toyoichi Tanaka. Volume phase transition and related phenomena of polymer gels. In *Responsive gels: volume transitions I*, volume 109, pages 1–62. Springer Berlin Heidelberg, 1993.

[68] M R Aguilar, C Elvira, A Gallardo, B Vázquez, and J S Román. Smart polymers and their applications as biomaterials. In *Topics in tissue engineering*, volume 3. Elsevier: Cambridge, UK, 2007.

[69] Ashok Kumar, Akshay Srivastava, Igor Yu Galaev, and Bo Mattiasson. Smart polymers: Physical forms and bioengineering applications. *Progress in Polymer Science*, 32(10):1205–1237, oct 2007.

[70] Michael C. Koetting, Jonathan T. Peters, Stephanie D. Steichen, and Nicholas A. Peppas. Stimulus-responsive hydrogels: Theory, modern advances, and applications. *Materials Science and Engineering: R: Reports*, 93:1–49, jul 2015.

[71] O Okay. *General Properties of Hydrogels*, volume 6 of *Springer Series on Chemical Sensors and Biosensors*. Springer Berlin Heidelberg, 2010.

[72] N Peppas. Hydrogels in pharmaceutical formulations. *European Journal of Pharmaceutics and Biopharmaceutics*, 50(1):27–46, jul 2000.

[73] Todd R. Hoare and Daniel S. Kohane. Hydrogels in drug delivery: Progress and challenges. *Polymer*, 49(8):1993–2007, apr 2008.

[74] Lan Wei, Chunhua Cai, Jiaping Lin, and Tao Chen. Dual-drug delivery system based on hydrogel/micelle composites. *Biomaterials*, 30(13):2606–2613, may 2009.

[75] A.A. Naddaf, I. Tsibranska, and H.-J. Bart. Kinetics of BSA release from poly(N-isopropylacrylamide) hydrogels. *Chemical Engineering and Processing: Process Intensification*, 49(6):581–588, jun 2010.

[76] Daniel James Hall, Olga V. Khutoryanskaya, and Vitaliy V. Khutoryanskiy. Developing synthetic mucosa-mimetic hydrogels to replace animal experimentation in characterisation of mucoadhesive drug delivery systems. *Soft Matter*, pages 9620–9623, jun 2011.

[77] Hossein Omidian and Kinam Park. Hydrogels. In *Fundamentals and Applications of Controlled Release Drug Delivery*, pages 75–105. Springer US, Boston, MA, 2012.

[78] Weiwei Gao, Drew Vecchio, Jieming Li, Jingying Zhu, Qiangzhe Zhang, Victoria Fu, Jiayang Li, Soracha Thamphiwatana, Diannan Lu, and Liangfang Zhang. Hydrogel containing nanoparticle-stabilized liposomes for topical antimicrobial delivery. *ACS Nano*, 8(3):2900–2907, feb 2014.

[79] Laura E. Strong, Shreyas N. Dahotre, and Jennifer L. West. Hydrogel-nanoparticle composites for optically modulated cancer therapeutic delivery. *Journal of Controlled Release*, 178(1):63–68, mar 2014.

[80] Yong Qiu and Kinam Park. Environment-sensitive hydrogels for drug delivery. *Advanced Drug Delivery Reviews*, 64(SUPPL.):49–60, dec 2012.

[81] Jeanie L. Drury and David J. Mooney. Hydrogels for tissue engineering: scaffold design variables and applications. *Biomaterials*, 24(24):4337–4351, nov 2003.

[82] N. A. Peppas, J. Z. Hilt, Ali Khademhosseini, and Robert Langer. Hydrogels in Biology and Medicine: From Molecular Principles to Bionanotechnology. *Advanced Materials*, 18(11):1345–1360, jun 2006.

[83] Paul C. Nicolson and Jürgen Vogt. Soft contact lens polymers: an evolution. *Biomaterials*, 22(24):3273–3283, dec 2001.

[84] B Balakrishnan, M Mohanty, P Umashankar, and A Jayakrishnan. Evaluation of an in situ forming hydrogel wound dressing based on oxidized alginate and gelatin. *Biomaterials*, 26(32):6335–6342, nov 2005.

[85] Kazuhiko Ishikiriyama, Minoru Todoki, Takuichi Kobayashi, and Hiroshi Tanzawa. Pore Size Distribution Measurements of Poly(methyl methacrylate) Hydrogel Membranes for Artificial Kidneys Using Differential Scanning Calorimetry. *Journal of Colloid and Interface Science*, 173(2):419–428, aug 1995.

[86] Masanori Kobayashi. Preliminary study of polyvinyl alcohol-hydrogel (PVA-H) artificial meniscus. *Biomaterials*, 24(4):639–647, feb 2003.

[87] Leonid Ionov. Hydrogel-based actuators: possibilities and limitations. *Materials Today*, 17(10):494–503, dec 2014.

[88] M. Guenther and Gerald Gerlach. Hydrogels for Chemical Sensors. In *Springer Series on Chemical Sensors and Biosensors*, volume 4, pages 165–195. Springer Berlin Heidelberg, Berlin, Heidelberg, 2009.

[89] Anca Mateescu, Yi Wang, Jakub Dostalek, and Ulrich Jonas. Thin Hydrogel Films for Optical Biosensor Applications. *Membranes*, 2(4):40–69, feb 2012.

[90] Andreas Richter, Georgi Paschew, Stephan Klatt, Jens Lienig, Karl-Friedrich Arndt, and Hans-Jürgen P. Adler. Review on Hydrogel-based pH Sensors and Microsensors. *Sensors*, 8(1):561–581, jan 2008.

[91] Ihor Tokarev and Sergiy Minko. Stimuli-responsive hydrogel thin films. *Soft Matter*, 5(3):511–524, nov 2009.

[92] Alena Aulasevich, Robert F. Roskamp, Ulrich Jonas, Bernhard Menges, Jakub Dostálek, and Wolfgang Knoll. Optical waveguide spectroscopy for the investigation of protein-functionalized hydrogel films. *Macromolecular Rapid Communications*, 30(9-10):872–877, may 2009.

[93] Jakub Dostalek, Yi Wang, and Chun Huang. Evanescent Wave Biosensors with a Hydrogel Binding Matrix. In *Handbook of Biofunctional Surfaces*, chapter 9, pages 361–406. Pan Stanford Publishing, may 2013.

[94] Juewen Liu. Oligonucleotide-functionalized hydrogels as stimuli responsive materials and biosensors. *Soft Matter*, 7(15):6757, may 2011.

[95] Xiaoping Yang, Xiaohan Pan, Jeff Blyth, and Christopher R. Lowe. Towards the real-time monitoring of glucose in tear fluid: Holographic glucose sensors with reduced interference from lactate and pH. *Biosensors and Bioelectronics*, 23(6):899–905, jan 2008.

[96] H.G. Schild. Poly(N-isopropylacrylamide): experiment, theory and application. *Progress in Polymer Science*, 17(2):163–249, jan 1992.

[97] Syang-Peng Rwei, Tun-Fun Way, Shu-Mei Chang, Whe-Yi Chiang, and Yi-Yin Lien. Thermo- and pH- responsive copolymers: Poly(N -Isopropylacrylamide- co -IAM) copolymers. *Journal of Applied Polymer Science*, 132(33):42367, sep 2015.

[98] Kimiko Makino, Jiro Hiyoshi, and Hiroyuki Ohshima. Kinetics of swelling and shrinking of poly (N-isopropylacrylamide) hydrogels at different temperatures. *Colloids and Surfaces B: Biointerfaces*, 19(2):197–204, dec 2000.

[99] Matthias J N Junk, Ulrich Jonas, and Dariush Hinderberger. EPR Spectroscopy Reveals Nanoinhomogeneities in the Structure and Reactivity of Thermoresponsive Hydrogels. *Small*, 4(9):1485–1493, sep 2008.

[100] Ashutosh Chilkoti, Matthew R. Dreher, Dan E. Meyer, and Drazen Raucher. Targeted drug delivery by thermally responsive polymers. *Advanced Drug Delivery Reviews*, 54(5):613–630, sep 2002.

[101] Chun Jen Huang, Jakub Dostalek, and Wolfgang Knoll. Long range surface plasmon and hydrogel optical waveguide field-enhanced fluorescence biosensor with 3D hydrogel binding matrix: On the role of diffusion mass transfer. *Biosensors and Bioelectronics*, 26(4):1425–1431, dec 2010.

[102] Ji-hyun Jang, Shalin J Jhaveri, Boris Rasin, Choengyang Koh, Christopher K Ober, and Edwin L Thomas. Three-Dimensionally-Patterned Submicrometer-Scale Hydrogel/Air Networks That Offer a New Platform for Biomedical Applications. *Nano Letters*, 8(5):1456–1460, apr 2008.

[103] Stephanie J. Bryant, Janet L. Cuy, Kip D. Hauch, and Buddy D. Ratner. Photo-patterning of porous hydrogels for tissue engineering. *Biomaterials*, 28(19):2978–2986, jul 2007.

[104] Judy Yeh, Yibo Ling, Jeffrey M. Karp, Jay Gantz, Akash Chandawarkar, George Eng, James Blumling III, Robert Langer, and Ali Khademhosseini. Micromolding of shape-controlled, harvestable cell-laden hydrogels. *Biomaterials*, 27(31):5391–5398, nov 2006.

[105] Huijie Hou, Woosik Kim, Melissa Grunlan, and Arum Han. A thermoresponsive hydrogel poly(N -isopropylacrylamide) micropatterning method using microfluidic techniques. *Journal of Micromechanics and Microengineering*, 19(12):127001, dec 2009.

[106] Olof Andersson, Andréas Larsson, Tobias Ekblad, and Bo Liedberg. Gradient Hydrogel Matrix for Microarray and Biosensor Applications: An Imaging SPR Study. *Biomacromolecules*, 10(1):142–148, jan 2009.

[107] Nan Zhang and Wolfgang Knoll. Thermally responsive hydrogel films studied by surface plasmon diffraction. *Analytical Chemistry*, 81(7):2611–2617, feb 2009.

[108] Alexander Revzin, Ryan J. Russell, Vamsi K. Yadavalli, Won-Gun Koh, Curt Deister, David D. Hile, Michael B. Mellott, and Michael V. Pishko. Fabrication of Poly(ethylene glycol) Hydrogel Microstructures Using Photolithography. *Langmuir*, 17(18):5440–5447, sep 2001.

[109] Stefan Kobel, Monika Limacher, Samy Gobaa, Thierry Laroche, and Matthias P. Lutolf. Micropatterning of Hydrogels by Soft Embossing. *Langmuir*, 25(15):8774–8779, aug 2009.

[110] Ye Zhou, Olof Andersson, Peter Lindberg, and Bo Liedberg. Reversible Hydrophobic Barriers Introduced by Microcontact Printing: Application to Protein Microarrays. *Microchimica Acta*, 146(3-4):193–205, jun 2004.

[111] Van N. Truskett and Michael P.C. Watts. Trends in imprint lithography for biological applications. *Trends in Biotechnology*, 24(7):312–317, jul 2006.

[112] Benno Rothenhausler and Wolfgang Knoll. Total internal diffraction of plasmon surface polaritons. *Applied Physics Letters*, 51(11):783, sep 1987.

[113] C. Vieu, F. Carcenac, A. Pépin, Y. Chen, M. Mejias, A. Lebib, L. Manin-Ferlazzo, L. Couraud, and H. Launois. Electron beam lithography: resolution limits and applications. *Applied Surface Science*, 164(1-4):111–117, sep 2000.

[114] K.-J. Byeon and H. Lee. Recent progress in direct patterning technologies based on nano-imprint lithography. *The European Physical Journal Applied Physics*, 59(1):10001, aug 2012.

[115] Stephen Y. Chou. Sub-10 nm imprint lithography and applications. *Journal of Vacuum Science & Technology B: Microelectronics and Nanometer Structures*, 15(6):2897, nov 1997.

[116] Pierre Colson, Catherine Henrist, and Rudi Cloots. Nanosphere Lithography: A Powerful Method for the Controlled Manufacturing of Nanomaterials. *Journal of Nanomaterials*, 2013:1–19, aug 2013.

[117] Toshiro Itani, Wataru Wakamiya, Julian Cashmore, and Malcolm Gower. 157-nm lithography with high numerical aperture lens for sub-70 nm node. *Microelectronic Engineering*, 67-68:39–46, 2003.

[118] Daniel Bratton, Da Yang, Junyan Dai, and Christopher K. Ober. Recent progress in high resolution lithography. *Polymers for Advanced Technologies*, 17(2):94–103, 2006.

[119] Jung-Hun Seo, Jung Ho Park, Seong-Il Kim, Bang Ju Park, Zhenqiang Ma, Jinnil Choi, and Byeong-Kwon Ju. Nanopatterning by Laser Interference Lithography: Applications to Optical Devices. *Journal of Nanoscience and Nanotechnology*, 14(2):1521–1532, feb 2014.

[120] Cheng Lu and R.H. Lipson. Interference lithography: a powerful tool for fabricating periodic structures. *Laser & Photonics Reviews*, 4(4):568–580, may 2009.

[121] Mana Toma, Koji Toma, Pavel Adam, Jiri Homola, Wolfgang Knoll, and Jakub Dostálek. Surface plasmon-coupled emission on plasmonic Bragg gratings. *Optics Express*, 20(13):14042, jun 2012.

[122] Evaporation : https://en.wikipedia.org/wiki/Evaporation_%28deposition%29.

[123] J Christopher Love, Lara A. Estroff, Jennah K. Kriebel, Ralph G. Nuzzo, and George M. Whitesides. Self-Assembled Monolayers of Thiolates on Metals as a Form of Nanotechnology. *Chemical Reviews*, 105(4):1103–1170, apr 2005.

[124] A K Geim, S V Dubonos, I V Grigorieva, K S Novoselov, A A Zhukov, and S Yu Shapoval. Microfabricated adhesive mimicking gecko foot-hair. *Nature Materials*, 2(7):461–463, jul 2003.

[125] N J Glassmaker, A Jagota, C-Y Hui, and J. Kim. Design of biomimetic fibrillar interfaces: 1. Making contact. *Journal of The Royal Society Interface*, 1(1):23–33, nov 2004.

[126] Liang Dong, Abhishek K Agarwal, David J Beebe, and Hongrui Jiang. Adaptive liquid microlenses activated by stimuli-responsive hydrogels. *Nature*, 442(7102):551–554, aug 2006.

[127] Sanford A. Asher and John H. Holtz. Polymerized colloidal crystal hydrogel film as intelligent chemical sensing materials. *Nature*, 389(6653):829–832, oct 1997.

[128] Ji Hwan Kang, Jun Hyuk Moon, Seung Kon Lee, Sung Gyu Park, Se Gyu Jang, Shu Yang, and Seung Man Yang. Thermoresponsive hydrogel photonic crystals by three-dimensional holographic lithography. *Advanced Materials*, 20(16):3061–3065, jul 2008.

[129] Vladimir L. Alexeev. Photonic Crystal Glucose-Sensing Material for Noninvasive Monitoring of Glucose in Tear Fluid. *Clinical Chemistry*, 50(12):2353–2360, dec 2004.

[130] Vijay R. Tirumala, Ralu Divan, Leonidas E. Ocola, and Derrick C. Mancini. Direct-write e-beam patterning of stimuli-responsive hydrogel nanostructures. *Journal of Vacuum Science & Technology B: Microelectronics and Nanometer Structures*, 23(6):3124, dec 2005.

[131] Mary Caldorera-Moore, Min Kyoo Kang, Zachary Moore, Vikramjit Singh, S. V. Sreenivasan, Li Shi, Rui Huang, and Krishnendu Roy. Swelling behavior of nanoscale, shape- and size-specific, hydrogel particles fabricated using imprint lithography. *Soft Matter*, 7(6):2879, feb 2011.

[132] F Di Benedetto, a Biasco, D Pisignano, and R Cingolani. Patterning polyacrylamide hydrogels by soft lithography. *Nanotechnology*, 16(5):S165–S170, feb 2005.

[133] Misuk Bae, Richard a. Gemeinhart, Ralu Divan, Kamlesh J. Suthar, and Derrick C. Mancini. Fabrication of poly(ethylene glycol) hydrogel structures for pharmaceutical applications using electron beam and optical lithography. *Journal of Vacuum Science & Technology B: Microelectronics and Nanometer Structures*, 28(6):C6P24, dec 2010.

[134] Chun-Wen Kuo, Jau-Ye Shiu, and Peilin Chen. Size- and Shape-Controlled Fabrication of Large-Area Periodic Nanopillar Arrays. *Chemistry of Materials*, 15(15):2917–2920, jul 2003.

[135] Dominic Ho, Jianli Zou, Bogdan Zdyrko, K. Swaminathan Iyer, and Igor Luzinov. Capillary force lithography: the versatility of this facile approach in developing nanoscale applications. *Nanoscale*, 7(2):401–414, sep 2015.

[136] Edward D. Palik. *Handbook of optical constants of solids*, volume 3. Academic press, 1998.

[137] Murat Guvendiren, Shu Yang, and Jason A. Burdick. Swelling-Induced Surface Patterns in Hydrogels with Gradient Crosslinking Density. *Advanced Functional Materials*, 19(19):3038–3045, oct 2009.

[138] Patrick W. Beines, Iris Klosterkamp, Bernhard Menges, Ulrich Jonas, and Wolfgang Knoll. Responsive thin hydrogel layers from photo-cross-linkable poly(N-isopropylacrylamide) terpolymers. *Langmuir*, 23(4):2231–2238, jan 2007.

[139] Matthias J. N. Junk, Rudiger Berger, and Ulrich Jonas. Atomic Force Spectroscopy of Thermoresponsive Photo-Cross-Linked Hydrogel Films. *Langmuir*, 26(10):7262–7269, may 2010.

[140] George M Hale and Marvin R Querry. Optical Constants of Water in the 200-nm to 200-μm Wavelength Region. *Applied Optics*, 12(3):555, mar 1973.

[141] Ryan Toomey, Daniel Freidank, and Jürgen Rühe. Swelling Behavior of Thin, Surface-Attached Polymer Networks. *Macromolecules*, 37(3):882–887, jan 2004.

[142] K R Catchpole and a Polman. Plasmonic solar cells. *Optics express*, 16(26):21793–800, dec 2008.

[143] J R Krenn, H Ditlbacher, G Schider, A Hohenau, A Leitner, and F R Aussenegg. Surface plasmon micro- and nano-optics. *Journal of Microscopy*, 209(3):167–172, mar 2003.

[144] Benedikt Schwarz, Peter Reininger, Daniela Ristanić, Hermann Detz, Aaron Maxwell Andrews, Werner Schrenk, and Gottfried Strasser. Monolithically integrated mid-infrared lab-on-a-chip using plasmonics and quantum cascade structures. *Nature Communications*, 5(May):1–7, jun 2014.

[145] Jiao Lin, J P Balthasar Mueller, Qian Wang, G. Yuan, Nicholas Antoniou, X.-C. Yuan, and Federico Capasso. Polarization-Controlled Tunable Directional Coupling of Surface Plasmon Polaritons. *Science*, 340(6130):331–334, apr 2013.

[146] Lin Li, Tao Li, Shuming Wang, Shining Zhu, and Xiang Zhang. Broad Band Focusing and Demultiplexing of In-Plane Propagating Surface Plasmons. *Nano Letters*, 11(10):4357–4361, oct 2011.

[147] H. Ditlbacher, J. R. Krenn, N. Felidj, B. Lamprecht, G. Schider, M. Salerno, A. Leitner, and F. R. Aussenegg. Fluorescence imaging of surface plasmon fields. *Applied Physics Letters*, 80(3):404, jan 2002.

[148] M. U. González, J.-C. Weeber, A.-L. Baudrion, A. Dereux, A. L. Stepanov, J. R. Krenn, E. Devaux, and T. W. Ebbesen. Design, near-field characterization, and modeling of 45° surface-plasmon Bragg mirrors. *Physical Review B*, 73(15):155416, apr 2006.

[149] Leilei Yin, Vitali K. Vlasko-Vlasov, John Pearson, Jon M. Hiller, Jiong Hua, Ulrich Welp, Dennis E. Brown, and Clyde W. Kimball. Subwavelength Focusing and Guiding of Surface Plasmons. *Nano Letters*, 5(7):1399–1402, jul 2005.

[150] W. L. Barnes, T. W. Preist, S. C. Kitson, and J. R. Sambles. Physical origin of photonic energy gaps in the propagation of surface plasmons on gratings. *Physical Review B*, 54(9):6227–6244, sep 1996.

[151] S. C. Kitson, W. L. Barnes, and J. R. Sambles. Surface-plasmon energy gaps and photoluminescence. *Physical Review B*, 52(15):11441–11445, oct 1995.

[152] Dirk Kuckling, Marianne E. Harmon, and Curtis W. Frank. Photo-Cross-Linkable PNIPAAm Copolymers. 1. Synthesis and Characterization of Constrained Temperature-Responsive Hydrogel Layers. *Macromolecules*, 35(16):6377–6383, jul 2002.

[153] Jacek Gosciniak, Sergey I Bozhevolnyi, Thomas B Andersen, Valentyn S Volkov, Jakob Kjelstrup-Hansen, Laurent Markey, and Alain Dereux. Thermo-optic control of dielectric-loaded plasmonic waveguide components. *Optics Express*, 18(2):1207, jan 2010.

[154] Xu Dong, Xianbo Zou, Xiaoyun Liu, Ping Lu, Jianmao Yang, Danli Lin, Li Zhang, and Liusheng Zha. Temperature-tunable plasmonic property and SERS activity of the monodisperse thermo-responsive composite microgels with core-shell structure based on gold nanorod as core. *Colloids and Surfaces A: Physicochemical and Engineering Aspects*, 452:46–50, jun 2014.

[155] Helene Gehan, Claire Mangeney, Jean Aubard, Georges Levi, Andreas Hohenau, Joachim R Krenn, Emmanuelle Lacaze, and Nordin Felidj. Design and Optical Properties of Active Polymer-Coated Plasmonic Nanostructures. *The Journal of Physical Chemistry Letters*, 2(8):926–931, apr 2011.

[156] Mana Toma, Ulrich Jonas, Anca Mateescu, Wolfgang Knoll, and Jakub Dostalek. Active control of SPR by thermoresponsive hydrogels for biosensor applications. *Journal of Physical Chemistry C*, 117(22):11705–11712, may 2013.

[157] T. W. Ebbesen, H. J. Lezec, H. F. Ghaemi, T Thio, and P. A. Wolff. Extraordinary optical transmission through sub-wavelength hole arrays. *Nature*, 391(6668):667–669, feb 1998.

[158] D. E. Grupp, H. J. Lezec, T. W. Ebbesen, K. M. Pellerin, and Tineke Thio. Crucial role of metal surface in enhanced transmission through subwavelength apertures. *Applied Physics Letters*, 77(11):1569, jul 2000.

[159] K. J Klein Koerkamp, S. Enoch, F. B. Segerink, N. F. van Hulst, and L. Kuipers. Strong Influence of Hole Shape on Extraordinary Transmission through Periodic Arrays of Subwavelength Holes. *Physical Review Letters*, 92(18):183901, may 2004.

[160] C Genet and T W Ebbesen. Light in tiny holes. *Nature*, 445(7123):39–46, jan 2007.

[161] L. Martín-Moreno, F. J. García-Vidal, H. J. Lezec, K. M. Pellerin, T. Thio, J. B. Pendry, and T. W. Ebbesen. Theory of Extraordinary Optical Transmission through Subwavelength Hole Arrays. *Physical Review Letters*, 86(6):1114–1117, feb 2001.

[162] K. L. van der Molen, K. J. Klein Koerkamp, S. Enoch, F. B. Segerink, N. F. van Hulst, and L. Kuipers. Role of shape and localized resonances in extraordinary transmission through periodic arrays of subwavelength holes: Experiment and theory. *Physical Review B*, 72(4):045421, jul 2005.

[163] A Degiron and T W Ebbesen. The role of localized surface plasmon modes in the enhanced transmission of periodic subwavelength apertures. *Journal of Optics A: Pure and Applied Optics*, 7(2):S90–S96, feb 2005.

[164] Kevin A Tetz, Lin Pang, and Yeshaiahu Fainman. High-resolution surface plasmon resonance sensor based on linewidth-optimized nanohole array transmittance. *Optics Letters*, 31(10):1528, feb 2006.

[165] Ahmet A. Yanik, Min Huang, Osami Kamohara, Alp Artar, Thomas W. Geisbert, John H. Connor, and Hatice Altug. An Optofluidic Nanoplasmonic Biosensor for Direct Detection of Live Viruses from Biological Media. *Nano Letters*, 10(12):4962–4969, dec 2010.

[166] Hyungsoon Im, Si Hoon Lee, Nathan J. Wittenberg, Timothy W. Johnson, Nathan C. Lindquist, Prashant Nagpal, David J. Norris, and Sang-Hyun Oh. Template-Stripped Smooth Ag Nanohole Arrays with Silica Shells for Surface Plasmon Resonance Biosensing. *ACS Nano*, 5(8):6244–6253, aug 2011.

[167] Alexandre G Brolo, Reuven Gordon, Brian Leathem, and Karen L Kavanagh. Surface Plasmon Sensor Based on the Enhanced Light Transmission through Arrays of Nanoholes in Gold Films. *Langmuir*, 20(12):4813–4815, jun 2004.

[168] Alexandre G Brolo, Shing C Kwok, Matthew G Moffitt, Reuven Gordon, Jason Riordon, and Karen L Kavanagh. Enhanced Fluorescence from Arrays of Nanoholes in a Gold Film. *Journal of the American Chemical Society*, 127(42):14936–14941, oct 2005.

[169] Mohamadreza Najiminaini, Fartash Vasefi, Bozena Kaminska, and Jeffrey J L Carson. Nanohole-array-based device for 2D snapshot multispectral imaging. *Scientific Reports*, 3:2589, sep 2013.

[170] Matthew J. Dicken, Luke A. Sweatlock, Domenico Pacifici, Henri J. Lezec, Kaushik Bhattacharya, and Harry A. Atwater. Electrooptic modulation in thin film barium titanate plasmonic interferometers. *Nano Letters*, 8(11):4048–4052, oct 2008.

[171] Etai Rosenkrantz and Shlomi Arnon. Local Surface Plasmon Tuning for Optical Devices. *IEEE Photonics Technology Letters*, 27(6):669–672, mar 2015.

[172] Vasily V. Temnov, Gaspar Armelles, Ulrike Woggon, Dmitry Guzatov, Alfonso Cebollada, Antonio Garcia-Martin, Jose-Miguel Garcia-Martin, Tim Thomay, Alfred Leitenstorfer, and Rudolf Bratschitsch. Active magneto-plasmonics in hybrid metal-ferromagnet structures. *Nature Photonics*, 4(2):107–111, jan 2010.

[173] C. Hermann, V. Kosobukin, G. Lampel, J. Peretti, V. Safarov, and P. Bertrand. Surface-enhanced magneto-optics in metallic multilayer films. *Physical Review B*, 64(23):235422, nov 2001.

[174] Ragip A Pala, Ken T Shimizu, Nicholas A Melosh, and Mark L Brongersma. A Nonvolatile Plasmonic Switch Employing Photochromic Molecules. *Nano Letters*, 8(5):1506–1510, may 2008.

[175] Yan Jun Liu, Guang Yuan Si, Eunice S P Leong, Ning Xiang, Aaron J. Danner, and Jing Hua Teng. Light-Driven Plasmonic Color Filters by Overlaying Photoresponsive Liquid Crystals on Gold Annular Aperture Arrays. *Advanced Materials*, 24(23):OP131–OP135, jun 2012.

[176] Luca Piantanida, Denys Naumenko, Emanuela Torelli, Monica Marini, Dennis M. Bauer, Ljiljana Fruk, Giuseppe Firrao, and Marco Lazzarino. Plasmon resonance tuning using DNA origami actuation. *Chem. Commun.*, 51(23):4789–4792, feb 2015.

[177] Kai Chen, Eunice Sok Ping Leong, Michael Rukavina, Tadaaki Nagao, Yan Jun Liu, and Yuebing Zheng. Active molecular plasmonics: tuning surface plasmon resonances by exploiting molecular dimensions. *Nanophotonics*, 4(1):186–197, jun 2015.

[178] Jun Matsui, Kensuke Akamatsu, Noriaki Hara, Daisuke Miyoshi, Hidemi Nawafune, Katsuyuki Tamaki, and Naoki Sugimoto. SPR Sensor Chip for Detection of Small Molecules Using Molecularly Imprinted Polymer with Embedded Gold Nanoparticles. *Analytical Chemistry*, 77(13):4282–4285, jul 2005.

[179] Ilke Anac, Alena Aulasevich, Matthias J N Junk, Piotr Jakubowicz, Robert F. Roskamp, Bernhard Menges, Ulrich Jonas, and Wolfgang Knoll. Optical characterization of co-nonsolvency effects in thin responsive PNIPAAm-based gel layers exposed to ethanol/water mixtures. *Macromolecular Chemistry and Physics*, 211(9):1018–1025, mar 2010.

[180] Nityanand Sharma, Christian Petri, Ulrich Jonas, Monika Bach, Günter Tovar, Kateřina Mrkvová, Milan Vala, Jiří Homola, Wolfgang Knoll, and Jakub Dostálek. Molecularly Imprinted Polymer Waveguides for Direct Optical Detection of Low-Molecular-Weight Analytes. *Macromolecular Chemistry and Physics*, 215(23):2295–2304, dec 2014.

[181] Olivier Y F Henry, David C. Cullen, and Sergey A. Piletsky. Optical interrogation of molecularly imprinted polymers and development of MIP sensors: a review. *Analytical and Bioanalytical Chemistry*, 382(4):947–956, jun 2005.

[182] M. Lotierzo, O.Y.F Henry, S. Piletsky, I. Tothill, D. Cullen, M. Kania, B. Hock, and A.P.F Turner. Surface plasmon resonance sensor for domoic acid based on grafted imprinted polymer. *Biosensors and Bioelectronics*, 20(2):145–152, sep 2004.

[183] Roderick B. Pernites, Ramakrishna R. Ponnapati, and Rigoberto C. Advincula. Surface Plasmon Resonance (SPR) Detection of Theophylline via Electropolymerized Molecularly Imprinted Polythiophenes. *Macromolecules*, 43(23):9724–9735, dec 2010.

[184] Natalie R. Walker, Matthew J. Linman, Margaret M. Timmers, Stacey L. Dean, Colleen M. Burkett, Julie A. Lloyd, Joel D. Keelor, Brandi M. Baughman, and Paul L. Edmiston. Selective detection of gas-phase TNT by integrated optical waveguide spectrometry using molecularly imprinted sol-gel sensing films. *Analytica Chimica Acta*, 593(1):82–91, jun 2007.

[185] C.A. Barrios, S. Carrasco, M. Francesca, P. Yurrita, F. Navarro-Villoslada, and M.C. Moreno-Bondi. Molecularly imprinted polymer for label-free integrated optical waveguide bio(mimetic)sensors. *Sensors and Actuators B: Chemical*, 161(1):607–614, jan 2012.

[186] Dirk Nopper, Olaf Lammershop, Günter Wulff, and Günter Gauglitz. Amidine-based molecularly imprinted polymers-new sensitive elements for chiral chemosensors. *Analytical and Bioanalytical Chemistry*, 377(4):608–613, oct 2003.

[187] Felix Kolarov, Klaus Niedergall, Monika Bach, Günter E M Tovar, and Günter Gauglitz. Optical sensors with molecularly imprinted nanospheres: A promising approach for robust and label-free detection of small molecules. *Analytical and Bioanalytical Chemistry*, 402(10):3245–3252, apr 2012.

[188] Yannick Fuchs, Olivier Soppera, Andrew G. Mayes, and Karsten Haupt. Holographic molecularly imprinted polymers for label-free chemical sensing. *Advanced Materials*, 25(4):566–570, oct 2013.

[189] Jinhua Li, Zhong Zhang, Shoufang Xu, Lingxin Chen, Na Zhou, Hua Xiong, and Hailong Peng. Label-free colorimetric detection of trace cholesterol based on molecularly imprinted photonic hydrogels. *Journal of Materials Chemistry*, 21(48):19267, nov 2011.

[190] C.A. Barrios, C. Zhenhe, F. Navarro-Villoslada, D. López-Romero, and M.C. Moreno-Bondi. Molecularly imprinted polymer diffraction grating as label-free optical bio(mimetic)sensor. *Biosensors and Bioelectronics*, 26(5):2801–2804, jan 2011.

[191] A.G. Mayes and M.J Whitcombe. Synthetic strategies for the generation of molecularly imprinted organic polymers. *Advanced Drug Delivery Reviews*, 57(12):1742–1778, dec 2005.

[192] Yannick Fuchs, Olivier Soppera, and Karsten Haupt. Photopolymerization and photostructuring of molecularly imprinted polymers for sensor applications-A review. *Analytica Chimica Acta*, 717(2012):7–20, mar 2012.

[193] Xiaobin Hu, Qi An, Guangtao Li, Shengyang Tao, and Jian Liu. Imprinted Photonic Polymers for Chiral Recognition. *Angewandte Chemie International Edition*, 45(48):8145–8148, dec 2006.

[194] Mark E. Byrne, Kinam Park, and Nicholas a. Peppas. Molecular imprinting within hydrogels. *Advanced Drug Delivery Reviews*, 54(1):149–161, jan 2002.

[195] Michael Riskin, Ran Tel-Vered, Oleg Lioubashevski, and Itamar Willner. Ultrasensitive Surface Plasmon Resonance Detection of Trinitrotoluene by a Bis-aniline-Cross-Linked Au Nanoparticles Composite. *Journal of the American Chemical Society*, 131(21):7368–7378, jun 2009.

[196] Dorothea Vaihinger, Katharina Landfester, Iris Kräuter, Herwig Brunner, and Günter E M Tovar. Molecularly imprinted polymer nanospheres as synthetic affinity receptors obtained by miniemulsion polymerisation. *Macromolecular Chemistry and Physics*, 203(13):1965–1973, sep 2002.

[197] Alessandro Poma, Antonio Guerreiro, Michael J Whitcombe, Elena V Piletska, Anthony P F Turner, and Sergey A Piletsky. Solid-Phase Synthesis of Molecularly Imprinted Polymer Nanoparticles with a Reusable Template-Plastic Antibodies. *Advanced Functional Materials*, 23(22):2821–2827, jun 2013.

[198] António R. Guerreiro, Iva Chianella, Elena Piletska, Michael J. Whitcombe, and Sergey A. Piletsky. Selection of imprinted nanoparticles by affinity chromatography. *Biosensors and Bioelectronics*, 24(8):2740–2743, apr 2009.

[199] Iva Chianella, Antonio Guerreiro, Ewa Moczko, J Sarah Caygill, Elena V Piletska, Isabel M Perez De Vargas Sansalvador, Michael J Whitcombe, and Sergey A Piletsky. Direct Replacement of Antibodies with Molecularly Imprinted Polymer Nanoparticles in ELISA-Development of a Novel Assay for Vancomycin. *Analytical Chemistry*, 85(17):8462–8468, sep 2013.

[200] Yuki Taguchi, Eri Takano, and Toshifumi Takeuchi. SPR Sensing of Bisphenol A Using Molecularly Imprinted Nanoparticles Immobilized on Slab Optical Waveguide with Consecutive Parallel Au and Ag Deposition Bands Coexistent with Bisphenol A-Immobilized Au Nanoparticles. *Langmuir*, 28(17):7083–7088, may 2012.

[201] Yi Wang, Chun-Jen Huang, Ulrich Jonas, Tianxin Wei, Jakub Dostalek, and Wolfgang Knoll. Biosensor based on hydrogel optical waveguide spectroscopy. *Biosensors and Bioelectronics*, 25(7):1663–1668, mar 2010.

[202] Qingwen Zhang, Yi Wang, Anca Mateescu, Khulan Sergelen, Asmorom Kibrom, Ulrich Jonas, Tianxin Wei, and Jakub Dostalek. Biosensor based on hydrogel optical waveguide spectroscopy for the detection of 17β-estradiol. *Talanta*, 104(2013):149–154, jan 2013.

[203] Achim Weber, Melanie Dettling, Herwig Brunner, and Günter E M Tovar. Isothermal Titration Calorimetry of Molecularly Imprinted Polymer Nanospheres. *Macromolecular Rapid Communications*, 23(14):824–828, oct 2002.

[204] Radan Slavík and Jiří Homola. Ultrahigh resolution long range surface plasmon-based sensor. *Sensors and Actuators B: Chemical*, 123(1):10–12, apr 2007.

[205] Coenraad R van den Brom, Ilke Anac, Robert F Roskamp, Markus Retsch, Ulrich Jonas, Bernhard Menges, and Jon A. Preece. The swelling behaviour of thermoresponsive hydrogel/silica nanoparticle composites. *Journal of Materials Chemistry*, 20(23):4827, may 2010.

[206] N.W. Ashcroft and N.D. Mermin. *Solid State Physics*. Hrw international editions edition, 1976.

[207] Mathias Lehmann, Melanie Dettling, Herwig Brunner, and Günter E.M. Tovar. Affinity parameters of amino acid derivative binding to molecularly imprinted nanospheres consisting of poly[(ethylene glycol dimethacrylate)-co-(methacrylic acid)]. *Journal of Chromatography B*, 808(1):43–50, aug 2004.

[208] Kokkarachedu Varaprasad, Emmanuel Rotimi Sadiku, Koduri Ramam, Jaragula Jayaramudu, and G. Siva Mohan Reddy. Significances of Nanostructured Hydrogels for Valuable Applications. In *Nanostructured Polymer Blends*, pages 273–298. Elsevier, 2014.